Theoretical investigation of the dynamics and microhydration of the $F^- + CH_3I$ S_N2 and proton-transfer reactions

PhD thesis

Balázs Olasz

Supervisor:

Dr. Gábor Czakó, DSc

Assistant Professor of Chemistry, University of Szeged

Place of the PhD process:

Faculty of Science and Informatics of the University of Szeged

Department of Physical Chemistry and Materials Science

Doctoral School:

University of Szeged

Doctoral School of Chemistry

Time of the PhD process:

2015-2018

Publications covered in the thesis*

- **B. Olasz**, I. Szabó, G. Czakó, High-level *ab initio* potential energy surface and dynamics of the $F^- + CH_3I$ S_N2 and proton-transfer reactions, Chem. Sci., 2017, 8, 3164−3170
- I. Szabó, **B. Olasz**, G. Czakó, Deciphering front-side complex formation in S_N2 reactions via dynamics mapping, J. Phys. Chem. Lett., 2017, 8, 2917−2923
- M. Stei, E. Carrascosa, A. Dörfler, J. Meyer, **B. Olasz**, G. Czakó, A. Li, H. Guo, R. Wester, Stretching vibration is spectator in nucleophilic substitution, 2018, Sci. Adv., 4, eaas9544
- **B. Olasz**, G. Czakó, Mode-specific quasiclassical dynamics of the $F^- + CH_3I$ S_N2 and proton-transfer reactions, J. Phys. Chem. A., 2018, 122, 8143−8151
- **B. Olasz**, G. Czakó, Uncovering the role of the stationary points in the dynamics of the $F^- + CH_3I$ reaction, Phys. Chem. Chem. Phys., 2019, 21, 1578−1586
- **B. Olasz**, G. Czakó, High-level-optimized stationary points for the $F^-(H_2O) + CH_3I$ system: Proposing a new water-induced double-inversion pathway, J. Phys. Chem. A, 2019, 123, 454−462

Publications related to the thesis

- T. Győri, **B. Olasz**, G. Paragi, G. Czakó, Effects of the level of electronic structure theory on the dynamics of the $F^- + CH_3I$ reaction, J. Phys. Chem. A., 2018, 122, 3353−3364

*In the text of the thesis, the references to my own articles are marked with underlines

Contents

Glossary 5

1 Introduction 7

1.1 About the bimolecular nucleophilic substitution (S_N2) reactions 7

1.2 Investigating the dynamics of chemical reactions 10

1.3 Prior work in the field of chemical reaction dynamics in connection with my research 11

1.4 Goals of the research 12

1.5 The structure of the PhD thesis 13

2 Theoretical background 14

2.1 Schrödinger equations and approximations needed to solve the time-independent Schrödinger equation 14

2.2 Electron correlation methods 16

2.3 The density functional theory (DFT) 19

2.4 Quantum chemical bases 22

3 Development of the potential energy surface (PES) 24

3.1 Geometry optimization and frequency calculation 24

3.1.1 Geometry optimization methods 24

3.1.1 Normal mode analysis 25

3.2 PES development 26

3.2.1 Fitting of the *ab initio* points 26

4 Quasiclassical trajectory (QCT) method 28

4.1 Initial conditions 30

4.1.1 Microcanonical normal mode sampling 30

4.1.2 The orientation and velocities of the reactants 31

4.2 Final conditions 32

4.2.1 Reaction probabilities 32

4.2.2 Initial attack angle 32

4.2.3 Scattering angle 33

4.2.4 Relative translational energy and internal energy 33

4.2.5 Trajectory integration time 34

4.3 Mode-specific (ro)vibrational analysis 34

4.4 Determining configuration of the products 37

5 Results and discussion 38

5.1 Developing of a high-level *ab initio* potential energy surface for the F^- + CH_3I system 38

5.1.1 MOLPRO computational details 42

5.2 Dynamics of the F^- + CH_3I S_N2 and proton-transfer reactions 43

5.3 Deciphering front-side complex formation in S_N2 reactions via dynamics mapping 49

5.4 Stretching vibration is spectator in nucleophilic substitution 53

5.5 Mode-specific quasiclassical dynamics of the F^- + CH_3I S_N2 and proton-transfer reactions 58

5.6 Uncovering the role of the stationary points in the dynamics of the F^- + CH_3I reaction 66

5.7 Electronic structure theory study of the microsolvated $F^-(H_2O)$ + CH_3I S_N2 reaction 73

Summary 85

Acknowledgements 88

References 89

Glossary

S_N2	Bimolecular nucleophilic substitution
DI	Double Inversion
FSA	Front-Side Attack
BSA	Back-Side Attack
PES	Potential Energy Surface
QCT	Quasiclassical Trajectory
TS	Transition State
IRC	Intrinsic Reaction Coordinate
MEP	Minimum Energy Pathway
FC	Frozen Core
AE	All Electron
SP	Single Point Energy Calculation
NMA	Normal Mode Analysis
ZPE	Zero Point Energy
HF	Hartree-Fock
HF-SCF	Hartree-Fock Self Consistent Field
MP2	Second-Order Møller-Plesset Perturbation Theory
CCSD(T)	Coupled Cluster Singles, Doubles and Perturbative Triples
CISD	Configuration Interaction Singles and Doubles
DFT	Density Functional Theory
RMS	Root-Mean-Square

ICS	Integral Cross Section
GB	Gaussian Binning
GTO	Gaussian-Type Orbital
STO	Slater-Type Orbital
ECP	Effective Core Potential
TOP	Trajectory Orthogonal Projection
SVP	Sudden Vector Projection

1 Introduction

1.1 About the bimolecular nucleophilic substitution (S_N2) reactions

Bimolecular nucleophilic substitution (S_N2) reactions are of fundamental importance in chemistry and biochemistry. In preparative organic chemistry, S_N2 reactions are used to change functional groups and are capable to form carbon-carbon bonds, because the cianide ion or the cianide radical can be nucleophile agents, too. In biochemistry, they play an important role for example in the field of the nucleic acids or in the biosynthesis of adrenalin.

The oldest-discovered mechanism of the S_N2 reactions is which called direct rebound in Figure 1.1.[1] This was described by Paul Walden in 1896[2] and usually called Walden inversion. This Walden inversion has a double-well potential energy diagram, because of the ion-dipole complexes in the entrance channel and in the product channel with low energies connecting with a Walden transition state. Figure 1.2[3] shows that these diagrams can be different depending on the exothermicity of the reaction and the height of the central barrier. It is important that exothermic reactions can proceed with and without a significant central barrier, too. Since the description of the Walden inversion, many pathways of the S_N2 reactions have been discovered, as Figure 1.1 shows. The direct stripping mechanism frequently takes place among the S_N2 reaction paths. This pathway starts with attack from the side of the polyatomic reactant and the nucleophile substitutes the leaving group via the usual Walden-inversion transition state, resulting in sideways and forward scattering. The roundabout mechanism[1] is an interesting reaction route which occurs rarer than the stripping. In the case of the roundabout pathway the polyatomic reactant rotates in the neighbourhood of the attacking agent until a transition-state like structure develops. These reactions usually end with inversion so the discovery of the retention mechanisms is particularly interesting. At first, the front-side retention mechanism was described.[4] This mechanism proceeds with a high barrier, so the description of an S_N2 retention mechanism with a lower barrier by Szabó and Czakó was very significant. They discovered this new, so-called double-inversion retention pathway for the F^- + CH_3Cl system.[5] Figure 1.3 shows the most important steps of the double-inversion mechanism. The process starts with a proton abstraction then the generated HF molecule moves to the other side of the CH_2Cl^- unit. Then, the double inversion transition state develops before the HF unit gives the proton back to the CH_2Cl^- unit. The energy of the double inversion transition state is around 16 kcal/mol relative to the reactants, while the relative energy of the front-side transition state is around 31 kcal/mol. Since the HF unit gave back the proton to the CH_2Cl^- unit to the opposite side compared with the side of the CH_3Cl the fluoride ion abstracted the proton, an inversion occurred in this way. After that, a second inversion takes place which is a

traditional Walden inversion process. With two inversions, the final configuration is the same as the initial.

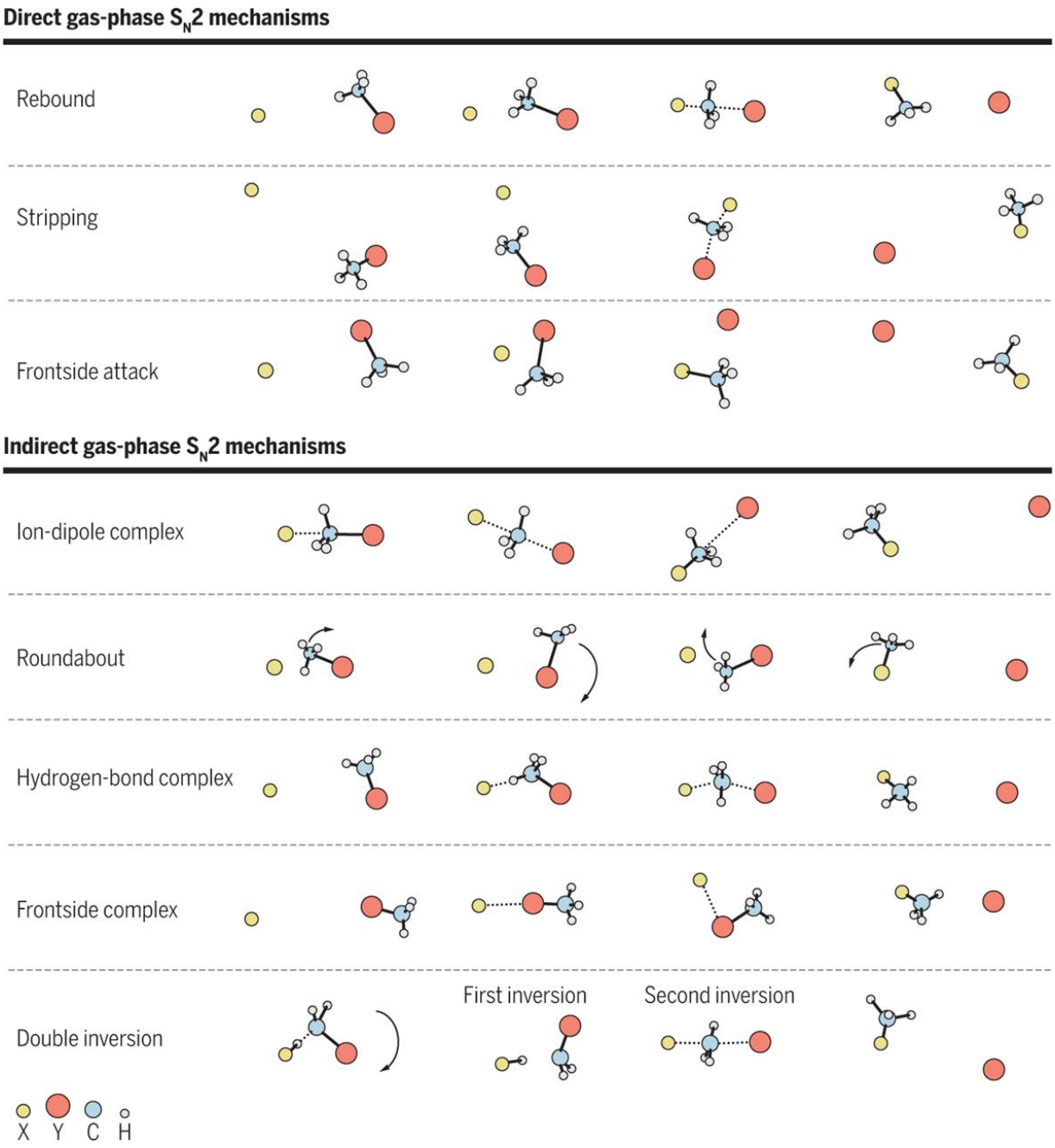

Figure 1.1. Reaction mechanisms belonging to the gas-phase S_N2 reactions[1]

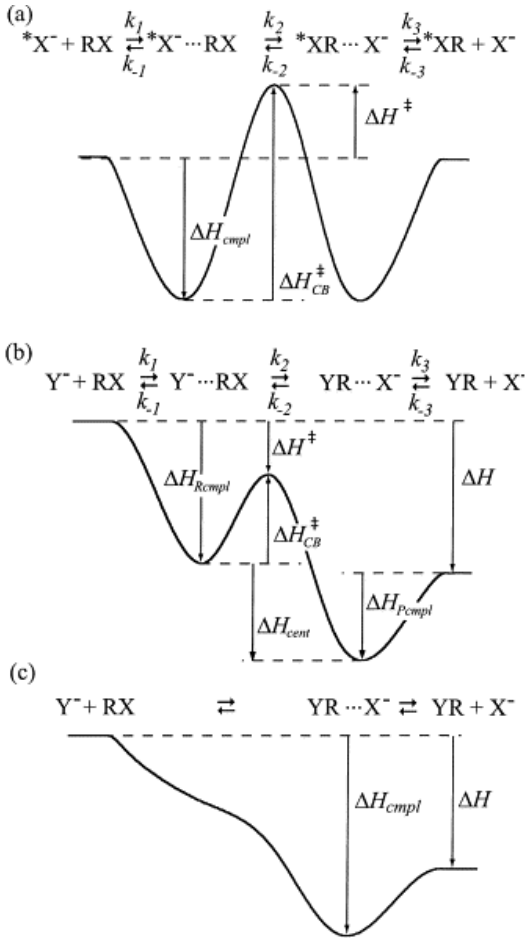

Figure 1.2. Potential energy profiles for (a) a thermoneutral identity double-well S_N2 reaction, (b) an exothermic double-well S_N2 reaction with a significant central barrier, and (c) an exothermic S_N2 reaction without a central barrier, with corresponding energy differences

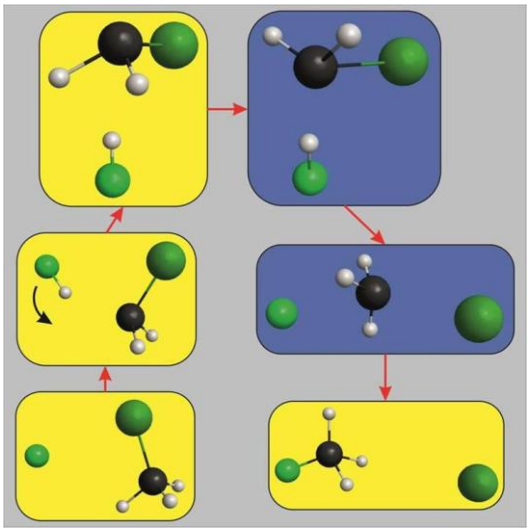

Figure 1.3. Schematic description of the double-inversion mechanism[5]

1.2 Investigating the dynamics of chemical reactions

The investigation of chemical reactions can be experimental or theoretical. In the age of Paul Walden, scientists could investigate these reactions in solution phase, the configuration of the product could be determined, but could not measure internal energy and scattering angle distributions, which are comparable to the theoretical results. Nowadays, with the crossed-beam techniques, this is possible. Above this the attacking angle is adjustable, and with lasers the mode-specific vibrational excitation of the reactants is feasible. Roland Wester and co-workers have been carrying out such crossed-beam experiments for S_N2 reactions for more than a decade.[6,7]

The theoretical studies of the dynamics of chemical reactions have two big classes: the direct dynamical simulations and the analytical potential energy surface-based reaction dynamics computations. The direct dynamics investigations have several disadvantages. Because in every step of the trajectory calculating energy gradients with electronic structure computation method is necessary, this is a rather time consuming procedure. In consequence, with direct dynamics simulations only a few trajectories (usually less than a thousand) can be run and high-level electronic-structure methods can not be applied. Therefore, I used the other approach. Here, the development of an analytical potential energy surface (PES) is a time-consuming procedure, although with our newly developed programs this work is mainly can be done by the computer. The advantage of this method is that after the development of the PES, millions of trajectories can be run efficiently, because here the energy gradients can be directly calculated from the analytical PES function. This feature allows the discovery of the rare reaction pathways and the determination of statistically accurate dynamics results. Furthermore, another advantage is that the PES points can be computed with high-level electronic-structure methods; thus, the analytical PES-based dynamics is more efficient and more accurate than the traditional direct dynamics.

On these potential energy surfaces, quasiclassical trajectory (QCT) simulations are usually used to investigate the dynamics of chemical reactions. These simulations use the laws of the classical mechanics, which is reasonable due to the relatively big masses of the atoms, ions, and molecules (nuclei) compared to the mass of the electron. In a quasiclassical simulation, the vibrational energy levels of the reactants are set according to the rules of the quantum mechanics. In addition, by the analysis of the trajectories, the so called zero-point energy (ZPE) violation, that the product molecules whether have at least their ZPEs, is checkable. More details about the QCT method are described in chapter 4.

1.3 Prior work in the field of chemical reaction dynamics in connection with my research

The development of analytical potential energy surfaces for reactive polyatomic systems is a relatively new scientific field, especially in the case of S_N2 reactions. Hase and co-workers developed a PES for the $F^- + CH_3Cl$ S_N2 reaction using approximately 1000 MP2 potential energy values calculated for the stationary-point geometries and other characteristic geometries.[8] The calculated rate constants of the $F^- + CH_3Cl$ reaction show only qualitative agreement with the experimental rate constants depending on the temperature and the translational energy. This model PES was used for another study where the effect of the excitation of the C-Cl stretching mode was investigated.[9] After these old analytical PES-based studies carried out in 1997-1998, the Hase group has been using direct dynamics to investigate S_N2 reactions.

Potential energy surface developments have a long history involving many research groups. For example, Espinosa-Garcia and co-workers developed semiempirical PESs, which use analytically derived expressions describing atomic motions, for instance, the London-Eyring-Polanyi function to describe the stretching modes in the case of the $F + CH_4$ reaction.[10] Some of the results derived from these semiempirical surfaces agree reasonably well with experimental results but others, for example, the rotational energy distributions and the product energy partitions do not agree well with the experiments in every case. To my work the *ab initio*-based PES developments are related the most, which are initiated by Bowman, Braams, Czakó, Guo, Zhang, and others, mostly in the case of atom + water and methane reactions.[11,12,13,14] For S_N2 reactions this high-level *ab initio* PES-based dynamics approach was first proposed by Szabó and Czakó in 2013.[15]

For the $F^- + CH_3I$ system which I investigated during my PhD work several studies were reported before our work, but an appropriate potential energy surface has not existed earlier. Mainly stationary point searches[16,17] and direct dynamics simulations[18] were carried out earlier in order to investigate this system. Considering the advances of the analytical potential energy surfaces, the development of a full-dimensional surface for the $F^- + CH_3I$ system computed at high-level of *ab initio* theory seemed to be an important challenge for my PhD work.

Experimental studies also exist in connection with this reaction. The crossed-beam results of Roland Wester and his research group in Innsbruck were comparable with our theoretical results.[19,20]

1.4 Goals of the research

After the discovery of the double-inversion pathway in 2015,[5] it became important to uncover this new retention mechanism for other systems. My target was firstly the F^- + CH_3I system. Beside the double-inversion route, the other pathways such as the Walden inversion or direct rebound, the direct stripping, which result in inversion, the front-side attack mechanism and the abstraction route are also important.

The reaction can be promoted by vibrational and perhaps rotational excitation. One of my goals was the investigation of the reaction with vibrationally excited CH_3I molecule. Among the vibrational modes, the modes which couple with the reaction coordinate the most efficiently have presumably the most important role promoting the reaction.

Due to the fact that S_N2 reactions usually take place in solution phase in the routine, the investigation of the hydrated F^- + CH_3I system was among my targets.

I planned to collaborate with an experimental research group in Innsbruck leading by Professor Roland Wester. A joint experimental-theoretical study may provide unprecedented insights into the mode-specific dynamics of the F^- + CH_3I reaction.

In order to achieve the above described goals, I was to develop a high-level *ab initio* PES for the F^- + CH_3I reaction, which describes the different inversion and retention S_N2 pathways as well as the proton-transfer channel. With this new PES at hand I could investigate the dynamics of the title reaction using the quasi-classical trajectory method.

1.5 The structure of the PhD thesis

After the Introduction presented in chapter 1, in chapter 2, I shortly describe the theoretical background of the electronic structure methods, which are important tools to characterize and develop PESs. I do not write full deduction to the equations just the starting equations and the final results.

Chapter 3 is about the development of potential energy surfaces which starts with the development of a first surface, then the correction of the surface in multiple iterative steps. There is a subsection about the fitting of the PES points. Chapter 4 describes the theory of the quasiclassical trajectory simulations with the initial conditions needed to start the QCT simulation and the final conditions calculated from the final parameters of trajectories.

In chapter 5 the main results of my doctoral work are described and in every case comparisons with other studies are also presented. References to my own papers are marked with underlines. The list of publications covered in this thesis is given at the beginning of the dissertation on page 2.

The dissertation ends with Summary, Acknowledgements, and References.

2 Theoretical background

2.1 Schrödinger equations and approximations needed to solve the time-independent Schrödinger equation

The time-dependent Schrödinger equation

$$i\hbar\frac{\partial\Psi}{\partial \mathrm{t}} = \hat{\mathrm{H}}\Psi \tag{1}$$

is one of the axioms of quantum mechanics. In this expression, $\hbar = \frac{h}{2\pi}$, where h is the Planck constant, the i is the imaginary unit, Ψ is the wave function which is the state function of the system, and $\hat{\mathrm{H}}$ is the so-called Hamilton-operator. In general, operators make special objects (functions, matrices, vectors, etc.) from the same type of objects. The non-relativistic Hamilton operator

$$\hat{\mathrm{H}} = -\frac{\hbar^2}{2m}\sum_{i=1}^{N_\mathrm{e}}\nabla_i^2 - \frac{\hbar^2}{2}\sum_{a=1}^{N_\mathrm{n}}\frac{\nabla_\mathrm{i}^2}{m_a} + \frac{\mathrm{e}^2}{4\pi\epsilon_0}\sum_{i<j=1}^{N_\mathrm{e}}\frac{1}{r_{ij}} - \frac{\mathrm{e}^2}{4\pi\epsilon_0}\sum_{a=1}^{N_\mathrm{n}}\sum_{i=1}^{N_\mathrm{e}}\frac{Z_\mathrm{a}}{r_{ai}} + \frac{\mathrm{e}^2}{4\pi\epsilon_0}\sum_{a<b=1}^{N\mathrm{n}}\frac{Z_a Z_b}{r_{ab}} \tag{2}$$

consists of five terms. The Hamilton-operator of a system consists of N_e electrons N_n nuclei. The first term is the kinetic energy operator of the electrons, the second is the kinetic energy operator of the nuclei, the third is the potential energy operator for the electron-electron repulsion, the fourth is the nucleus-electron attraction, the fifth is the nucleus-nucleus repulsion. m denotes the masses of the particles, ∇_i^2 is the nabla square or Laplace-operator which is the second derivative operator with respect to the space coordinates. The r_{xy} expressions are the distances of particles, the Z_x values are the atomic numbers, and e denotes the charge of an electron which is the atomic unit of the charge.

The more commonly used time-independent Schrödinger equation

$$\hat{\mathrm{H}}\Psi = E\Psi\,, \tag{3}$$

which is suitable to calculate the energy (E) of a system, is derived from the time-dependent one. Eq. (3) is an eigenvalue-equation. On one side of the eigenvalue-equations there is a function after an operator, on the other side there is the same function multiplied by a constant which is called eigenvalue. In the equation (3) the eigenvalue is the energy. In the case of real chemical systems except the hydrogen atom, analytical solution of the Schrödinger equations does not exist. The numerical solution is complicated; therefore, approximations have to be introduced.

One can reduce the number of variables by using of the electron density instead of the wave function because the electron density has only three variables, which are the three spatial coordinates. The electron density methods will be discussed later in this chapter.

One can simplify the form of the wave function by approximations. One approximation is the neglection of the relativistic effect spin-orbit coupling. If we use this approximation, the wave function can be written as the product of the spin wave function and the spatial wave function. The

other approximation which is generally used is the Born-Oppenheimer approximation[21] which states that the motion of the nuclei and the electrons can be treated separately, because the heavy nuclei follow very slowly the motion of the electrons which are at least three orders of magnitude lighter than the nuclei. The electrons follow the motion of the nuclei immediately. In consequence, we can fix the positions of the nuclei and solve only the electronic Schrödinger equation to get the energy of the molecule. These two approximations make little neglections in most cases, the spin-orbit coupling is significant only in the case of radicals, and the Born-Oppenheimer approximation is also widely useable, this will be discussed in detail in chapter 3.

The third approximation is the separation of the motion of the electrons. This is an incorrect assumption because the motion of the electrons is correlated. But firstly, we use this assumption so the wave function can be written as the product of the one-electron state functions and by using an average potential of the electrons on every electron. In this simple product form, the wave function does not fulfil the Pauli principle, because if we change two electrons, the wave function does not change its sign. We can choose an arbitrary linear combination of the wave functions, which is antisymmetric according to the Pauli principle, for example:

$$\Psi=\frac{1}{\sqrt{2}}[\varphi_1(1)\varphi_2(2)-\varphi_1(2)\varphi_2(1)], \tag{4}$$

This is an expansion of a determinant, so in an *N*-electron case we can choose also a determinant as a wave function with the appropriate normalization coefficient:

$$\Psi=\frac{1}{\sqrt{N!}}\begin{vmatrix}\varphi_1(1) & \varphi_2(1) & & \varphi_N(1)\\ \varphi_1(2) & \varphi_2(2) & & \varphi_N(2)\\ \vdots & & \ddots & \\ \varphi_1(N) & \varphi_2(N) & & \varphi_N(N)\end{vmatrix} \tag{5}$$

The problem to solve after that is the proper form of the effective potential of the electrons. To find this, the variational principle can be used, which states that the energy functional:
$E[\Psi]=<\Psi|\hat{H}|\Psi>$ in the $\Psi=\Psi_0$ case gives the lowest energy, where Ψ_0 is the ground-state wave function. This principle is used in the case of the deduction of Hartree-Fock equations.[22] The derivation starts from the equation

$$E[\Psi] = <\Psi|\hat{\mathrm{H}}|\Psi> =$$

$$\mathrm{h}_0 + \sum_{i=1}^{N}\int \psi_i^*(\mathbf{x}_1)\mathrm{h}_1(\mathbf{x}_1)\psi_j(\mathbf{x}_1)\mathrm{d}\mathbf{x}_1 + \frac{1}{2}\sum_{i,j=1}^{N}\int \psi_i^*(\mathbf{x}_1)\psi_j^*(\mathbf{x}_2)\frac{1-\mathrm{P}_{12}}{r_{12}}\psi_i(\mathbf{x}_1)\psi_j(\mathbf{x}_2)\mathrm{d}\mathbf{x}_1\,\mathrm{d}\mathbf{x}_2 \quad (6)$$

and gives the following expression as a result:

$$\hat{\mathrm{F}}(i) = \hat{\mathrm{h}}_1(i) + \sum_{j=1}^{n}\langle\varphi_j(j)|\hat{\mathrm{h}}_2(ij)(1-\hat{\mathrm{P}}_{ij})\varphi_j(j)\rangle \quad (7)$$

Eq. (7) defines the Fock operator, where the $\hat{\mathrm{h}}_1$ operator is the one-electron operator, the $\hat{\mathrm{h}}_2$ operator is the two-electron Coulomb operator, $\hat{\mathrm{P}}_{ij}$ is the permutation operator, which interchanges two electrons. The Fock operator contains all the one-electron functions, too. In consequence, the Hartree-Fock equations can be solved iteratively, starting with a set of one-electron functions, which can be used to build a first Fock operator. We can solve the equation with this operator and we get a set of new one-electron orbitals. This iterative process can be continued until the eigenvalues and the eigenvectors do not change significantly in two consecutive step. This is the so-called HF-SCF (Hartree-Fock Self Consistent Field) method.

2.2 Electron correlation methods

The Hartree-Fock (HF) method is based on the idea of the wave function which is the product of one-electron functions. This is the independent particle model which does not take the correlated motion of the electrons into account. One way to solve this problem is to consider the electronic correlation by a perturbative correction. The perturbation calculation can be used in quantum mechanics if the Hamilton operator differs not significantly from a reference Hamilton operator. The $\hat{\mathrm{H}}$ Hamilton operator can be written by using the $\hat{\mathrm{H}}^{(0)}$ reference operator and a W perturbation:

$$\hat{\mathrm{H}} = \hat{\mathrm{H}}^{(0)} + \lambda\mathrm{W} \quad (8)$$

The well-known Rayleigh-Schrödinger perturbation theory gives the further corrected energy and wave functions, where the '*i*' parameter is the order of the perturbation:

$$E = E^{(0)} + \sum_{i=0}^{\infty}\lambda^i\left\langle\psi^{(0)}\middle|\mathrm{W}\psi^{(i-1)}\right\rangle \quad (9)$$

$$\psi^{(1)} = \sum_i \frac{\langle\psi_i{}^{(0)}|\mathrm{W}\psi^{(0)}\rangle}{E^{(0)}-E_i{}^{(0)}}\psi_i{}^{(0)} \quad (10)$$

In quantum chemistry, the Møller-Plesset perturbation method[23] can be applied which uses the sum of the Fock operators as the non-perturbated (reference) Hamilton operator. There are MP2, MP3, MP4 etc. methods depending on the order of the perturbation, but only the MP2 and occasionally the MP4 methods are used because the MP1 does not changes the Hartree-Fock energy, and the

MP3 method does not surely gives better results than MP2 and demands more computational time. The MP4 corrects the HF energy but demands significantly more computation time than MP2 and does not gives much better energies. The second-order energy correction can be written as:

$$E^{(2)} = \sum_i \sum_{<j} \sum_a \sum_{<b} \frac{|\langle \varphi_{ij}^{ab} | W\varphi^{(0)} \rangle|^2}{\varepsilon_a + \varepsilon_b - \varepsilon_i - \varepsilon_j} \tag{11}$$

In the (11) expression, ε values are eigenvalues of the Fock operator, $\varphi^{(0)}$ is the Hartree-Fock reference wave function and φ_{ij}^{ab} is derived from $\varphi^{(0)}$ with excitation discussed in the next section. It is need to be mentioned here that these excitations do not have physical meaning.

The following electronic correlation methods are based on the idea of excited determinants, which were mentioned above. Equation (12) shows an example for such excitations.

$$\varphi_0 = \frac{1}{\sqrt{N!}} \begin{vmatrix} \varphi_1(1) & \varphi_2(1) & & \varphi_N(1) \\ \varphi_1(2) & \varphi_2(2) & & \varphi_N(2) \\ \vdots & & \ddots & \\ \varphi_1(N) & \varphi_2(N) & & \varphi_N(N) \end{vmatrix} \rightarrow \varphi_2^{N+1} = \frac{1}{\sqrt{N!}} \begin{vmatrix} \varphi_1(1) & \varphi_{N+1}(1) & & \varphi_N(1) \\ \varphi_1(2) & \varphi_{N+1}(2) & & \varphi_N(2) \\ \vdots & & \ddots & \\ \varphi_1(N) & \varphi_{N+1}(N) & & \varphi_N(N) \end{vmatrix} \tag{12}$$

The wave function can be written now as the linear combination of different determinants as

$$\psi = \varphi_0 + \sum_i \sum_a c_i^a \varphi_i^a + \sum_i \sum_{<j} \sum_a \sum_{<b} c_{ij}^{ab} \varphi_{ij}^{ab} + \sum_i \sum_{<j} \sum_{<k} \sum_a \sum_{<b} \sum_{<c} c_{ijk}^{abc} \varphi_{ijk}^{abc} + \dots \tag{13}$$

With the proper choice of the linear coefficients we can take the electronic correlation into account. The linear coefficients can be calculated directly from the (14) equations, where the S_{kj} elements are the elements of the overlap integral matrix.

$$\sum_{j=1}^{n} \boldsymbol{c_j} \left(\boldsymbol{H_{kj}} - \boldsymbol{E S_{kj}} \right) = \boldsymbol{0} \; ; \; \boldsymbol{S_{kj}} = \langle \boldsymbol{\varphi_k} | \boldsymbol{\varphi_j} \rangle \tag{14}$$

Figure 2.1 shows the CI matrix of the Hamilton operator. The $\hat{H}_{10}$ and the $\hat{H}_{01}$ matrix elements are zero due to the Brillouin's theorem. The other white matrix elements vanish because each term of the $\hat{H}$ operator depends only on the coordinates of no more than two electrons, so the determinants which differ in more than two electron's coordinates, can not be taken into account.

If we used an untruncated CI series expansion, we would get the exact solution of the nonrelativistic Schrödinger equation corresponding to a given basis set. This is impossible in the case of real calculations, so we have to truncate it. If we take only the first-order excitations into account, this will be the CIS method. If we take only the second-order excitations into account, this will be the CID method. If we take the first-order and the second-order excitations into account, this will be the CISD method. However, there is a problem with the configuration interaction method, that it does not fulfill the criteria of size consistency if we use the truncated CI expansion. This derives from that the product of two different wave functions, which is the description of two non-interacting

fragments contains higher-order excitations than the wave function of the molecule consists of the two fragments. In consequence, the configuration interaction method is rarely used nowadays.

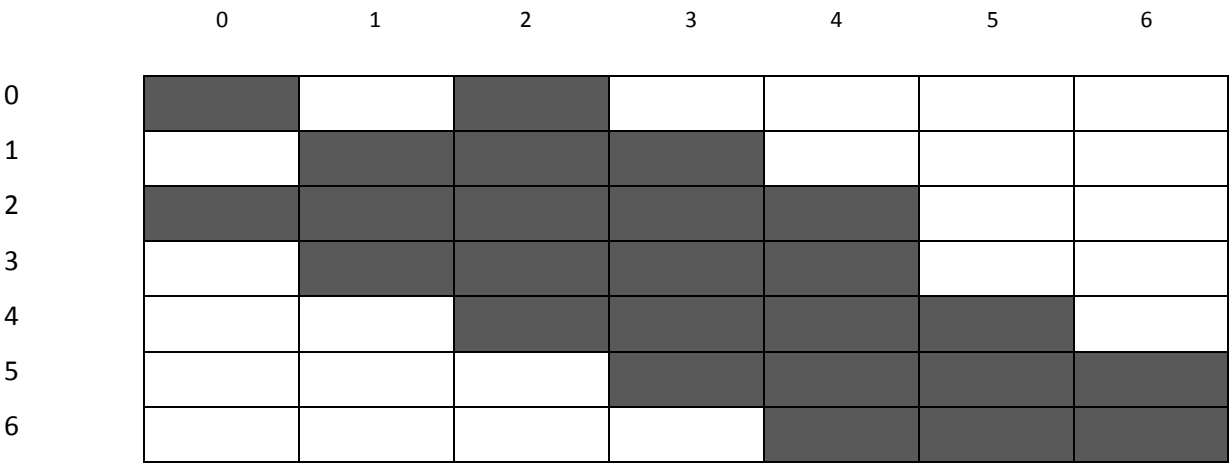

Figure 2.1.: Structure of the CI matrix

The coupled cluster method[24] uses the following expression for the wave function:

$$\psi = e^{\hat{T}} \varphi_0, \tag{15}$$

where the $\hat{T}$ operator can be written, for example, as:

$$\hat{T} = \hat{T}_1 + \hat{T}_2 \tag{16}$$

This $\hat{T}$ operator makes first-order and second-order excitations from the φ_0 wave function. Here, the expression of $e^{\hat{T}}$ is

$$e^{\hat{T}} = \hat{1} + \hat{T}_1 + \hat{T}_1\hat{T}_1 + \hat{T}_2 + \frac{1}{3!}\hat{T}_1\hat{T}_1\hat{T}_1 + \frac{1}{2}\hat{T}_2\hat{T}_1 + \frac{1}{2}\hat{T}_1\hat{T}_2 + \cdots. \tag{17}$$

In Eq. (17), the last three terms makes third-order excitations. The size consistency of coupled cluster (CC) method derives from the fact that the (17) exponential contains higher-order excitations than the $\hat{T}$ operator itself, so the wave function of one molecule contains as high-order excitations as the product of two different wave function (the description of two non-interacting particles). Here we started from first-order and second-order excitation operator, so this is the CCSD method. CCSD(T) is a popular method which makes a perturbative correction from the CCSD result. It is needed to mention that the CC method is better than the CI method not just due to its size consistency but due

to the accuracy of the method. This means that, for instance, the CCSD method usually gives better results than CISD. In addition to this, the computing time is similar in the case of the two methods.

The explicitly correlated F12 methods (F12a and F12b) use interelectronic distances in the Hamilton-operator instead of Cartesian coordinates. With the use of F12, the processes become more time-consuming but the results will be more precise especially in the case of using smaller basis sets.[25] So, the basis set convergence in the case of F12 methods is much better.

2.3 The density functional theory (DFT)

The DFT is an alternative approach in the field of quantum chemistry. The main advantage of this method is that the electron density has only three variables, which is the three spatial coordinates. The electron density function can be obtained from the electronic wave function of the system as:

$$\rho(\mathbf{r}) = \mathrm{N} \int \psi^*(\mathbf{r}, \omega_1, \dots, \mathbf{r}_N, \omega_N)\psi(\mathbf{r}, \omega_1, \dots, \mathbf{r}_N, \omega_N) d\omega_1, d\mathbf{r}_2 \dots, d\mathbf{r}_N, d\omega_N \quad (18)$$

Here, we left out the three spatial coordinates of the first electron from the integration but we can leave out either due to the fact that the electrons are undistinguishable.

The question is that this electron density function whether can be used instead of the electronic wave function or not. The first Hohenberg-Kohn theorem answers this question, which states that the *v(r)* external potential is a unique functional of the ρ(r) ground state electron density aside from an additive constant. The theorem can be proved through the correspondence between the *v(r)* external potentials and the ground-state wave functions and the correspondence between the ground-state wave functions and the ρ(r) ground state electron densities. In consequence, the ground-state electron density can be used instead of the ground-state electronic wave functions.

There is a second Hohenberg-Kohn theorem which declares for arbitrary electron density functions that

$$E[\rho] \geq E[\rho_0], \quad (19)$$

where ρ_0 is the exact ground-state electron density. This theorem allows determining the ground-state electron density by the variation of the electron density in the $E[\rho]$ functional.

We can write the energy functional in this form:

$$E[\rho] = T[\rho] + W[\rho] + V[\rho], \quad (20)$$

where $T[\rho]$ is the kinetic energy functional, the $W[\rho]$ is the electron-electron interaction functional and $V[\rho]$ is the nucleus-electron interaction functional. Theoretically, we can get the ground-state

energy and electron density by the variation of this $E[\rho]$ functional due to the second Hohenberg-Kohn theorem. But the form of the $T[\rho]$ and $W[\rho]$ functionals are unknown in general. These functionals can only be described in the independent particle model similarly to the Hartree-Fock equations:

$$E_{\mathrm{NI}}[\rho] = T_{\mathrm{NI}}[\rho] + W[\rho] + V_{\mathrm{NI}}[\rho] = \langle\psi|\mathrm{H}_{\mathrm{NI}}|\psi\rangle = \sum_{i=1}^{N}\int \varphi_i^*(\mathrm{r})\left(-\frac{\Delta}{2}\right)\varphi_i(\mathrm{r})\mathrm{dr} + \int \rho(\mathrm{r})v(\mathrm{r})\mathrm{dr} + \int \rho(\mathrm{r})v_{\mathrm{NI}}(\mathrm{r})\mathrm{dr}, \quad (21)$$

where NI means non-interacting. The (20) energy functional can be written in the following form:

$$E[\rho] = T_{\mathrm{NI}}[\rho] + V[\rho] + W[\rho] + T[\rho] - T_{\mathrm{NI}}[\rho] \quad (22)$$

Here, the first two terms are known. In the W[ρ], the Coulomb-interaction term can be expressed:

$$W_{\mathrm{Coul}}[\rho] = \int \frac{\rho(\mathrm{r}_1)\rho(\mathrm{r}_2)}{r_{12}}\mathrm{dr}_1\mathrm{dr}_2 \quad (23)$$

Thus, the last three terms can be written in the following form:

$$W[\rho] + T[\rho] - T_{\mathrm{NI}}[\rho] = W_{\mathrm{Coul}}[\rho] + W[\rho] - W_{\mathrm{Coul}}[\rho] + T[\rho] - T_{\mathrm{NI}}[\rho] \quad (24)$$

The last four terms on the right side of the equation (24) is the $W_{\mathrm{EC}}[\rho]$ exchange-correlation functional. The energy functional will be the following:

$$E[\rho] = T_{\mathrm{NI}}[\rho] + V[\rho] + W_{\mathrm{coul}}[\rho] + W_{\mathrm{EC}}[\rho] \quad (25)$$

We can express the electron density with the one-electron wave functions:

$$\rho = \sum_{i=1}^{N}\varphi_i^*\varphi_i \quad (26)$$

We search the minimum of this expression with a side condition $\int \rho(\mathrm{r})\mathrm{dr} = N$ using the method of Lagrange multipliers.

Finally, we get the Kohn-Sham equations:[26]

$$\left\{\Delta_{\mathrm{r}1} + \sum_{j=1}^{N}\int \frac{\varphi_j^*(\mathrm{r}_2)\varphi_j(\mathrm{r}_2)}{r_{12}}\mathrm{dr}_2 + v(\mathrm{r}_1) + v_{\mathrm{EC}}(\mathrm{r}_1)\right\}\varphi_i(\mathrm{r}_1) = \varepsilon_i\varphi_i(\mathrm{r}_1) \quad (27)$$

The big problem here that the following derivative is unknown:

$$v_{\mathrm{EC}} = \frac{\delta W_{\mathrm{EC}}[\rho]}{\delta \rho} \tag{28}$$

In contrast to the Hartree-Fock equations, the Kohn-Sham equations are exact, does not contain any approximations. The problem is that the form of the $W_{\mathrm{EC}}[\rho]$ functional and in consequence the v_{EC} energy is unknown. Therefore, the main challenge in the field of the density functional theory is the determination of this functional. The first functionals were determined by Dirac and Slater, who used the homogeneous electron gase approximation. This was the Xα exchange-correlation functional:

$$W_{\mathrm{EC}}[\rho] = E_{\mathrm{x}}^{\mathrm{LDA}}[\rho] = -\frac{3}{4}\left(\frac{3}{\pi}\right)^{1/3} \int \rho(\mathbf{r})^{4/3} \mathrm{d}\mathbf{r} \tag{29}$$

The homogeneous electron gase approximation is appropriate for the solid states, but in the case of the molecular systems, the changes of the electron density must be taken into account. This is why the gradient corrected GGA (Generalized Gradient Approach) functionals were developed. The B97 functional is a frequently used GGA functional. Other types of the DFT functionals are the hybride functionals which are the sum of the HF-type exchange and other type exchange-correlation terms with fixed coefficients:

$$E_{\mathrm{XC}}[\rho] = \frac{1}{2} E_{\mathrm{x}}^{\mathrm{HF}} + \frac{1}{2} \tilde{E}_{\mathrm{xc}} \,. \tag{30}$$

Becke's half and half functional[27] contains a Slater-type Xα exchange-correlation functional beside the HF-type exchange term. The B3LYP functional

$$E_{\mathrm{xc}}^{\mathrm{B3LYP}}[\rho] = (1-a)E_{\mathrm{x}}^{\mathrm{SGKS}}[\rho] + aE_{\mathrm{x}}^{\mathrm{HF}}[\rho] + bE_{\mathrm{x}}^{\mathrm{B88}}[\rho] + cE_{\mathrm{c}}^{\mathrm{LYP}}[\rho] + (1-c)E_{\mathrm{c}}^{\mathrm{VWN}}[\rho] \tag{31}$$

is a famous hybride functional which contains correlation terms and gradient correction terms beside the terms which are also included in the Becke's half and half functional. The B2PLYP is hybride functional with MP2 correlation term. The PBE0 is a famous functional which does not contain any empirical parameter. In contrast, the M06 functional[28] contains lots of empirical parameters and contains dispersion interaction correction term.

2.4 Quantum chemical bases

Quantum chemical basis functions are used in the real quantum chemical computations in the case of wave function methods and DFT-methods, too. There are two types of these basis functions, the Slater-type orbitals and the Gaussian-type orbitals as shown in Figure 2.2. The Slater-type orbitals give the better results but the other advantages of the Gaussian-type orbitals make them more preferred. One benefit of the Gaussian-type functions that they can be integrated analytically. The other important advantage is that the product of two Gaussian-type orbital is also a Gaussian-type orbital which is very important if we have to calculate two-electron integrals.

The minimal basis is one basis function to each atomic orbital. The DZ, TZ, QZ etc. basis means two-times more, three-times more and four-times more basis functions than the functions of the minimal basis set. The linear combinations of the Gaussian-type orbitals are frequently used. The quality of the basis functions obtained in this way is similar to the Slater-type basis functions. These so-called contracted basis functions have the computational benefits of the Gaussian-type orbitals. The Gaussian-type orbitals in the linear combination are called primitive Gaussian-type basis functions. The STO-*n*G basis set

$$\chi_{\mathrm{STO}} = \sum_{i=1}^{n} d_i g_i \tag{32}$$

is a minimal basis with one "STO" to each atomic orbital from *n* Gaussian-type orbital.

In the case of the split valence basis[29] the core shells are of single-zeta quality, the valence shells are of DZ or TZ qualities. For example, in the 4-21G basis the core orbitals are of single-zeta quality with the combination of four Gaussian-type orbitals, the valence shell are of double-zeta quality, with one contracted basis from two Gaussian-type orbitals, with one from one Gaussian-type orbital. The polarization functions simulate the derivatives of the basis functions; in consequence they are informative to the local surroundings of the atom. The diffuse functions are slowly decaying functions so they describe well the long-distance interactions. In the case of split valence basis sets polarization and diffuse functions are denoted by * and +, respectively. The most sophisticated basis sets are the Dunning-kind correlation-consistent (cc) functions that are optimized to the electronic correlation calculations.[30] In this case diffuse functions are denoted by "aug" and polarization functions are always involved in the basis sets. Thus, for instance, the aug-cc-pVDZ basis is a correlation-consistent, polarized, valence double-zeta basis set augmented with diffuse functions.

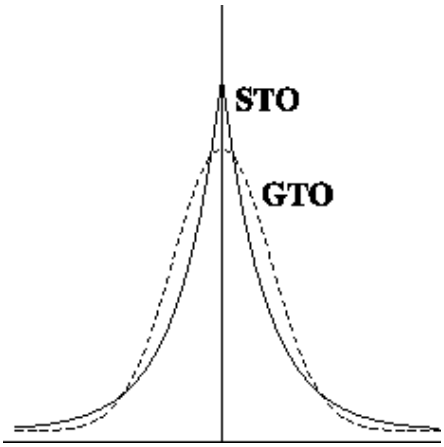

$$\chi_{\mathrm{STO}} = N r^{n-1} \exp(-\xi r)\, Y_l^m(\vartheta, \varphi)$$

$$g_{kpq} = N x^k y^p z^q \exp\left(-\xi r^2\right)$$

Figure 2.2.: Slater-type orbital and Gaussian-type orbital. *n* is the effective quantum number, *N* is the normalization factor, *r* is the distance from the nucleus, *x*, *y*, and *z* are Cartesian coordinates and $Y_l^m(\vartheta, \varphi)$ is spherical function which is similar to the eigenfunction of the H atom's angular momentum operator. In the case of the STO-s the $Y_l^m(\vartheta, \varphi)$ term, in the case of Gaussian-type orbitals the $x^k y^p z^q$ part describes the angular dependence.

3 Development of the potential energy surface (PES)

3.1 Geometry optimization and frequency calculation

3.1.1 Geometry optimization methods

In order to find a stationary point on a potential energy surface, the Newton's method[31] or similar procedures can be applied. The Newton's method (also called Newton-Raphson method) is an iterative process which is used for finding the root of functions or optimizing a geometry. The process is based on the idea that if we choose a value not far away from the solution or a geometry not far away from the stationary point we will be able to get closer and closer to the exact solution or structure by using the derivative of the function or the Hessian matrix:

$$\mathbf{H} = \begin{pmatrix} \frac{\partial^2 V(\mathbf{x})}{\partial x_1 \partial x_1} & \frac{\partial^2 V(\mathbf{x})}{\partial x_1 \partial x_2} & \cdots \\ \frac{\partial^2 V(\mathbf{x})}{\partial x_2 \partial x_1} & \frac{\partial^2 V(\mathbf{x})}{\partial x_2 \partial x_2} & \cdots \\ \vdots & \vdots & \ddots \end{pmatrix} \tag{33}$$

As seen in Eq. (33) the Hessian matrix contains the second derivatives of the potential.

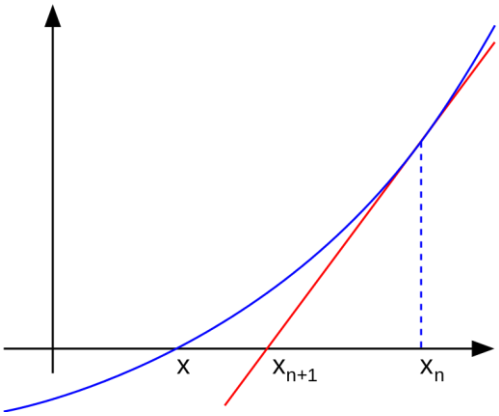

Figure 3.1.: Newton's procedure in the case of a one-variable function

Figure 3.1 illustrates one step of the Newton's procedure in the case of a one-variable function. If we would like to find the minimum of a function, first we need for the derivative of the function labelled with red in Figure 3.1. The iterative procedure goes through the equations

$$f'(x_n) = \frac{\Delta y}{\Delta x} = \frac{f(x_n)-0}{x_n - x_{n+1}} = \frac{0-f(x_n)}{x_{n+1}-x_n} \tag{34}$$

and

$$x_{n+1} = x_n - \frac{f(x_n)}{f'(x_n)}\,. \tag{35}$$

In the case of the geometry optimization procedure another type of the Newton-method is used which uses the Taylor expansion instead of the simple derivative:

$$V(\mathbf{x}_i + \Delta\mathbf{x}) = V(\mathbf{x}_i) + \Delta\mathbf{x}V'(\mathbf{x}_i) + \frac{1}{2}\Delta\mathbf{x}^{\mathrm{T}}V''(\mathbf{x}_i)\Delta\mathbf{x} + (\mathcal{O}|\Delta\mathbf{x}|^3) \tag{36}$$

This is the Taylor polynom around the initial $\mathbf{x}_i$ position where the first and the second derivative of the *V* potential is the gradient vector **g**(**x**$_i$) and the **H**(**x**$_i$), respectively and the $\mathcal{O}$ is the Lagrange remainder. Similar to the case of the one-variable function, the values of the derivatives are

$$\mathrm{grad}[V(\mathbf{x}_i + \Delta\mathbf{x})] = \mathbf{g}(\mathbf{x}_i) + \Delta\mathbf{x}\mathbf{H}(\mathbf{x}_i) + (\mathcal{O}|\Delta\mathbf{x}|^2) = \mathbf{0}\,. \tag{37}$$

Because the $(\mathcal{O}|\Delta\mathbf{x}|^2)$ term can be neglected we can get:

$$\Delta\mathbf{x} = -\mathbf{H}(\mathbf{x}_i)^{-1}\mathbf{g}(\mathbf{x}_i) \tag{38}$$

Computing the inverse of the Hessian matrix can be a time-comsuming procedure. The modern electronic structure programs use the quasi-Newton methods which evaluate the Hessian approximately in the beginning of the optimization then modify it at every step.

3.1.1 Normal mode analysis

We convert the **H** matrix to the **F** matrix

$$\mathbf{F} = \mathbf{M}^{-1/2}\mathbf{H}\mathbf{M}^{-1/2}\,, \tag{39}$$

which contains mass-weighted coordinates. The diagonal elements of the **H** or **F** matrix are always positive and the magnitudes of them depend on the forces along the coordinates. The nondiagonal elements depend on the effect of the change of either coordinate on the change of the other coordinate. If the $\frac{\partial^2 V(x)}{\partial x_i \partial x_j}$ element is positive, it means that the stretch of the x_i coordinate reduces the x_j coordinate.

Using the normal mode directions and frequencies, $\mathbf{l}_i$ and ω_i, the following equations can be written:[32]

$$\mathbf{F}\mathbf{l}_i = \omega_i^2 \mathbf{l}_i \tag{40}$$

$$\mathbf{l}_i \mathbf{l}_j = \delta_{ij} \tag{41}$$

The eigenvalues of the **F** matrix are apparently the squares of the frequencies. These eigenvalues can show the characters of the stationary points, because if all of the eigenvalues are positive, the stationary point will be a minimum, and if one eigenvalue is negative, the others are all positive, the stationary point is a first-order saddle point. In the case of the description of chemical reactions, these two types are the most important.

3.2 PES development

The development of the potential energy surface starts with finding the stationary points for the reaction. Displacing the stationary point structures we can collect the geometries for the first surface. To obtain an analytical potential energy function, after the energy calculations, fitting of the points is necessary.

The situation is more complicated if a system has several real electronic states. If the energies of one state are lower than the energies of the other state on certain regions of the PES, but in the case of the other regions another state has lower energies, there will be a crossover point called conical intersection in the crossing point of the two regions.

The stationary points define the minimum energy path of the reaction which is the lowest energy pathway from the first-order saddle point which has the highest energy among the stationary points along the reaction route, to the reactants and the products. The minimum energy path (MEP) in mass-weighted coordinates is the intrinsic reaction coordinate (IRC). In real cases the reactions do not exactly follow this pathway because the vibrational modes have at least their zero-point energies and can become more excited. For instance, in the case of the $OH^- + CH_3F \rightarrow CH_3OH + F^-$ reaction, 90% of the trajectories do not approach the deep minimum in the postsubstitution region according to a direct dynamical simulation.[33]

3.2.1 Fitting of the *ab initio* points

The PES function has to fulfill several requirements. It must be invariant under translation, rotation and the permutation of the identical atoms. The translational and rotational invariances are fulfilled if we use internal coordinates instead of Cartesian coordinates. The Morse-type variables describe well the dissociation of the bonds. The Morse-type variables are $y_{ij} = \exp(-r_{ij}/a)$,

where r_{ij} are the atom-atom coordinates, and a is a real fixed parameter. The PES function can be given in the following form:[34,35]

$$V = \sum_{\mathbf{n}=\mathbf{0}}^{\mathbf{N}} C_{\mathbf{n}} \mathrm{S}(y_{12}^{n12} y_{13}^{n13} y_{14}^{n14} \dots y_{23}^{n23} y_{24}^{n24} \dots) \,, \tag{42}$$

where S is a symmetrization operator, which symmetrizes the fitting basis under the permutation of identical atoms. The permutationally invariant fitting is one of the most important goals in connection with the PES development.[34,36,37,38,39] The $C_{\mathbf{n}}$ [$\mathbf{n}$=(n_{12},n_{13},n_{14},...,n_{23},n_{24},...)] denotes the coefficients which are determined by a weighted linear least-squares fit to the *ab initio* data. The number of the coefficients depends on the number of the atoms, the permutational symmetry, and the maximum order of the polynomials. The number of the points is usually a few tens of thousands. The maximum order of the polynomials is often five or six. The lower permutational symmetry and the higher order of the polynomials give more coefficients. The a parameter, which is usually 2-3 bohr, controls the asymptotic behaviour of the PES. Lower a value is chosen in the case of short-range dispersion interactions, and higher in the case of long-range ion-dipole interactions and H-bonds. The low-energy points should have a larger weight in the fit. Therefore, a weight of $E_0/(E + E_0)$ is used to suppress the higher-energy points, where E_0 is a weight parameter and E is the energy of the point relative to the global minimum. The goal in the case of the fitting is to reach the chemical accuracy (which means 1 kcal/mol or less RMS error) at least in the most important low-energy regions.

4 Quasiclassical trajectory (QCT) method

The exact method for the theoretical investigation of chemical reactions would be the quantum dynamics method which uses the solution of the time-dependent (or independent) Schrödinger equation. This is a rather time-comsuming procedure, for more than four-atom systems usually only reduced-dimensional models can be applied. The quasiclassical trajectory (QCT) method is an effective way to study the reaction dynamics which uses the laws of the classical physics during the trajectory propagation. There are several equivalent formulations of the classical physics. The Newton-formulas are a common description of it. Among the laws of Newton, the following one must be used in a QCT simulation:

$$\mathbf{F} = m\mathbf{a}, \tag{43}$$

where **F** means force and **a** means acceleration. Equation (43) can be rewritten as:

$$-\frac{\partial \mathrm{V(q)}}{\partial \mathrm{q}} = m\frac{\partial^2 \mathrm{q}}{\partial t^2}, \tag{44}$$

where the **q** means the spatial coordinates and the $V(\mathbf{q})$ is the potential energy.

Another formulation uses the Lagrange function ($L(\mathbf{q},\mathbf{p})$), which is the difference between the kinetic ($T(\mathbf{q},\mathbf{p})$) and the potential energy ($L(\mathbf{q},\mathbf{p}) = T(\mathbf{q},\mathbf{p}) - V(\mathbf{q})$). In this case the equation of motion is

$$\frac{\mathrm{d}}{\mathrm{d}t}\frac{\partial \mathrm{L(q,p)}}{\partial \dot{\mathrm{q}}} - \frac{\partial \mathrm{L(q,p)}}{\partial \mathrm{q}} = 0\,, \tag{45}$$

where $\dot{\mathrm{q}}$ means the first derivative of the coordinate with respect to the time, the velocity.

The third equivalent approach is the Hamilton formalism. The classical Hamilton function is the sum of the kinetic and the potential energy ($H(\mathbf{q},\mathbf{p}) = T(\mathbf{q},\mathbf{p}) + V(\mathbf{q})$) and the equations of motion are

$$\frac{dq}{dt} = \frac{\partial H(q,p)}{\partial p} \tag{46}$$

$$\frac{dp}{dt} = -\frac{\partial H(q,p)}{\partial p}\,. \tag{47}$$

The above equations must be solved by numerical integration methods. The most commonly used are the Verlet algorithms[40] which are time-reversible which means that the energy will be the same if we reach the same structure as the starting geometry. This guarantees the total energy conservation during the trajectory evolution. One type of the Verlet algorithms is the Verlet integration without velocities. The time evolution is the following Taylor-polynomial:

$$\vec{\mathrm{x}}(t+\Delta t)=\vec{\mathrm{x}}(t)+\vec{\mathrm{v}}(t)\Delta t+\frac{\vec{\mathrm{a}}(\mathrm{t})\Delta t^{2}}{2}+\frac{\vec{\mathrm{b}}(\mathrm{t})\Delta t^{3}}{6}+\mathcal{O}\Delta t^{4} \tag{48}$$

$$\vec{\mathrm{x}}(t-\Delta t)=\vec{\mathrm{x}}(t)-\vec{\mathrm{v}}(t)\Delta t+\frac{\vec{\mathrm{a}}(t)\Delta t^{2}}{2}-\frac{\vec{\mathrm{b}}(t)\Delta t^{3}}{6}+\mathcal{O}\Delta t^{4} \quad , \tag{49}$$

where $\vec{\mathrm{a}}(t)$ is the acceleration, $\vec{\mathrm{b}}(t)$ is the jerk or hyperacceleration, which is the first derivative of the acceleration with respect to the time, so the third derivative of the position with respect to the time and $\mathcal{O}$ is the Lagrange remainder. The velocity can obtained as:

$$\vec{\mathrm{v}}(t)=\frac{\vec{\mathrm{x}}(t+\Delta \mathrm{t})-\vec{\mathrm{x}}(t-\Delta t)}{2\Delta t}+\mathcal{O}\Delta t^{2} \tag{50}$$

In the case of our reaction dynamics simulations the velocity Verlet algorithm is used, which gives the velocity directly:

$$\vec{\mathrm{x}}(t+\Delta t)=\vec{\mathrm{x}}(t)+\vec{\mathrm{v}}(t)\Delta t+\frac{\vec{\mathrm{a}}(t)\Delta \mathrm{t}^{2}}{2} \tag{51}$$

$$\vec{\mathrm{v}}(t+\Delta t)=\vec{\mathrm{v}}(t)+\frac{\vec{\mathrm{a}}(t)+\vec{\mathrm{a}}(t+\Delta t)}{2}\Delta t \tag{52}$$

In the case of the QCT simulations, some of the quantum effects are taken into account. The internal energy of the reactant in the QCT simulation is identical to its vibrational or rovibrational quantum state energy. For the final conditions, there is a possibility to sort out the trajectories where the products do not have vibrational energy equal or more than its zero-point energy. If the product consists of two or more fragments, there will be two ways of the zero-point energy restriction, the soft and the hard. In the case of the soft restriction only those trajectories will not be taken into account where the sum of the vibrational energies of the product molecules does not reach the sum of their zero-point energies. The hard restriction means the comparison of the vibrational energies of the products with their zero-point energies. The strictest approach is if we compare the zero-point energies of the vibrational modes with the mode energies in the final state of the molecules. Gaussian binning methods give larger weights to the quantum-mechanically more reasonable products and will be discussed in detail later.

4.1 Initial conditions

4.1.1 Microcanonical normal mode sampling

The setting-up of the initial vibrational energy levels of the reactants can be either canonical or microcanonical. The canonical normal-mode sampling means the initialization of the vibrational energy levels based on the Boltzmann-distribution. The microcanonical normal-mode sampling,[41] which I used during my work, means the same set-up of the vibrational energy levels for every reactant molecules.

A nonlinear system which contains *N* atoms has 3*N*–6 vibrational modes. The *i*th mode has the frequency ω_i. The harmonic vibrational energy of a mode, in atomic units, can be expressed as:

$$E_{\mathrm{vib},i} = \omega_i(n_i + \tfrac{1}{2}) \,, \tag{53}$$

where n_i is the vibrational quantum number, which we choose to zero, the mode is in ground state. If it is zero in the case of all vibrational modes, we can get the zero-point energy of the molecule as the sum of the $E_{\mathrm{vib},i}$ energies.

If we have all of the $E_{\mathrm{vib},i}$ energies, we choose a random phase to every mode, transforming its E_i into a normal mode coordinate Q_i and momentum P_i.

$$Q_i = \frac{\sqrt{2E_i}}{\omega_i}\cos(2\Pi R_i) \tag{54}$$

$$P_i = \sqrt{2E_i}\sin(2\Pi R_i), \tag{55}$$

where R_i is a real random number between 0 and 1. The harmonic classical vibrational mode energy can be written as

$$E_i = \frac{{P_i}^2}{2} + \frac{\omega_i{}^2 {Q_i}^2}{2}. \tag{56}$$

Thus, the normal mode coordinate Q_i and momentum P_i are chosen as a random point on an ellipse, and the size of this ellipse is determined by the vibrational energy of the normal mode.

The last step of the procedure is to transform the Q_i and P_i vectors from normal-mode coordinates to Cartesian coordinates:

$$\mathbf{q} = \mathbf{q}_\mathrm{e} + \mathbf{M}^{-1/2}\mathbf{l}\mathbf{Q} \tag{57}$$

$$\mathbf{p} = \mathbf{M}^{1/2}\mathbf{l}\mathbf{P} \,, \tag{58}$$

where $\mathbf{q}_e$ is the equilibrial position, **M** is a diagonal mass matrix and the **l** is a transformation matrix, which will be discussed in chapter 4.3.

4.1.2 The orientation and velocities of the reactants

If the goal is to simulate the collision of two reactants, these particles must be at random orientation and in appropriate distance from each other. The random orientation is prepared by an Euler rotation matrix which rotates the reactants by three random angles around the initial position and rotates the initial velocity vector, too.

$$\mathbf{q} = \mathbf{R}(\theta, \varphi, \Psi)\mathbf{q}^0 \tag{59}$$

$$\mathbf{v} = \mathbf{R}(\theta, \varphi, \Psi)\mathbf{v}^0, \tag{60}$$

where the three Euler angles are defined by the following equations:

$$\cos\theta = 2R_1 - 1; \qquad \varphi = 2\pi R_2; \qquad \Psi = 2\pi R_3 \tag{61}$$

R_1, R_2, and R_3 are three different real random numbers between 0 and 1.

The distance of the reactants is defined by the separation of their center of mass positions and by their vertical distance called impact parameter and abbreviated by *b*.

In Figure 4.1, α indicates the initial attack angle in an example for S_N2 reactions. Attack angle distributions for reactive trajectories are sometimes analyzed in QCT studies.

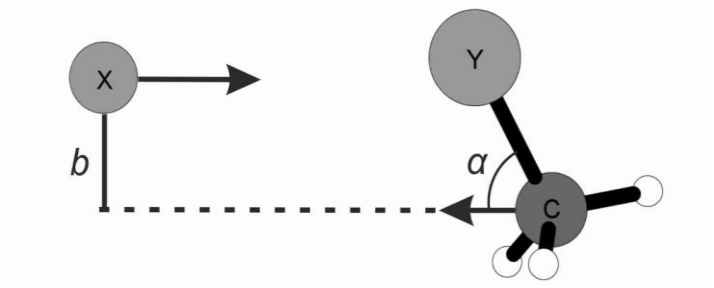

Figure 4.1.: Definition of the attack angle

The relative velocity is obtained by the following expression:

$$v_{\mathrm{rel}} = \sqrt{[2E_{\mathrm{coll}}(m_{\mathrm{X}} + m_{\mathrm{Y}})/(m_{\mathrm{X}}m_{\mathrm{Y}})]}, \tag{62}$$

where E_{coll} is the collision energy and m_X and m_Y are the masses of the reactants X and Y, respectively. Then, the velocity vectors of X and Y can be obtained as:

$$\left(\frac{m_Y}{m_X+m_Y}v_{rel}, 0,0\right) \tag{63}$$

$$\left(\frac{-m_X}{m_X+m_Y}v_{rel}, 0,0\right), \tag{64}$$

respectively.

4.2 Final conditions

4.2.1 Reaction probabilities

For the final parameters, the reaction probability quantities are of outstanding importance. The reaction probability can be obtained by the following expression:

$$P(E_{coll}, b) = \frac{N_r}{N_{total}} , \tag{65}$$

where N_r is the number of the reactive trajectories and N_{total} is the total number of trajectories at a given collision energy and impact parameter. This quantity can not be measured directly because the impact parameter is not tunable during experiments.

Integral cross sections (ICSs) can be obtained by weighting $P(E_{coll}, b)$ by the impact parameter and integrating from 0 to b_{max}, for example, with the trapezoidal rule:

$$\sigma(E_{coll}) = \int_0^{b_{max}} 2\pi b P(E_{coll}, b) \mathrm{d}b \tag{66}$$

Cross sections are measurable in contrast to $P(E_{coll},b)$ and give good congruence with experiments considering the fact that the collisions with larger impact parameters have higher probabilities.

4.2.2 Initial attack angle

In Figure 4.1, the definition of the initial attack angle is shown. If this was adjusted to a concrete value, this parameter would belong to the initial conditions, but due to the random orientation of the reactants, the attack angle distributions of the reactive trajectories can be related to the final parameters. The attack angle is an indicator to the reaction mechanism. However, the initial attack angle is not capable for classification of the trajectories to the specific reaction mechanisms, because even if the attacking agent comes from the front, it will be able to reach the lateral or backside region and vice versa. But after the classification, the attacking angle can be

interesting, for instance the significant amount of front-side minimum formation in the case of backside attack shows the prominent role of this complex.

4.2.3 Scattering angle

The scattering angle is also an important quantity, which is defined in Figure 4.2. The scattering angle can refer to the reaction mechanism. Nearly isotropic scattering angle distributions belong to the indirect mechanisms. For the S_N2 substitution reactions, backward scattering, which means that the θ angle is close to 180°, belongs to the rebound mechanism, whereas the direct stripping and frontside attack mechanisms show sideways (θ is close to 90°) and forward (θ is close to 0°) scattering.

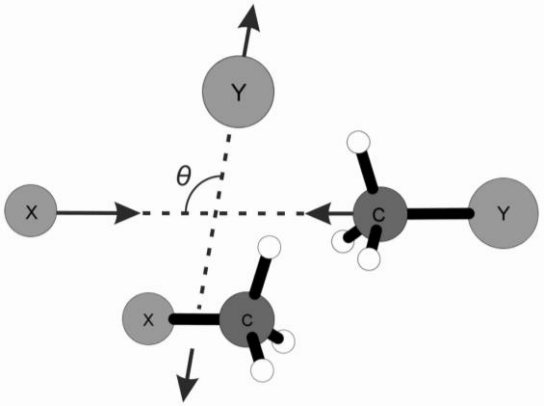

Figure 4.2. The definition of the scattering angle. The X indicates the attacking particle and Y indicates the leaving group.

4.2.4 Relative translational energy and internal energy

The relative translational energy is the following expression:

$$E_{\text{trans}} = \frac{\mu v_{\text{rel}}^2}{2}, \tag{67}$$

where the μ is the reduced mass, which is the product of the masses of the fragments divided by the sum of their masses. The v_{rel} is the relative velocity which is the difference vector between the product velocity vectors.

The internal energy is the sum of the vibrational and the rotational energy of a molecule. The vibrational energy of the polyatomic products is the sum of the kinetic and the potential energy of the vibration. The kinetic energy can be calculated as:

$$E_{\mathrm{kin}} = \frac{1}{2}\sum_{i=1}^{natom} m_i(\mathbf{v}_i - \mathbf{v}_{\mathrm{com}})^2 \,, \tag{68}$$

where the $\mathbf{v}_{\mathrm{com}}$ is the velocity of the center of mass, the $\mathbf{v}_i$ vectors are the atomic velocities and the m_i values are the atomic masses. The potential energy of the vibration is the relative potential energy of the molecule to the potential energy of the molecule in equilibrium.

The relative translational energy and the internal energy are also indicators of the reaction mechanism because in the case of indirect mechanisms there is enough time for the relative translational energy to be converted to the internal energy modes. In consequence, the internal energy diagram of the products will show a shift to the larger energy values if indirect mechanisms dominate.

4.2.5 Trajectory integration time

The chemical reactions have femtosecond-picosecond time scale. In the field of the theoretical investigation of chemical reactions, we can speak about either step numbers or reaction times. This quantity can distinguish between direct and indirect reactions, because the direct reactions significantly take shorter time. However, the reaction mechanism cannot be unambiguously distinguished based on the trajectory integration time, because even if a reaction with a specific mechanism is usually long, it can be sometimes shorter and also the short, direct reaction routes can take sometimes longer. A typical value for the integration time step in our QCT simulations is 0.0726 fs, which corresponds to 3 atomic time units.

4.3 Mode-specific (ro)vibrational analysis

In the beginning of this chapter, it is necessary to introduce the inertia tensor and the angular momentum of molecules.

The inertia tensor (**I**) can be obtained as:

$$I_{11} = \sum_{i=1}^{natom} m_i\left(y_i^2 + z_i^2\right) \tag{69}$$

$$I_{22} = \sum_{i=1}^{natom} m_i(x_i^2 + z_i^2) \tag{70}$$

$$I_{33} = \sum_{i=1}^{natom} m_i (x_i^2 + y_i^2) \tag{71}$$

$$I_{23} = I_{32} = -\sum_{i=1}^{natom} m_i y_i z_i \tag{72}$$

$$I_{21} = I_{12} = -\sum_{i=1}^{natom} m_i x_i y_i \tag{73}$$

$$I_{31} = I_{13} = -\sum_{i=1}^{natom} m_i x_i z_i \,, \tag{74}$$

where the x_i, y_i, and z_i are the Cartesian coordinates of the atoms in the center of mass frame. The angular momentum of a molecule can be obtained as:

$$\mathbf{L} = \mathbf{I}'\boldsymbol{\omega} = \mathbf{r} \times \mathbf{p} \,, \tag{75}$$

where $\times$ refers to vectorial product and **I**′ is derived from the **I** by an orthogonal transformation. The **I** is the inertia tensor in the body-centered Cartesian space and the **I**′ is the inertia tensor in the space centered Cartesian space. The $\boldsymbol{\omega}$ is the angular speed of the rotating molecule and **p** is the momentum in the center of mass frame.

In the QCT analysis, we set up the initial (ro)vibrational energy levels quantum-mechanically, but due to the classical nature of the trajectory propagation, the final levels do not satisfy the rules of quantum mechanics. The Gaussian Binning[42] techniques sort the trajectories assigning a weight to each reactive trajectory favoring the cases with products which have quantum-mechanically better vibrational energy levels. One way of this is to obtain classical actions which are comparable to the quantum numbers. This can be employed in the case of diatomic systems, but in the case of polyatomic systems this method is impractical due to the exponential time scaling of the procedure. In these cases, the so-called 1GB method[43,44] can be employed, which compares the total vibrational energies of the products with the quantum-mechanically proper energies.

The product analysis procedure starts with relating the actual geometry to a reference minimum geometry, which can be found for example with an optimization procedure which locates it to the closest minimum. After that, the optimal orientation of the actual geometry must be found with respect to the reference geometry, which can be done by minimizing this expression:

$$\sum_{i=1}^{N} \left\| \mathbf{C}(\theta, \varphi, \Psi)\mathbf{r}_i - \mathbf{r}_i^{\mathrm{eq}} \right\|^2 \,, \tag{76}$$

or satisfying the following equation:

$$\sum_{i=1}^{N} m_i \mathbf{r}_i^{\mathrm{eq}} \times \left(\mathbf{C}(\theta, \varphi, \Psi)\mathbf{r}_i - \mathbf{r}_i^{\mathrm{eq}} \right) = \mathbf{0} \,, \tag{77}$$

where **C** is the transformation matrix with respect to the three Euler-angles, $\mathbf{r}_i$ values are Cartesian coordinates of the actual geometry and $\mathbf{r}_i^{\mathrm{eq}}$ values are Cartesian coordinates of the reference geometry.

At the beginning of the process finding the **C** matrix, a normal-mode analysis is performed at the reference geometry, which gives beside the frequencies the **l** matrix. This orthogonal transformation matrix can transform between the mass-scaled Cartesian coordinates and the normal coordinates. This normal-mode analysis is done once then the same reference geometry and the same **l** matrix is used for the other geometries. After that, we remove the angular momentum by modifying velocities:

$$\mathbf{v}_i^{\mathrm{nr}} = \mathbf{v}_i - \boldsymbol{\Omega} \times \mathbf{r}_i \,, \tag{78}$$

where $\boldsymbol{\Omega} = \mathbf{I}^{-1}\mathbf{j}$,and $\mathbf{I}^{-1}$ is the inverse of the moment of inertia tensor at $\mathbf{r}_i$ and $\mathbf{j} = \sum_{i=1}^{N} \mathbf{r}_i \times (m_i \dot{\mathbf{r}}_i)$.

Then, the **C** matrix can be obtained as:

$$A_{n,m} = \sum_{i=1}^{N} m_i r_{i,n} \, r_{i,m}^{\mathrm{eq}} \qquad n, m = 1(x), 2(y), 3(z) \tag{79}$$

$$\mathbf{A}_1 = \mathbf{A}^{\mathrm{T}}\mathbf{A} \;;\; \mathbf{A}_2 = \mathbf{A}\mathbf{A}^{\mathrm{T}} \tag{80}$$

$$\mathbf{C} = \mathbf{U}_1 \mathbf{U}_2^{\mathrm{T}}, \tag{81}$$

where the columns of $\mathbf{U}_1$ and $\mathbf{U}_2$ contain the normalized eigenvectors of the real symmetric matrices $\mathbf{A}_1$ and $\mathbf{A}_2$, respectively. Then, the Cartesian coordinates and velocities which satisfy the Eckart conditions will be $\mathbf{C}\mathbf{r}_i$ and $\mathbf{C}\mathbf{v}_i^{\mathrm{nr}}$, respectively. Since the sign of an eigenvector is not well-defined, eight different **C** matrices exist, which all satisfy the Eckart conditions.

$$\mathbf{C}^a = \mathbf{U}_1^a \mathbf{U}_2^{\mathrm{T}} \tag{82}$$

$$(\mathbf{U}_1^a)_{n,m} = (-1)^{a_m} (\mathrm{U}_1)_{n,m} \qquad \mathbf{a} = (a_1, a_2, a_3) \qquad a_1 = 1{,}2 \quad a_2 = 1{,}2 \quad a_3 = 1{,}2 \tag{83}$$

Hereafter, the **C** matrix indicates the matrix which gives the smallest (76) expression. The normal coordinates and the momenta in the normal coordinate space can be obtained as:

$$Q_k = \sum_{i=1}^{N} \sqrt{m_i}\, \mathbf{l}_{ki} \Delta \mathbf{r}_i \qquad k = 1{,}2, \ldots, 3N-6 \tag{84}$$

$$P_k = \sum_{i=1}^{N} \sqrt{m_i}\, \mathbf{l}_{ki} \mathbf{C}\mathbf{v}_i^{\mathrm{nr}} \qquad k = 1{,}2, \ldots, 3N-6 \tag{85}$$

where $\Delta \mathbf{r}_i = \mathbf{C}\mathbf{r}_i - \mathbf{r}_i^{\mathrm{eq}}$. The harmonic vibrational energy can be calculated using the equation (53).

Then, the noninteger classical harmonic action can be obtained for each mode as:

$$n'_k = \frac{E_k}{\omega_k} - \frac{1}{2}. \tag{86}$$

4.4 Determining configuration of the products

The Eckart transformation procedure has other practical applications beside the normal-mode analysis. In order to determine the configuration of a molecule one need a reference geometry with known configuration and with the Eckart transformation finding the best overlap with it. Then, the determinant of the transformation matrix gives information about the configuration. If the determinant equals to 1, the configuration will be the same as the configuration of the reference geometry. If the determinant equals to -1, the configuration of our molecule will be inverted with respect to the configuration of the reference geometry. In the case of nonreactive trajectories the configuration of the molecules is also important because induced inversion can occur, which means that the final configuration of the reactant molecule is inverted relative to the initial configuration.

5 Results and discussion

5.1 Developing of a high-level *ab initio* potential energy surface for the $F^- + CH_3I$ system

After I had written a code which can analyse the results of the QCT simulations, I searched for stationary points in connection with the substitution and abstraction reaction pathways of the fluoride-methyliodide system. Figure 5.1 shows the energy diagram based on these stationary points. Actually, I found further stationary points which are the transition states of the dihalide (IF^-) production and the hydride substitution (the process where F^-substitutes a H^- ion). These reaction routes are of less importance, so although we found some dihalide production at high energies, we do not discuss this in this thesis.

First, I found the stationary points at MP2 level with aug-cc-pVDZ basis function. I optimized further the geometries at CCSD(T)-F12b/aug-cc-pVDZ(-PP), then at CCSD(T)-F12b/aug-cc-pVTZ(-PP) level. For the iodine atom, we used an effective core potential (ECP) instead of the 28 inner-core electrons, because in the case of heavy atoms the scalar relativistic effects are not neglectable due to the high speed of the electrons on the nearest orbitals to the nucleus. PP denotes the basis belonging to the ECP. I performed single-point (SP) calculations on the geometries optimized at CCSD(T)-F12b/aug-cc-pVTZ(-PP) level. The SP levels were FC-CCSD(T)-F12b-aug-cc-pVQZ(-PP), FC-CCSD(T)-aug-cc-pwCVDZ(-PP), AE-CCSD(T)-aug-cc-pwCVDZ(-PP), FC-CCSD(T)-aug-cc-pwCVTZ(-PP) and AE-CCSD(T)-aug-cc-pwCVTZ(-PP). FC means frozen core and AE means all electron. In the case of frozen-core calculations only the valence shell electrons are correlated, in the case of all electron calculations the correlated motion of the electrons on one inner shell is also taken into account. The “pw” basis sets are optimized to the AE computations. With the difference of the AE-CCSD(T)-aug-cc-pwCVTZ(-PP) and FC-CCSD(T)-aug-cc-pwCVTZ(-PP) energies core correction energy can be calculated. The most accurate energies which are marked as red in Figure 5.1, are obtained from the FC-CCSD(T)-aug-cc-pVQZ(-PP) energies with the addition of the core correction and the ZPE correction at FC-CCSD(T)/aug-cc-pVTZ(-PP) level. All three energies are relative to the corresponding energies of the reactants. The black energies in Figure 5.1 belong to the geometries optimized on the final potential energy surface with Newton-Raphson method. Figure 5.2 shows some of stationary points including CH_3I and CH_3F with the most important geometric parameters obtained at FC-CCSD(T)-F12b/aug-cc-pVDZ(-PP) and FC-CCSD(T)-F12b/aug-cc-pVTZ(-PP) levels and from the geometries optimized on the analytical PES.

As Figure 5.1 shows the $F^- + CH_3I$ S_N2 reaction is highly exotherm. The Walden-inversion substitution process can proceed via several submerged stationary points. The retention pathways

have positive classical barriers of 9.1 and 20.1 kcal/mol for double inversion and front-side attack, respectively. Thus, as seen, the novel double-inversion mechanism is the lowest energy retention pathway of the $F^- + CH_3I$ S_N2 reaction. The proton transfer between F^- and CH_3I is an endothermic process via several minima and transition states. It is important to notice that the double-inversion barrier height is below the energy level of the proton-transfer products; thus, double inversion may open at collision energies, where the HF + CH_2I^- products are energetically not available.

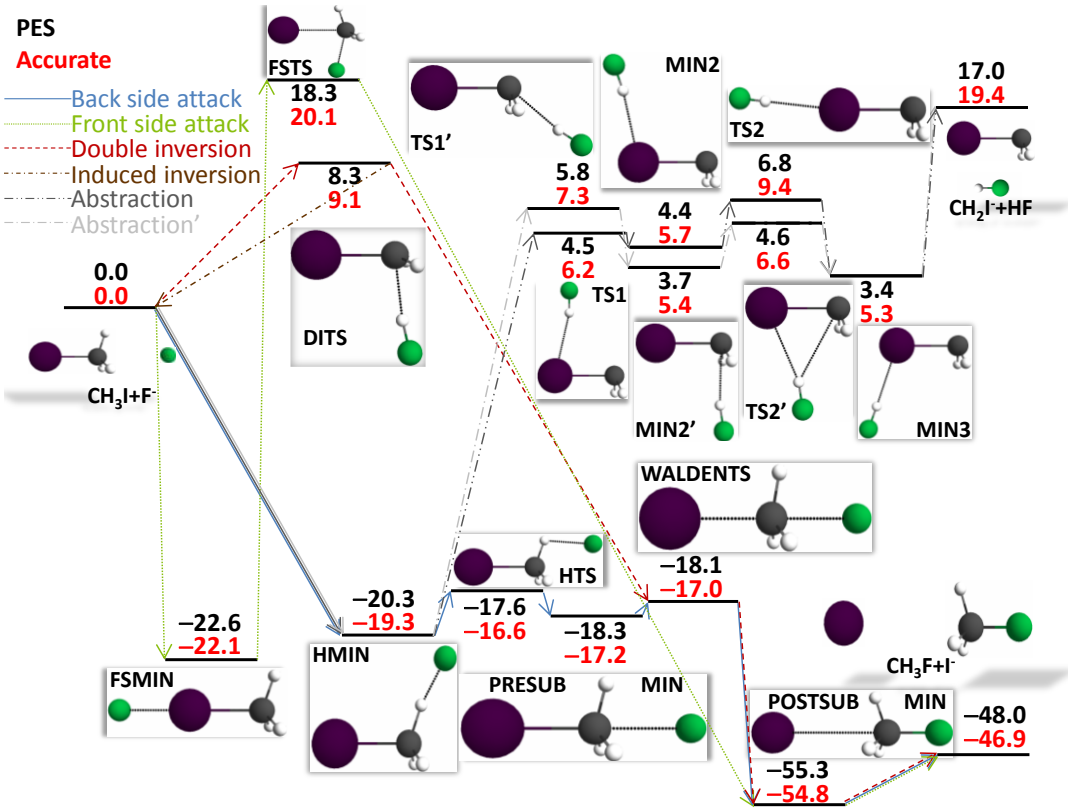

Figure 5.1.: Reaction energy diagram for the $F^- + CH_3I$ system showing the different S_N2 and abstraction pathways and the relative energies (kcal/mol) of the stationary points

As were mentioned in chapter 3.2, the first potential energy surface is generated by the several modifications of the geometric parameters of the stationary points. I used for this purpose several techniques:

a) *n*-mode grids to generate geometries from the stationary points (*n* can be 1,2,3 or 4).

b) Random changes in the stationary point geometries.

c) For describing the reactant and the product region I put the fragments several different distances from each other. If this distance reached a value (this was usually 10 Å) the energies of the fragments could be added, because the interactions of these particles can be neglected.

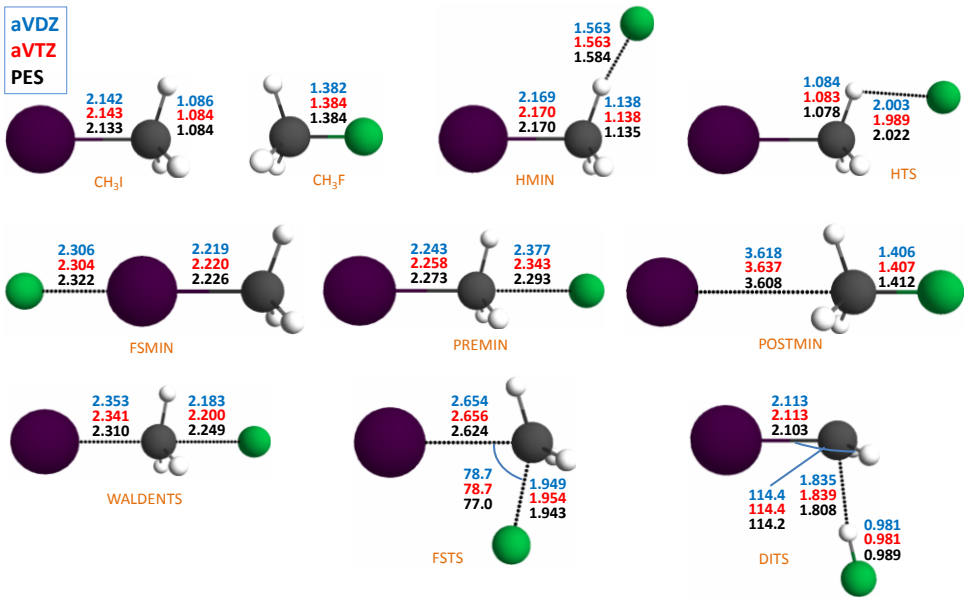

Figure 5.2.: Structural parameters (in Å) of selected stationary points for the F^- + CH_3I system obtained at CCSD(T)-F12b with the indicated basis sets and on the PES

After I completed the first surface, I ran trajectories on that. In this and the following steps I chose the trajectories which were unphysical on the used energy, and I selected points from them for Molpro calculations. Thus, I put these points to the next fitting and so to the next surface.

In the last step of the PES development, I checked the several reaction pathways. I chose some trajectories belonging to each reaction route, and I calculated the energy of the points by Molpro. If the Molpro energy of a point was too far away from its PES energy, then the geometry would be taken into the next PES. I mention here that this process can now be done automatically by a code being developed in our group. This code runs trajectories, and if a geometry in the trajectory differs significantly in geometry and/or in energy from the geometries can be found in the PES, then the geometry will be taken into the next surface.

The development of the surface was not without any difficulties. The region of the dihalide production, where the system consists of a methyl radical (CH_3) and an IF^- ion, could not always be calculated by methods which use single-determinant wave functions. I observed that the energy of one PES point was below of the real energy minimum of the system (due to the wrong energy calculation). Thus, the other points had small weights in the fitting, so the RMS error was particularly high. I had to select out this and the other problematic points from the PES. In consequence, the potential energy surface for the F^- + CH_3I reaction may not be very accurate at high energies, since these problematic points are of high energies. The Molpro calculations showed in these cases high T_1 diagnostic values. The optimal T_1 diagnostic values are below 0.2, but between 0.2 and 0.4 the calculated energies may be acceptable. The energies of the higher-T_1 geometries could only be

computed accurately by multireference methods, for example, the multireference-configuration interaction method (MRCI),[45] which uses excited determinants which are generated from multi-configuration reference functions. However, the energies of the PES points have to be calculated by the same method, because the energy values of two different methods are not comparable. The MRCI method is, however, rather time-consuming, thus the calculation of each PES points would be very complicated using that. There is an other possibility to calculate the energies of these points, using the Orbital-optimised Quasi-Variational Coupled Cluster (OQVCCD) method which commonly used with perturbative correction (OQVCCD(T)) similarly to the simple Coupled Cluster methods. OQVCCD(T) method demands similar computational times as the CCSD(T) and is capable to treat those systems where the CCSD(T) fails, for instance, breaking triple bonds.[46] In an article[47] entitled "Effects of the Level of Electronic Structure Theory on the Dynamics of the F^- + CH_3I Reaction" we recalculated the points of this PES with several methods. We used the OQVCCD(T) method among the others, but these problematic structures were not included in the PES points, thus the advantages of the Quasi-Variational Coupled Cluster method could not be utilized.

The final surface I developed for the F^- + CH_3I system consists of 50 496 *ab initio* points. The final level used for the energy calculation was FC-CCSD(T)-F12b/aug-cc-pVTZ(-PP) with a CCSD(T)/aug-cc-pwCVDZ(-PP) core-correction.[48] The PES function was a 5th order polynomial expansion of Morse-type variables and the *a* parameter was chosen to 3 bohr due to the long-range ion-dipole interactions.

Comparison between the potential energy curves describing the motion of the fluoride along the C_3 axis obtained by the PES function and direct *ab initio* calculations at the same level as used for the PES points can show whether the PES describes well the long-range interactions. Figure 5.3 shows good agreement between the curves even in the case of large F-C distances, so it can be stated that the PES describes rather well the long-range ion-dipole interactions.

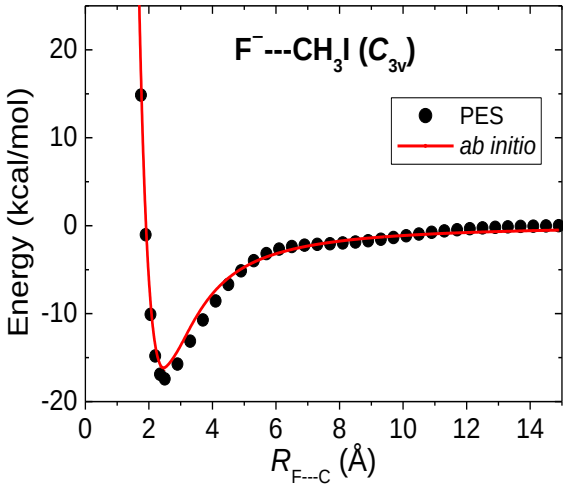

Figure 5.3.: Potential energy curves describing the moving away of the fluoride ion along the C_3 axis of the CH_3I molecule

The RMS values of the fitting were the following:

a) Lowest 20% of the energy interval (9122 points): 0.83 kcal/mol
b) Middle region (26328 points): 1.69 kcal/mol
c) Upper 60% of the energia interval (12114 points): 3.95 kcal/mol

Thus, I could reach the chemical accuracy in the most important low-energy region which is a requirement of a good potential energy surface. It has to be said that the low RMS value does not always mean good PES, because if there are lots of points in one region relatively to the other region, the many-point region can improve the RMS but does not improve the PES.

5.1.1 MOLPRO computational details

For all of my geometry optimization, frequency and single point energy calculations, I used the Molpro program package.[49] The optimization starts with the definition of a Z-matrix, which decribes a starting geometry. If this geometry is not similar enough to the stationary-point structure, the optimization may not be successful. The optimization can be a search for a minimum with {optg} command or a search for a saddle-point with {optg,root=2} command. I used for a couple of times stricter criteria for finding a minima or a saddle point than the default one. For this purpose, I always used the *gradient=1.d-5* option. Sometimes I used the *method,qsd* command for finding a difficult-to-find transition state. If I used all of these commands, this line was {optg,root=2 gradient=1.d-5;method,qsd}. If the *optg* command misses from the input, the Molpro will calculate only the energy of the geometry defined in the input. This is the so called single-point energy calculation. The command for frequency calculation can be written at the end of the input file.

5.2 Dynamics of the F^- + CH_3I S_N2 and proton-transfer reactions

Firstly, I ran trajectories on the newly developed potential energy surface at 7 different collision energies with reactants which have only their zero-point vibrational energies. The collision energies were 350, 1400, 2580, 3500, 5565, 12340, and 17500 cm^{-1}, corresponding to 1.0, 4.0, 7.4, 10.0, 15.9, 35.3, and 50.0 kcal/mol, respectively. 5000 trajectories were run at every impact parameter. The step of the impact parameters was 0.5 bohr and the maximum value of the *b* depended on the collision energy, because in the case of higher collision energies there is no chance of a reactive orientation to occur at large impact parameters. The b_{max} values were 30.0, 19.5, 17, 15, 13, 10.5, and 9 bohr, respectively at the collision energies given above. Figure 5.4 shows the decreasing of the reaction probabilities as a function of the impact parameter (the so-called opacity function). The above-mentioned b_{max} values can also be read approximately from Figure 5.4. Figure 5.5 shows that in the case of the direct stripping mechanism the reaction probabilities increase for low values of impact parameters. This is because in the case of the stripping S_N2 reaction the fluoride attacks the side of the methyl-iodide.

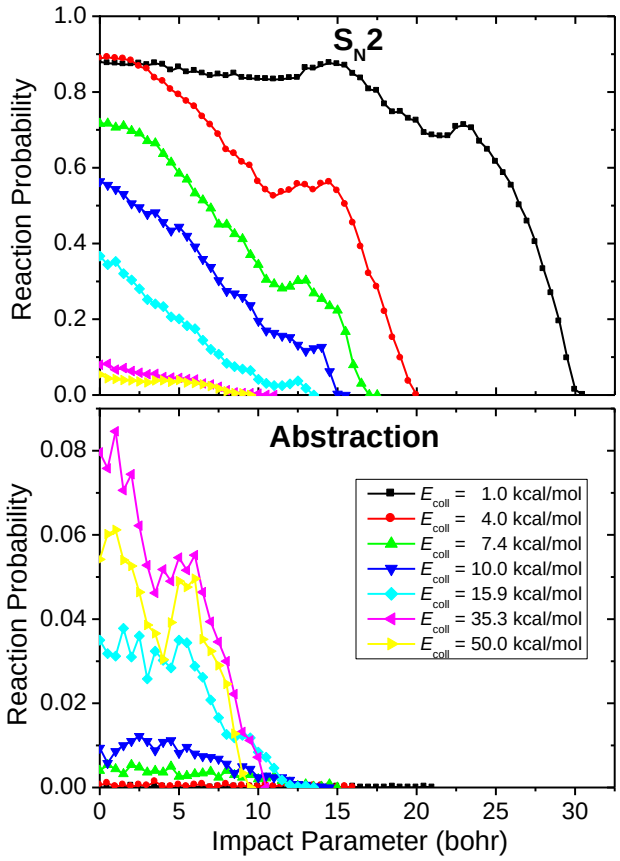

Figure 5.4.: Reaction probabilities of F^-+CH_3I depending on the impact parameter (opacity functions)

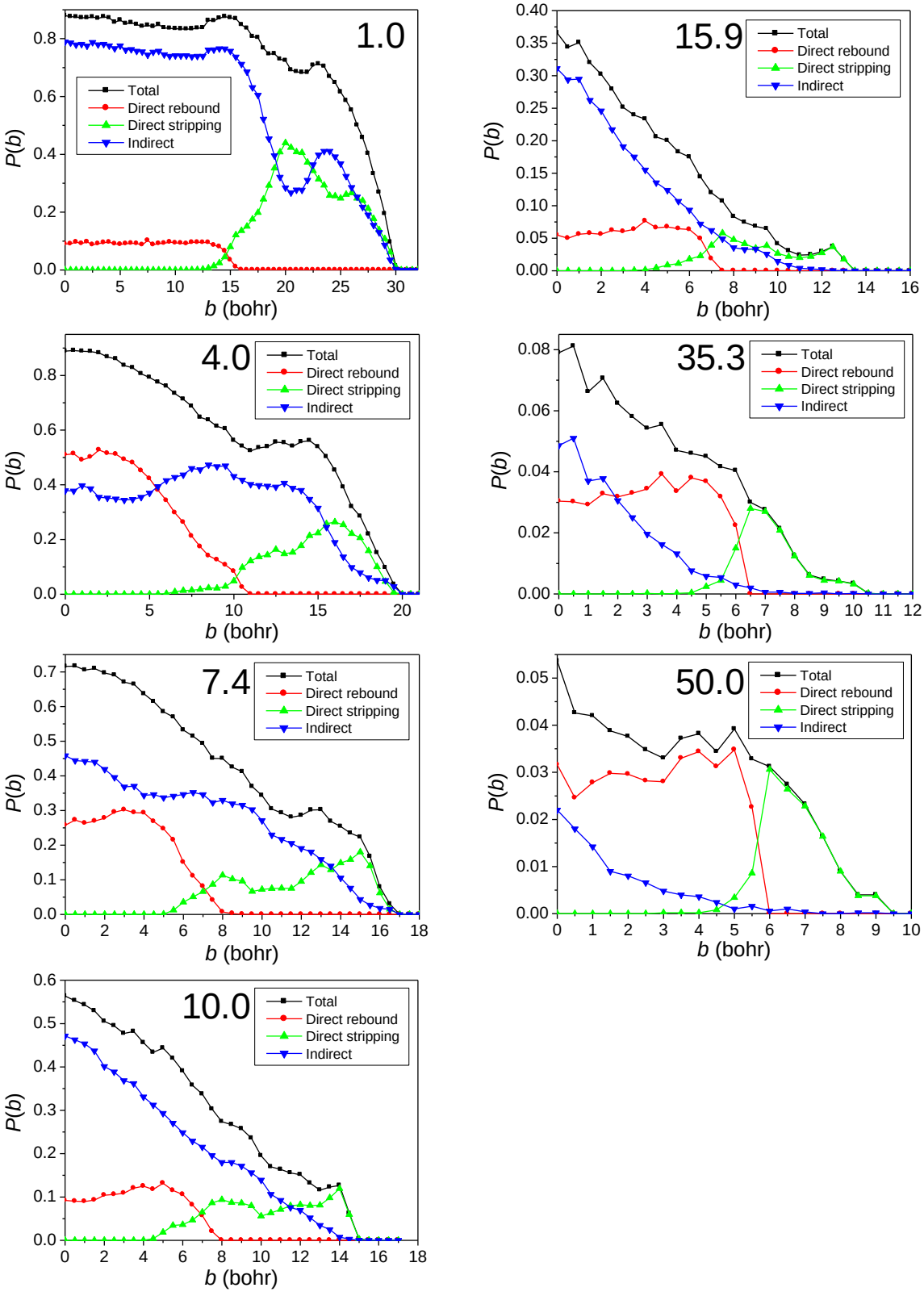

Figure 5.5.: Mechanism-specific opacity functions for the F^- + CH_3I S_N2 reaction

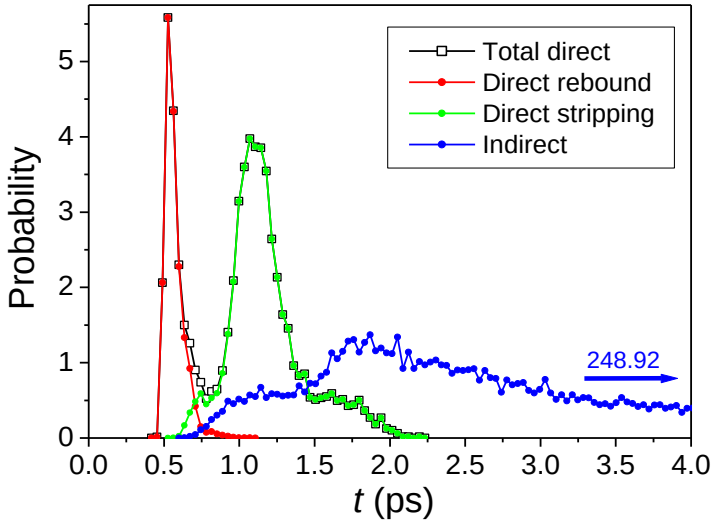

Figure 5.6.: Reaction time distributions of the different reaction pathways

I have analysed the final positions and velocities of the atoms with my analyzing code. In the case of the S_N2 reactive trajectories the configuration determination of the product and in the case of the nonreactive trajectories the configuration determination of the reactant was necessary. The induced-inversion process could produce reactants which are inverted with respect to the initial configuration. This process starts with a proton abstraction by the fluoride, and then continues with structures which are similar to the double-inversion transition state. After the turnover of the two hydrogens in the CH_2I^- unit, the fluorine donates the proton back. However, the second inversion does not take place in this case in contrast to the double-inversion process. In consequence, the trajectory will result in an inverted CH_3I and a fluoride ion. The determination of the configuration of the S_N2 products can distuingish between the inversion and the retention processes. Both the inversion and the retention processes can be direct and indirect. The direct and indirect processes can not be simply distuinguished based on simply the trajectory integration time as Figure 5.6 shows. Instead, the direct and indirect processes can be distuingished based on the following empirical function proposed by us:

$$Q(v,b) = R(b) + S(v) = r_0 + r_1 b + r_2 b^2 + r_3 b^3 + r_4 b^4 + s_0 + s_1 \mathrm{e}^{-\frac{v}{s_2}}, \qquad (87)$$

where b is the impact parameter, r and s values are parameters depending only on the collision energy, v is the leaving group velocity. Red curves in Figure 5.7 illustrate these $Q(v,b)$ functions, while the black curve on the last panel represents the $R(b)$ function.

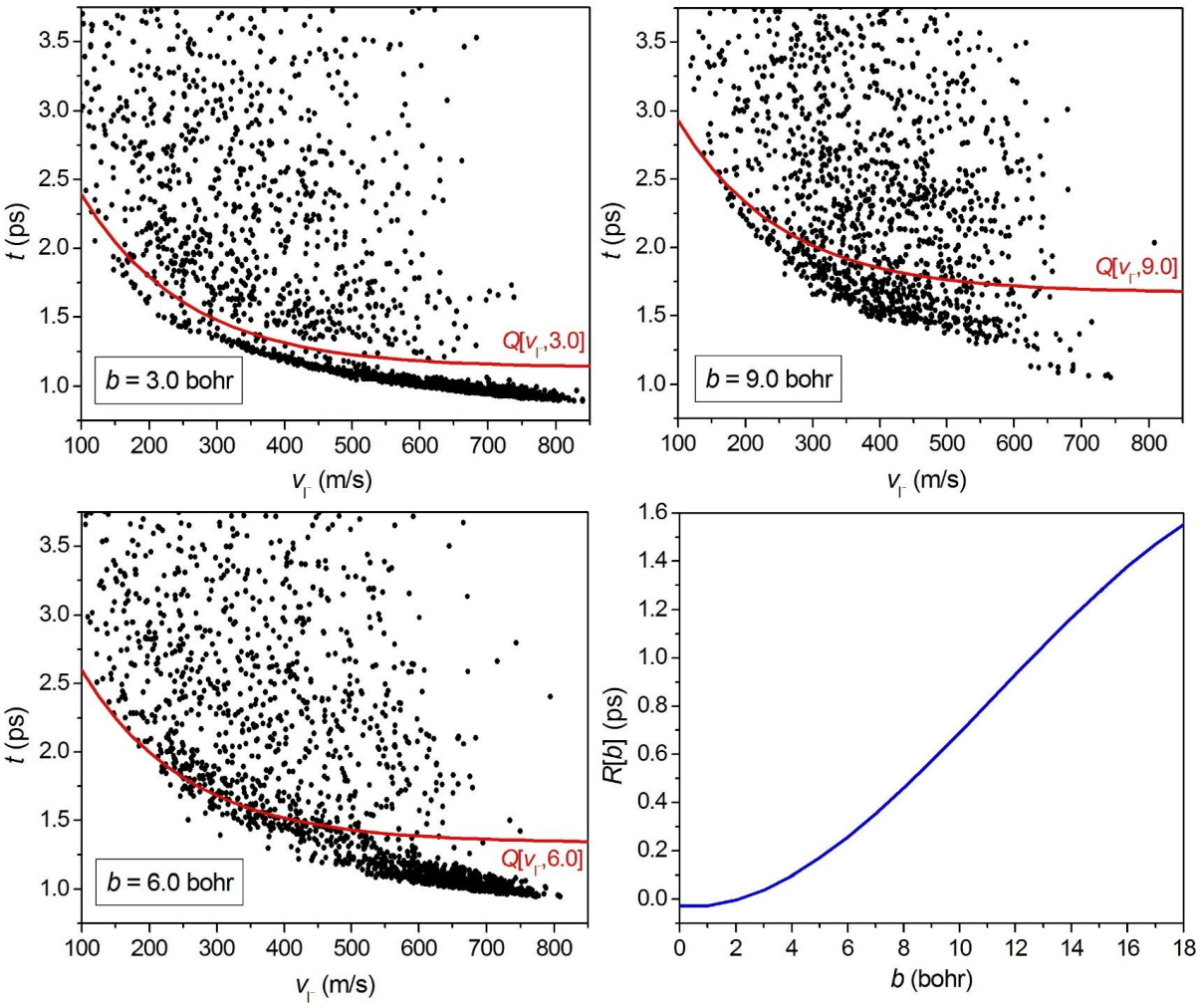

Figure 5.7.: Difference-making between direct and indirect reactions depending on the reaction time and product velocity

Figure 5.8 shows the ICSs depending on the collision energy and separated for the reaction channels.[48] Due to the high endothermicity of the abstraction reaction, the abstraction ICS values are higher at higher collision energies. In contrast, the high energies do not favour the exothermic S_N2 routes, which do not usually have positive activation energies. However, the double inversion and the front-side attack mechanism have significant positive activation energies. As a result, the highest ICS values belong to these processes at the higher energies. (The double inversion is an indirect reaction route, so the highest collision energies do not favour it.) The case is similar for the thermoneutral induced inversion channel which has the same activation energy as the double inversion channel.

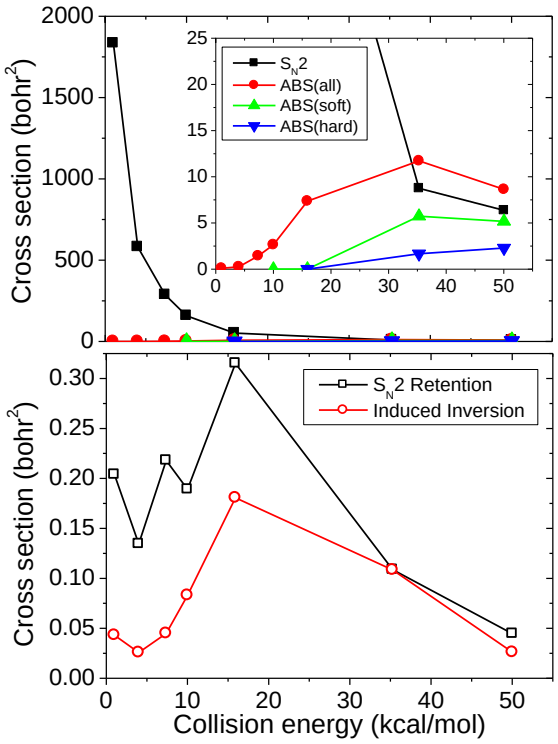

Figure 5.8.: ICS values as a function of the collision energy

As we mentioned in section 4.2, in the case of the dominance of indirect mechanisms the scattering angle shows a nearly isotropic distribution and the internal energy distributions shift to the higher values. At high energies, where the direct mechanisms are dominant (as can be seen in Figure 5.9), the internal energy shows a nearly isotropic distribution, and the scattering angle distribution shifts towards the backward scattering due to the direct rebound Walden substitution which is the most prevalent way of the S_N2 substitution, as Figure 5.10 shows.

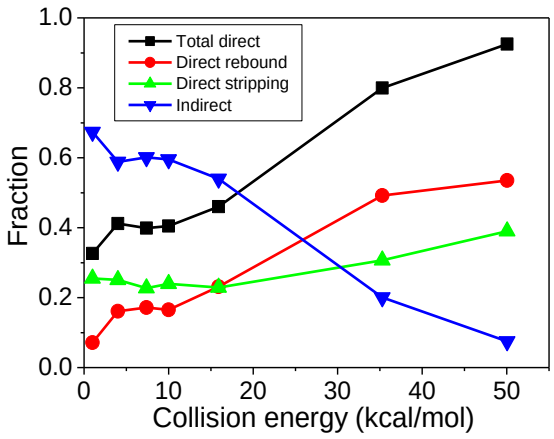

Figure 5.9.: Fraction of different S_N2 reaction mechanisms depending on the collision energy

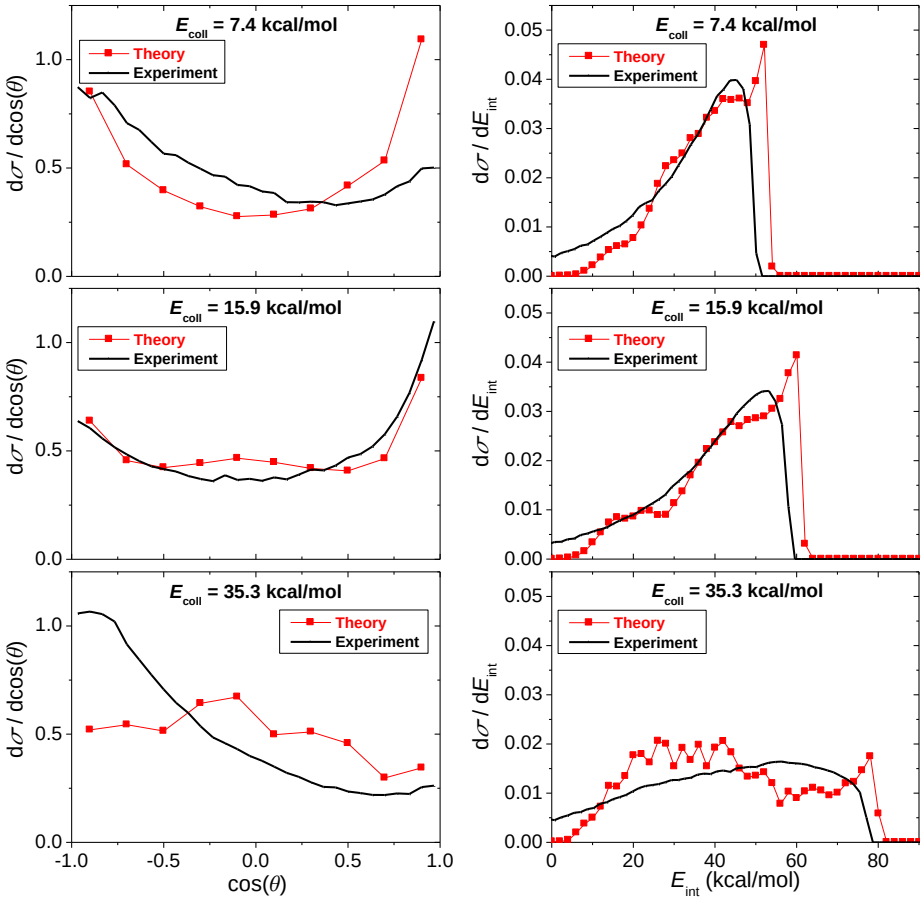

Figure 5.10.: Normalized scattering angle distributions and internal energy distributions for the S_N2 channel at different collision energies

5.3 Deciphering front-side complex formation in S_N2 reactions via dynamics mapping

The iodine atom has the electronegativity of 2.66 which is not far away from the electronegativity of the carbon atom of 2.55. In contrast, the electronegativity of the chlorine is 3.16 which is significantly higher than the electronegativity of the carbon. As a result, the fluoride makes much more stable front-side complex with the methyl-iodide than with the methyl-chloride, as can be seen in Figure 5.11.[50] Beside the about 20 kcal/mol lower energy in the case of the $F^-\cdots ICH_3$ complex, the shorter $F^-\cdots Y$ distances (where Y is the Cl or the I atom) also refer to the more stable complex in that case.

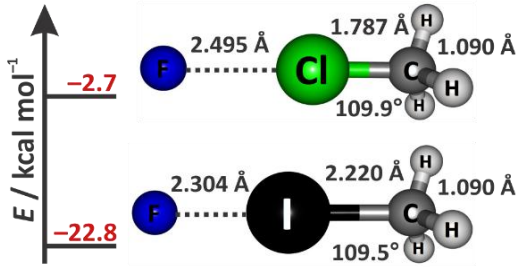

Figure 5.11.: Energies, relative to the reactant asymptotes, and structures of the $F^-\cdots ClCH_3$ and $F^-\cdots ICH_3$ complexes obtained at the CCSD(T)-F12b/aug-cc-pVTZ(-PP) level of theory

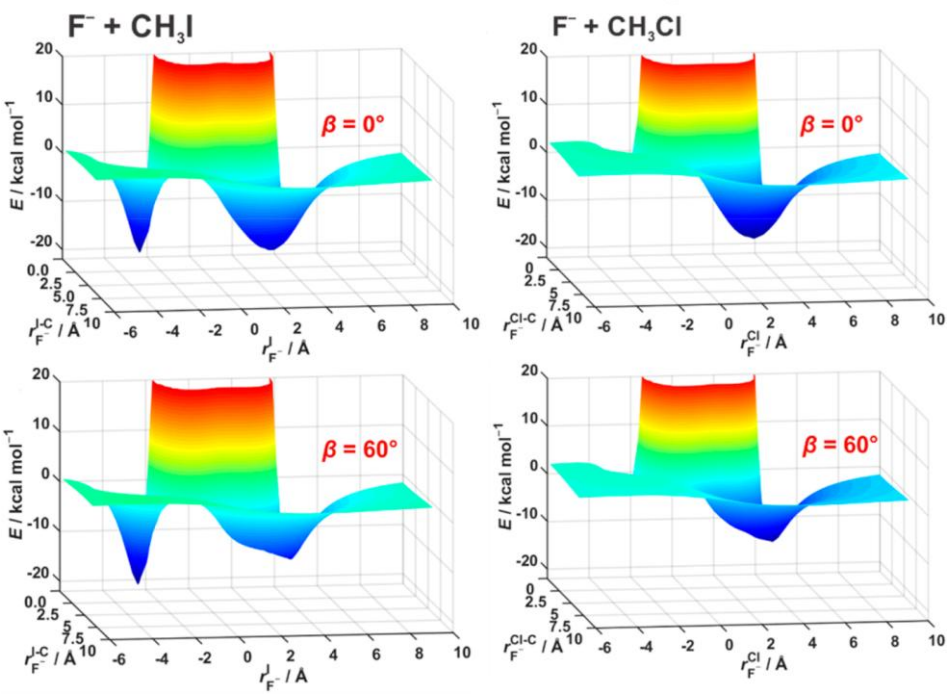

Figure 5.12.: Enegies of complexes depending on the halogen-halogen distances and the β angles defined in Fig. 5.13

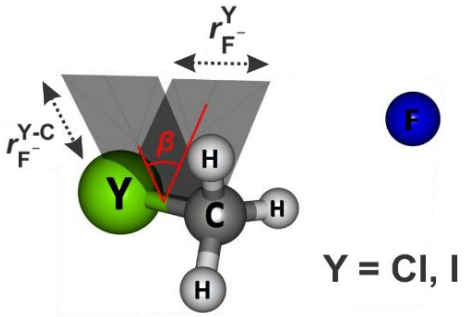

Figure 5.13.: Definition of the β angle

Figures 5.12 and 5.13 also show that in the case of F^- + CH_3I stable front-side complex exists in contrast to the case of the F^- + CH_3Cl system, because the negative $r^{I}_{F^-}$-values means that the position of the F^- is on the opposite direction from the Y atom as the carbon atom. As was mentioned earlier, the trajectories may avoid deep minima.[33] Therefore, the existence of this deep minimum in the case of the F^- + CH_3I system does not prove that this complex has a significant role in the dynamics. Therefore, we proposed a technique called trajectory orthogonal projection (TOP) to investigate the role of the front-side complex formation in the dynamics of the F^- + CH_3Cl and F^- + CH_3I S_N2 reactions.

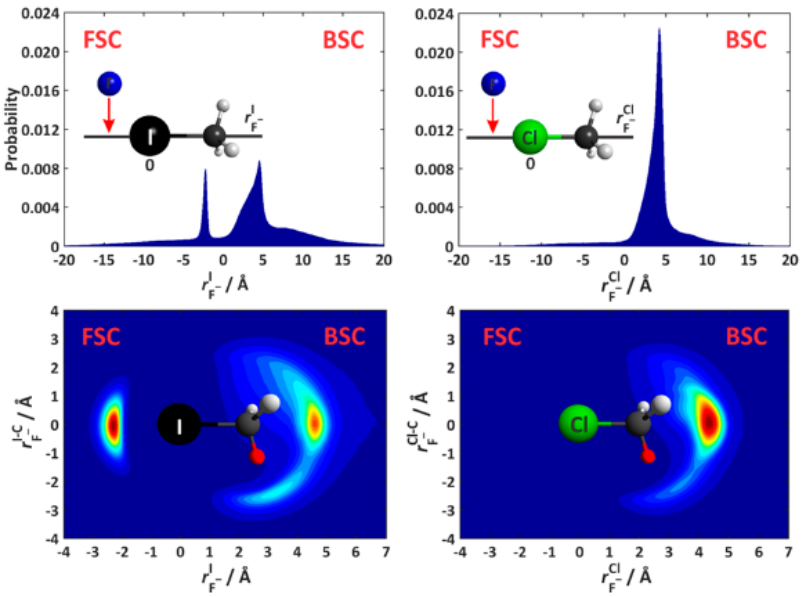

Figure 5.14.: Results of TOP (Trajectory Orthogonal Projection) at collision energy of 1 kcal/mol

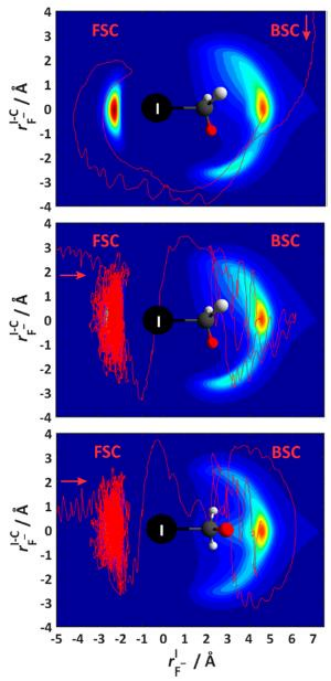

Figure 5.15.: TOP results of three representative F^- + CH_3I trajectories

The procedure starts with running trajectories at a given collision energy from b = 0 to b_{max}. After that, the three-dimensional positions of the nucleophile in the entrance channel are orthogonally projected to the linear or planar subspaces defined by certain atoms of CH_3Y. Figures 5.14 and 5.15 are the results of the trajectory orthogonal projection using the histogram analysis method which assigns different colours to different probabilities. For instance, here the darker red means larger probabilities. Figure 5.14 clearly demonstrates that only in the case of the F^- + CH_3I system has the front-side minimum a significant role. The diagrams are made based on all of the trajectory points at the collision energy of 1 kcal/mol where the C-Y distance was lower than 3.5 Å and the C-H distance was lower than 2.5 Å. The results of other collision energies give similar results.

Figure 5.15 represents the TOP results from three representative trajectories. The upper one shows a transient 0.6 ps front-side minimum formation after back-side attack. Then, the fluoride comes back to the back-side region and a Walden inversion takes place. The last two represent two trajectories with long-lived 42.1 ps front-side complex formation after front-side attack. The nucleophile then comes to the back-side region and carries out a Walden inversion.

Figure 5.16 shows the front-side complex lifetime distributions for the F^- + CH_3Y [Y = Cl,I] S_N2 reactions at different collision energies. The lifetime is calculated from the trajectory integration time spent by the F^- nucleophile in the front-side region defined as $r_{F-Y} < 0$, where r_{F-Y} is the distance of F^- from the Y leaving group after TOP. The uppers panels show the probabilities of front-side complexes with different lifetimes for different collision energies beside the maximum lifetimes of the front-side

complexes per collision energies. Front-side complex lifetime fractions split into the individual contribution of trajectories starting with front-side attack (FSA) and back-side attack (BSA). The FSA and BSA trajectories are distinguished based on the initial attack angle defined by Figure 4.1 at t = 0. Furthermore, the FSA and BSA are split into the contribution of short-lived (transient) and long-lived (strongly trapped) FSC trajectories. The latter ones are characterized by a lifetime larger than 2 and 4 ps for Y = Cl and Y= I, respectively. The fractions of these classes as the function of the collision energy are shown in the lower panels.

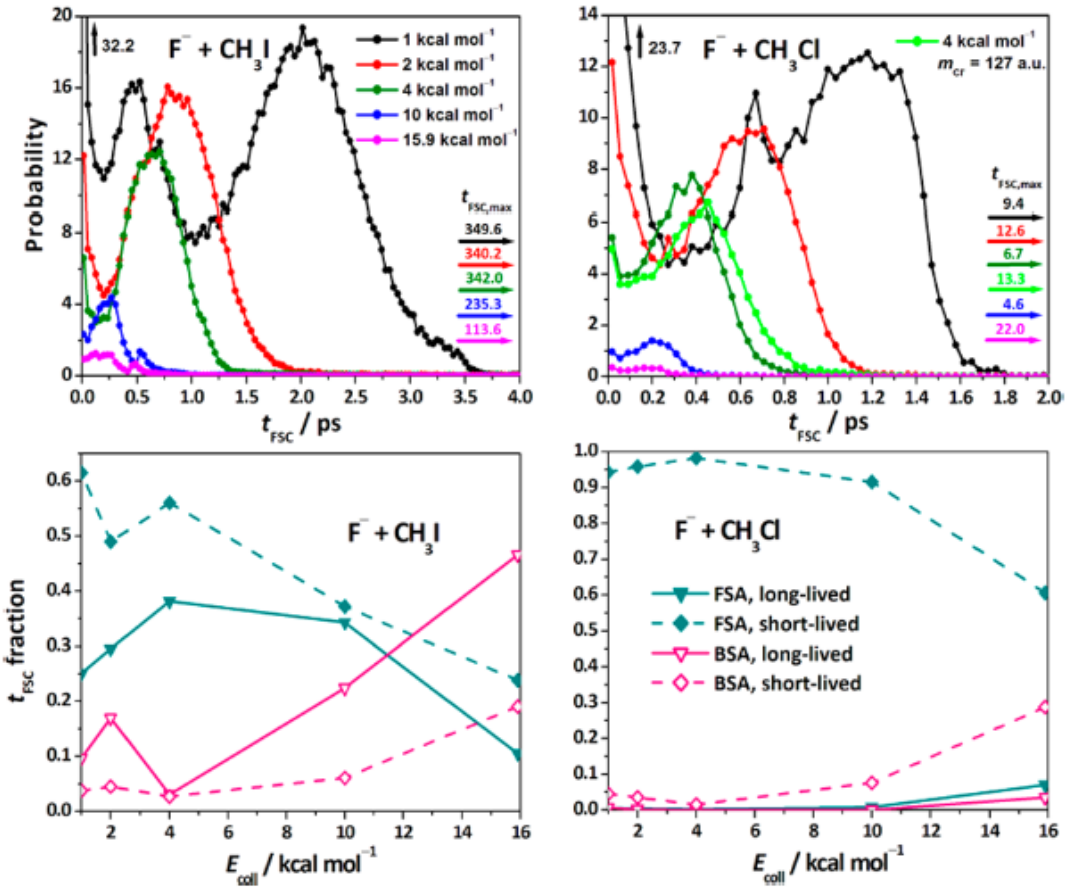

Figure 5.16.: Lifetime distributions of different complexes

5.4 Stretching vibration is spectator in nucleophilic substitution

The vibrational excitation of the reactants can influence the reaction dynamics. In the case of atom-diatom reactions the Polanyi rules[51] can be directly applicable, which states that the vibrational excitation promotes the late-barrier reactions, where the transition state has a product-like structure. We can also say that the vibrational excitation drives the endothermic reactions, because according to the Hammond postulate in the case of endothermic reactions the transition state has a product-like structure.

In the case of polyatomic systems the situation will be more complicated[52,53,54,55] because some vibrational modes can be spectator for the reaction dynamics. For example, the C-H stretching does not play significant role for the most types of S_N2 reactions.[5,56] This fact was already supported by theoretical investigations, but experimental evidence had not been existed before. Our theoretical work[20] was carried out in cooperation with a leading experimental group in the University of Innsbruck. One of our goals was to find an experimental evidence for the spectator role of the CH stretching vibration in S_N2 reactions. In addition, the role of the C-I stretching was also an important question for us. According to a quantum dynamics investigation, the C-Y, where Y is a halogen, stretching enhances the reaction at low collision energies but reduces it at higher collision energies.[57]

The experimental method is called crossed-beam ion imaging. To briefly summarize the procedure, the fluoride ions are produced by a pulsed plasma discharge of NF_3 seeded in argon. After the mass-selection of these ions, their kinetic energy is adjusted. Then, these fluoride ions are crossed with the methyl-iodide molecules with a chosen attacking angle, as Figure 5.17 illustrates. Among the products, only the ions are detectable with a time-sensitive detector. The 3D vectors of the incident product ions can be determined. The vibrational excitation of the reactants can be carried out by lasers (Figure 5.17 shows the way of the laser beam).

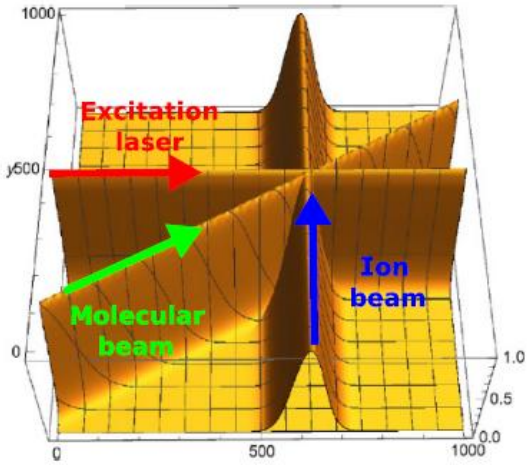

Figure 5.17.: Illustration of the experimental device

Figure 5.18 shows the time-of-flight traces for two collision energies, 0.71 and 1.17 eV (5726.5 and 9436.7 cm^{-1}). In the case of both collision energies the S_N2 channel dominates (on the upper panel the CH_2I^- traces are hundredfold enlarged), in accord with our QCT results shown in Figure 5.8. On the upper panel, the red curve shows the difference between the excited and non-excited traces and demonstrates the spectator role of the CH symmetric stretch in the case of nucleophilic substitution reactions and the enhancing role of this mode for the abstraction reaction.

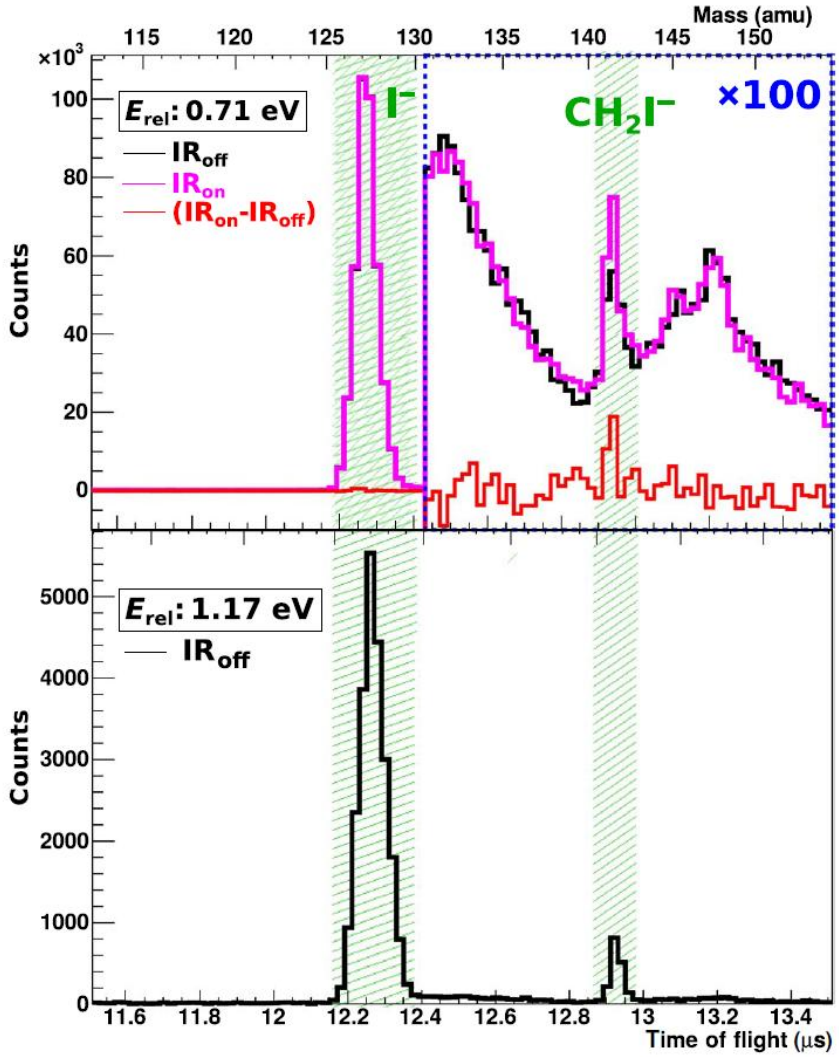

Figure 5.18.: Time of flight traces at the collision energies of 0.71 and 1.17 eV

Table 5.1 shows the effect of the excitation of the CH symmetric stretch on the reaction channels. The relative difference in the case of the S_N2 channel is barely significant, even if the growing of the absolute amount of the counts is higher than in the case of the abstraction channel, where the relative difference is hundred times that of the S_N2 reaction and highly significant.[20] The

relative rate increase takes into account the fact that the laser excitation cannot excite all of the reactant molecules. The excited fraction shows the ratio of the excited reactants and was determined to be 1.4 $\pm$ 0.5% based on the spatial and temporal overlap of the three beams shown in Figure 5.17.

Table 5.1.: Effect of the excitation of the CH symmetric stretch in the case of the experiment

	Counts (IR_{on})	Counts (IR_{off})	$IR_{on} - IR_{off}$	Rel. difference	Rel. rate increase
S_N2	389 726	388 552	1174 $\pm$ 882	(0.30 $\pm$ 0.23)%	0.21 $\pm$ 0.16
Proton transfer	1 191	911	280 $\pm$ 46	(31 $\pm$ 5)%	22 $\pm$ 4

The QCT simulations showed similar results as the experiment. I ran trajectories at the same collision energies as in the experiment. At 0.71 eV (5726.5 cm^{-1}) I found that the integral cross section for the total S_N2 reaction is 13.0 $Å^2$ in the unexcited case and 13.9 $Å^2$ in the case when the CH symmetric stretching was excited (only 6.9% enhancement). These results are in agreement with the experimental finding that the excitation of this mode has very little effect on the S_N2 channel.

It is need to be mentioned that in the case of other systems a few studies showed more significant effect of the CH symmetric stretching excitation on the S_N2 reaction route. For the $F^- + CH_3Cl$ system, the CH symmetric stretching enhanced the S_N2 reactivity by 10% to 30%, depending on the collision energy, according to QCT simulations run on a high-level potential energy surface.[5] For the $Cl^- + CH_3Br$ system, a quantum dynamics study questioned the spectator behaviour of the CH stretching for the S_N2 reaction. Due to the fact that quantum dynamics simulations can be carried out only in reduced dimensions, this finding, which disagrees with our results for the $F^- + CH_3I$ system, needs further investigation to confirm.

The upper panels in Figure 5.19 show distributions obtained by subtracting the contribution of ground-state reactions from the signal for reactions obtained with CH stretching-excited CH_3I molecules at 0.71 eV, similarly as the relative rate increase was calculated. The A panels show the velocity map of the CH_2I^- product on Newton diagrams. The red circle indicates the kinematic cutoff which shows the maximal kinetic energy which is possible without zero-point energy lesion. The B panels show the scattering angle distributions. The black lines are derived from the measured data, and the red lines show the results of the simulations, just as in the case of the C panels which show internal energy distributions. The measured and experimental data agree well in both cases. The scattering angle distributions in both panels are nearly isotropic with a slight propensity of forward and backward scattering (the cosθ values close to 1 indicates forward scattering while the cosθ

values close to −1 indicates backward scattering). In the case of vibrational ground-state reactions, this result agrees reasonably well with previous experiments[19] and direct dynamics simulations.[58] The internal energy of the products is mainly locked up in the CH_2I^- fragment; the HF acquired almost no internal excitation according to previous simulations.[58] Our results also showed that the HF fragment is prone to the ZPE lesion.[48]

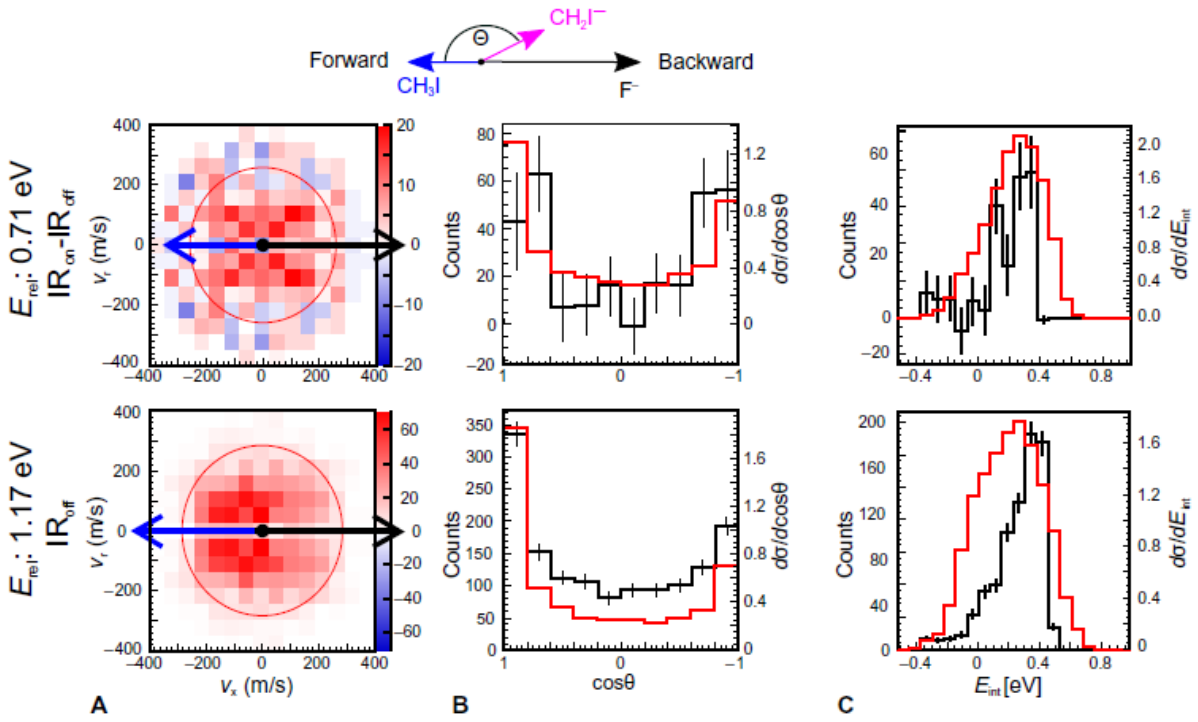

Figure 5.19.: CH_2I^- product velocity maps, scattering angle distributions and internal energy distributions at the two collision energies; the black curves indicate the results of the experiment, while the red curves indicate the results of the simulation

In order to generalize the Polanyi rules for polyatomic systems, the Sudden Vector Projection (SVP) model has been proposed. The SVP values are derived from the projection of the vibrational modes to the line of the imaginary mode of the transition state. It is important that in the case of indirect reactions this model does not work due to the energy redistribution during the trajectories. However, at 5726.5 cm^{-1}, where the effect of the excitation was investigated, according to the QCT simulations, the direct channels account more than 50% to the reactivity for the F^- + CH_3I reaction. As a result, the SVP values shown in Table 5.2 are probably appropriate to predict that which mode should be excited to promote the reactions. As expected and in accord with my QCT computations, the symmetric C-H stretching excitation promotes the proton transfer most efficiently, whereas the

C-I stretching enhances the S_N2 channel. More details and discussion on the mode-specific dynamics of the title reaction are presented in chapter 5.5.

Table 5.2.: SVP values of different vibrational modes in the case of the F^- + CH_3I proton-transfer and nucleophilic substitution (S_N2) reactions

	Proton transfer	S_N2
CI stretch	0.22	0.78
CH_3 rocking	0.09	0.00
CH_3 umbrella	0.76	0.24
CH_3 deformation	0.30	0.00
CH symmetric stretch	0.33	0.03
CH asymmetric stretch	0.10	0.00
Translation	0.02	0.16

5.5 Mode-specific quasiclassical dynamics of the F^- + CH_3I S_N2 and proton-transfer reactions

Beside the investigation of the effect of the CH symmetric stretching mode on the S_N2 and abstraction reactions both experimentally and theoretically,[20] we carried out a purely theoretical research on the effect of the other vibrational modes of the CH_3I molecule, too. This reactant molecule is nonlinear, thus has $3N–6$ vibrational modes, where N is the number of atoms, but due to degenaracy only six different vibrational modes exist instead of nine. Beside the ground-state reactant, I investigated the following vibrational excitations: the excitation of the CH symmetric stretch (v_1), the CH_3 umbrella motion (v_2), the CI stretching (v_3), the CH asymmetric stretching (v_4), the CH_3 deformation (v_5), and the CH_3 rocking (v_6). The degeneracy of the CH asymmetric stretching, the CH_3 deformation, and the CH_3 rocking can be seen in Figure 5.20, where the purple colour indicates the iodine atom. In accordance with this degeneracy, I obtained the following frequencies for the CH_3I molecule: 549 (550), 899 (922), 899 (922), 1287 (1275), 1479 (1468), 1479 (1468), 3087 (3088), 3201 (3224), and 3201 (3224) cm^{-1} at the CCSD(T)-F12b/aug-cc-pVTZ level of theory, in good agreement with the PES values shown in parentheses.

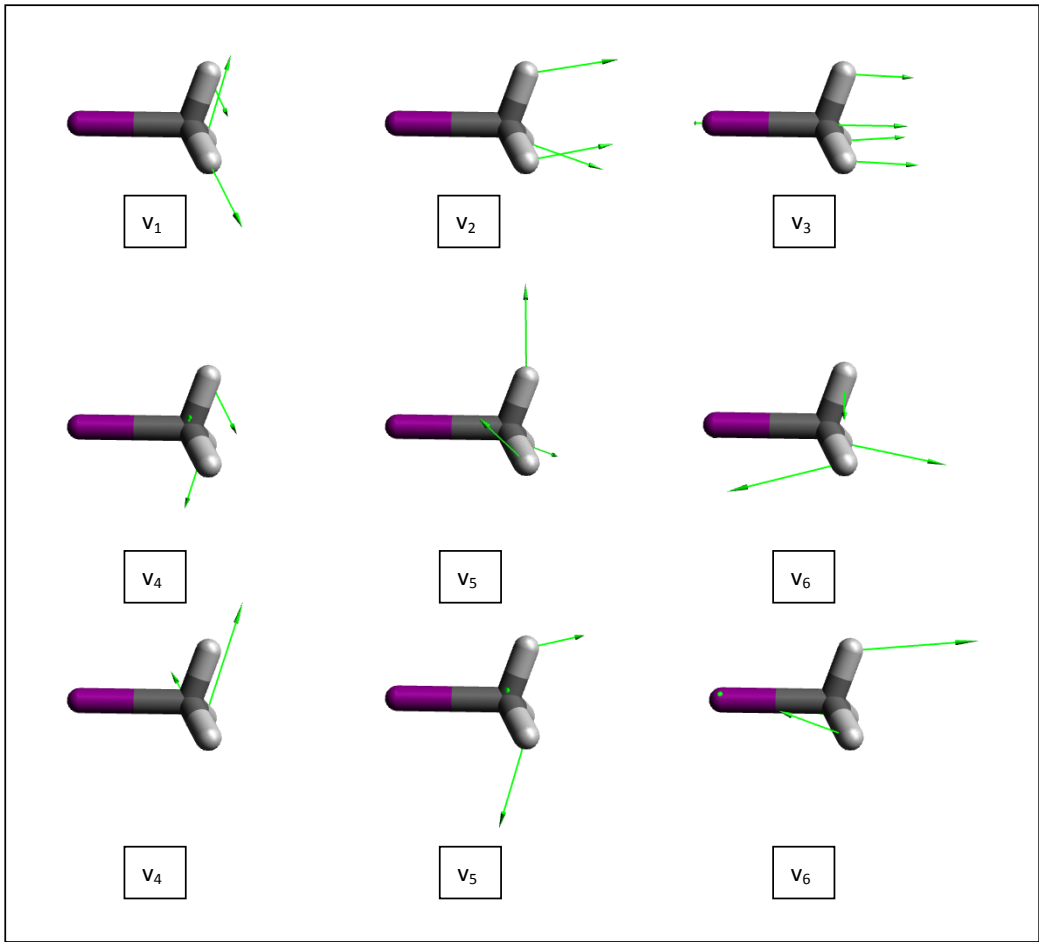

Figure 5.20.: Vibrational modes of methyl-iodide (the purple part indicates the iodine atom)

It was emphasized earlier that the SVP values which are shown in Table 5.2 for the $F^- + CH_3I$ reaction are not enough to prove which mode should be excited to promote a reaction, especially if the contribution of the indirect trajectories to the reactivity is significant. Thus, the dynamical investigation of the differently excited reactants is an important challenge for chemists.

For the $Cl^- + CH_3Cl$ and the $Cl^- + CH_3Br$ systems, some experimental and theoretical studies found evidences for the mode-selective vibrational enhancement of reactivity.[59,60,61] Above this, beside the above-mentioned quantum-dynamical study of Hennig and Schmatz,[62] they carried out other quantum-dynamical investigations for the effect of the excitation of several vibrational modes.[63,64,65] According to a 3-dimensional quantum dynamics study for the $Cl^- + CH_3I$ reaction,[66] where the C-I stretching, the C-Cl stretching and the CH_3 umbrella motion were investigated, the authors found that the excitation of the C-I stretching mode promotes the S_N2 reaction more efficiently than the excitation of the CH_3 umbrella mode. For the $F^- + CH_3Cl$ reaction the highest-dimensional quantum-dynamical investigation was carried out.[67] The 6-dimensional quantum dynamical results were in reasonably good agreement with the results of the full-dimensional QCT simulations performed on the same potential energy surface.[5] For the $F^- + CHD_2Cl$ reaction mode-specific QCT simulations were performed.[68] These studies demonstrated that the S_N2 reaction channel can be promoted by the excitation of the C-Cl stretching mode most efficiently, while the promotion of the abstraction channel can be carried out by the excitation of the C-H stretching mode in the most efficient way.

The first experimental evidence for the spectator behaviour of the CH stretching mode was provided by Roland Wester and co-workers for the $F^- + CH_3I$ S_N2 reaction in 2018, which was discussed in the latest chapter.[20] In the case of the abstraction reaction channel the excitation of this mode promoted the reaction. These results were supported by the results of our QCT simulations and with the Sudden Vector Projection (SVP) values. However, only the CH symmetric stretching mode was studied at only two collision energies.

Our comprehensive theoretical study[69] for the $F^- + CH_3I$ reaction investigates the effect of all of the different vibrational modes of the CH_3I reactant molecule at several collision energies. One of our goals was the investigation of the effect of the excitation of the normal modes of the CH_3I molecule on the double-inversion mechanism.[5,70] According to a direct dynamics study by Hase and co-workers,[71] the excitation of the vibrational modes of the methyl-iodide reactant does not promote the double-inversion reaction route of the $F^- + CH_3I$ reaction. However, due to the statistical inaccuracy of the direct dynamics studies and due to the low reaction probability of the double-inversion pathway, further investigation is required to support or disprove the above statement.

The developed potential energy surface for the $F^- + CH_3I$ reaction[48] made possible running thousands of trajectories with reactants excited of each vibrational mode at every impact parameter

at every collision energy. I used the following nine collision energies: 1.0, 2.0, 4.0, 7.4, 10.0, 15.9, 16.4, 27.0, and 35.3 kcal/mol. The collision energies of 16.4 and the 27.0 kcal/mol were used in the work discussed in the last chapter,[20] while 7.4, 15.9, and 35.3 kcal/mol were used in another theoretical-experimental study,[72] so our results[69] are comparable with the previous ones.

The b_{max} values varied between 11 and 30 bohr and the b_{step} was 0.5 bohr. I ran 5000 trajectories at every impact parameter. Considering the fact that nine different collision energies and six vibrational modes were investigated, millions of trajectories were run all in all.

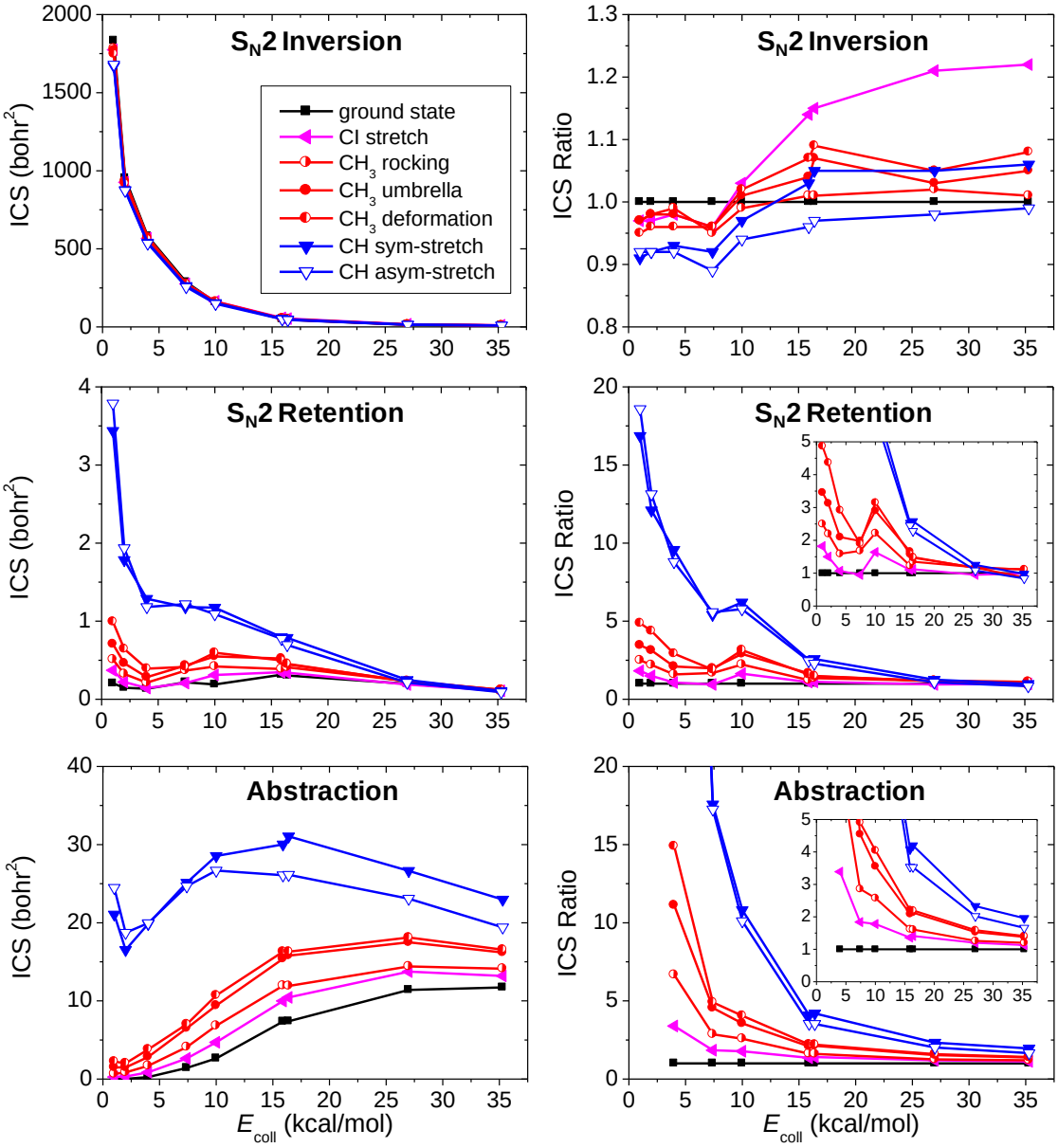

Figure 5.21.: Mode-specific ICS curves and their ratios for different reaction channels

The left-side panels in Figure 5.21 show ICS values depending on the collision energy, while the right-side panels show excited/nonexcited ICS ratios. In the case of the S_N2 inversion reaction, the right-side panel is more informative, because the large ICS values do not allow observing slight differences between them. The ICS ratios are significantly smaller than in the case of the S_N2 retention reactions and the abstraction reactions. This fact can be easily understood because the geometry of the transition state of the Walden inversion is not distorted too much in comparison with the reactant state in contrast to the transition state of the double inversion or the abstraction channels. In the lowest collision energies, the vibrational excitations hinder the S_N2 inversion which can be explained by the fact that the ICS values decrease steeply in this energy interval and the energy redistribution can be significant because the ratio of the indirect trajectories is also significant at lower collision energies. This assumption can be supported by the fact that in the case of the $F^- + CH_3Cl$ reaction, even in the 1-4 kcal/mol range the excitation of the most vibrational modes enhances the S_N2 inversion probability, because this is a more direct reaction.

In the case of higher collision energies the S_N2 inversion routes can be promoted by vibrational excitations, most efficiently by the CI stretching in agreement with the SVP values in Table 5.2. However, the SVP values predict that the umbrella motion is the second best facilitating the S_N2 inversion process, while the right upper panel in Figure 5.21 shows that the CH_3 deformation promotes it more efficiently than the umbrella motion. This fact shows that the Sudden Vector Projection model is not entirely reliable as was mentioned above.

The middle panels in Figure 5.21 show the S_N2 retention integral cross sections including the contribution of both the front-side attack and the double-inversion mechanisms. I found that these two mechanisms cannot be separated simply by the trajectory integration times in contrast to the case of the $F^- + CH_3Cl$, $F^- + CH_3F$, and $F^- + CHD_2Cl$ reactions,[5,73] thus only the overall retention cross sections are given.

The double-inversion process starts with a proton abstraction. Consequently, the leader role of the CH stretching modes facilitating the retention mechanism can be simply explained because the excitation of these modes promotes the leaving of a proton from the methyl-iodide molecule. In contrast to the case of the inversion, the vibrational excitations enhance the retention mainly at low collision energies due to the activation energy of the process. However, at higher collision energies, the ICS ratios decrease because the system has enough energy to reach the barrier height even without the vibrational excitation. The symmetric/asymmetric CH stretching excitations substantially enhance double inversion, for example, by factors of 17/19, 12/13, 10/9, 5/6, and 6/6 at collision energies of 1.0, 2.0, 4.0, 7.4, and 10.0 kcal/mol. So, we found strong contrast with the previous investigation mentioned above.[71] In the case of the highest energies the front-side mechanism

dominates over the double-inversion process. Consequently, the most efficient vibrational mode becomes the CH_3 deformation instead of the CH stretching modes.

The abstraction reaction can be promoted most efficiently by the excitation of the same modes (the symmetric and the asymmetric CH stretching) as the double-inversion process. This is not very much a surprise because both processes start with the leaving of one proton from the methyl-iodide reactant. The ICS ratios decrease similarly and for the similar reason as in the case of the retention pathway.

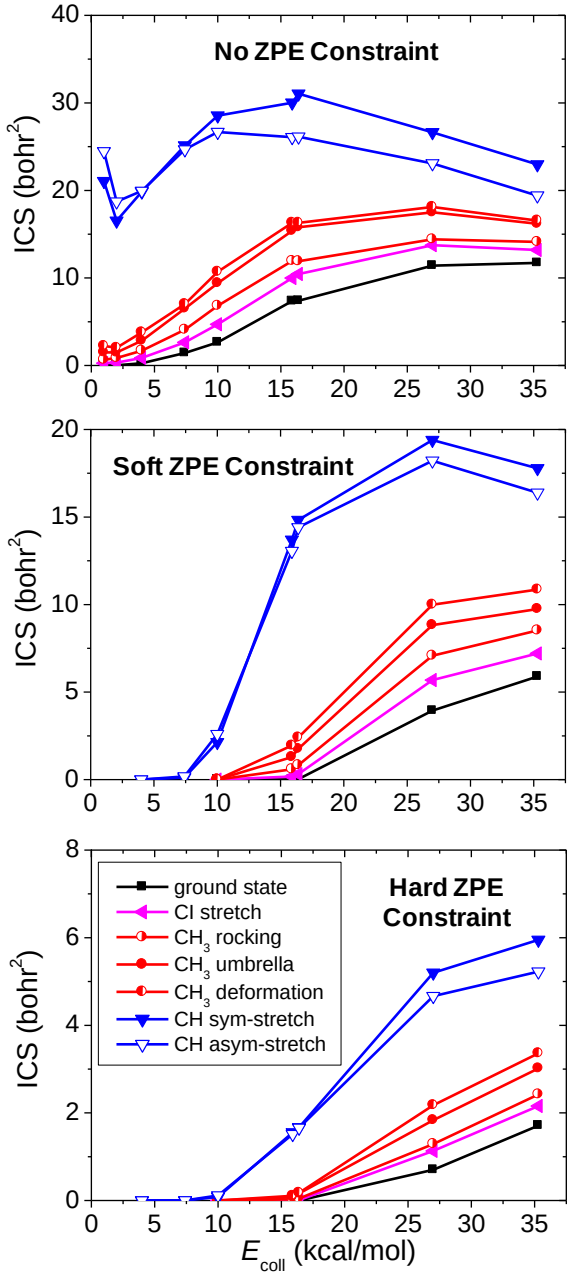

Figure 5.22.: ICS curves for the abstraction channel with and without ZPE constraints

In the case of the abstraction channel the ZPE violation is presumable. Thus, I calculated ICS values with ZPE constraints. ZPE constraint reduces the cross sections and shifts the threshold energies toward larger collision energies as can be seen in Figure 5.22. The thresholds of the upper panel which shows the thresholds without ZPE constraints, are unphysical. Reactant vibrational excitation increases the cross sections and opens the abstraction pathways at lower collision energies. The relative efficiency of the different vibrational modes promoting the proton-abstraction reaction is similar with and without ZPE constraint.

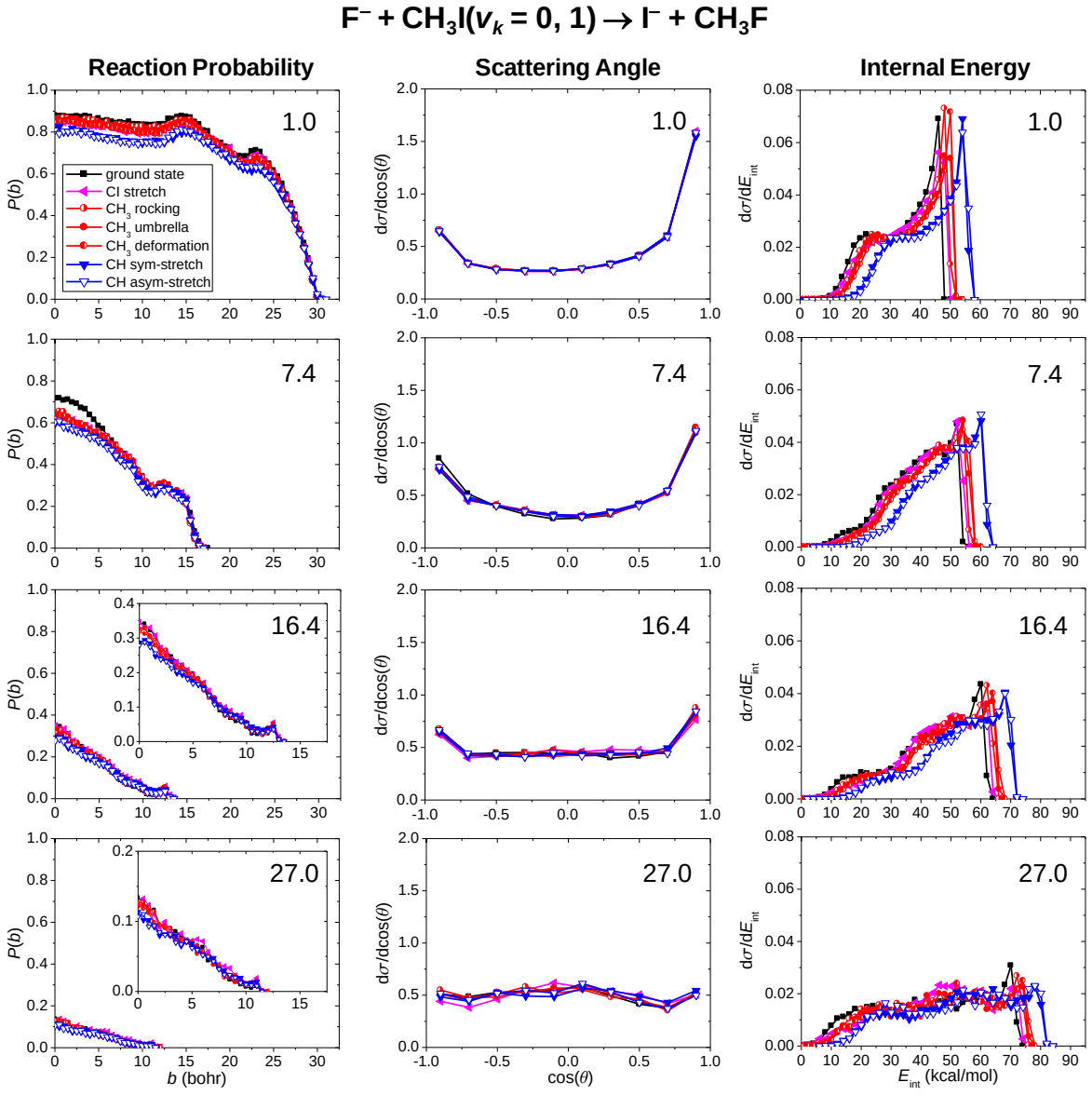

Figure 5.23.: Opacity functions, scattering angle distributions, and internal energy distributions in the case of the S_N2 reaction channel for different collision energies and excitation modes

Left panels of Figure 5.23 show the opacity functions (reaction probabilities depending on the impact parameter) for the S_N2 reaction channel. The reaction probabilities decrease with the collision energy, but at the lowest energy the long-range ion-dipole interactions delay the steep decreasing of the function. Significant mode specifity cannot be observed for the S_N2 reactions similarly to the ICS values in Figure 5.21 in contrast with the abstraction channel, where the most significant effect of the excitation of the CH stretching modes is observable. The b_{max} values of the S_N2 and proton-transfer reactions are very similar, indicating that the long-range pre-reaction interactions determine the maximum impact parameters.

The scattering angle distributions do not show mode specifity neither for the S_N2 nor the abstraction reactions. The S_N2 scattering angle distributions show forward preference beside the nearly isotropic scattering at lower collision energies indicating indirect mechanisms. Figure 5.24 shows that for the highest collision energy slight backward dominance can be observed due to the increased probability of direct reactions. The abstraction scattering angle distributions show backward-forward scattering with forward dominance at the highest collision energies in good agreement with the results in Figure 5.19.[20] This finding shows the high probability of the stripping abstraction mechanism.

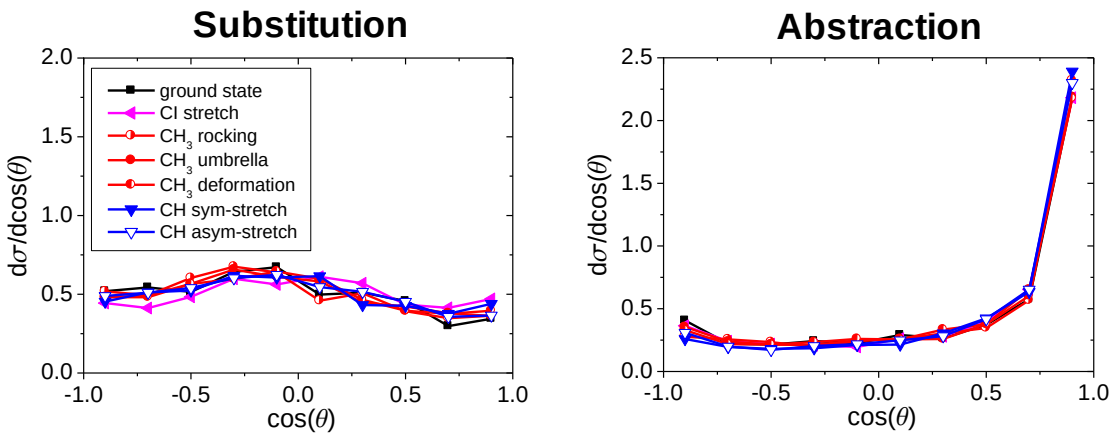

Figure 5.24.: Mode-specific scattering angle distributions for the S_N2 and proton-abstraction channels of the $F^- + CH_3I$ reaction at collision energy of 35.3 kcal/mol

Considering the internal energy distributions of the CH_3F product, the energy values are shifted towards the higher energies in the case of lower collision energies indicating indirect mechanisms. The broading of the distribution toward the higher energies is observable with increasing collision energies. Here mode specificity occurs in that way that the distributions shift

toward larger energies and the shifting is virtually the same as the initial vibrational excitation energy.

The distributions of the CH_2I^- product internal energies relative to the ZPE energy of the CH_2I^- ion can be seen on the right panels of the Figure 5.25. The ZPE violation is significant especially at lower collision energies. At 1.0 kcal/mol only the CH-stretching excited reactants produce physically proper products which is in agreement with the diagrams of Figure 5.22. The fact that the distributions are cold and Gaussian-like also corresponds to the high endothermicity of the abstraction reaction.

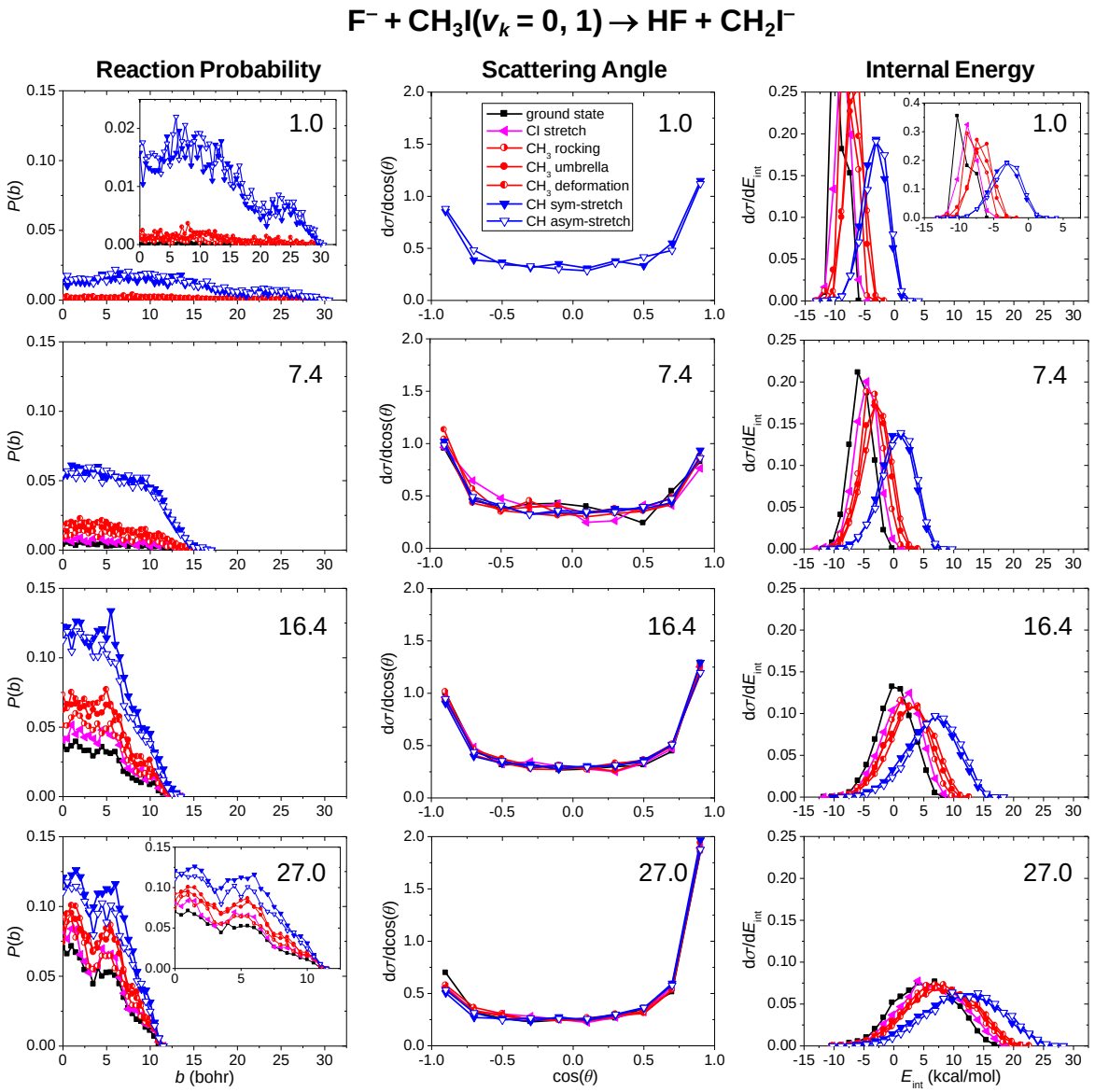

Figure 5.25.: Opacity functions, scattering angle distributions, and internal energy distributions in the case of the abstraction reaction channel for different collision energies and excitation modes

5.6 Uncovering the role of the stationary points in the dynamics of the $F^- + CH_3I$ reaction

Traditionally the role of the stationary points in the chemical reaction dynamics has been observed watching trajectory animations. For example, the previously mentioned finding that in the case of the $OH^- + CH_3F \rightarrow CH_3OH + F^-$ S_N2 reaction, most of the trajectories do not approach the deep minimum in the postsubstitution region is based on such observations. During my PhD work I composed a Fortran code which assigns the trajectory points to stationary points thereby automatizing this process. The code uses the Eckart transformation described earlier to find the best overlap between two geometries. After that, the stationary point with the least RMS value is assigned to the trajectory point. The RMS of an N-atomic system with N_{stat} stationary points is defined as

$$RMS(k) = \sqrt{\sum_{i=1}^{N}\sum_{n=1}^{3}\left((\mathbf{C}_k\mathbf{r})_{i,n} - (\mathbf{r}_{i,n}^{\mathrm{stat}})_k\right)^2/N} \quad , \quad k = 1,2,\dots,N_{\mathrm{stat}} \tag{88}$$

In the case of the F^- + CH_3I reaction, Eq. (88) corresponds to the root-mean-square value of the R(H1–H1'), R(H2–H2'), R(H3–H3'), R(C–C'), R(F–F') and R(I–I') distances, where ' labels the atoms of the stationary point.

Among the eight **C** matrices defined by equation (82) four make pure rotations, while the other four describe pseudo-rotation (rotation+inversion). Therefore, in our case, the permutation of the hydrogen atoms is partly solved by the four pseudo-rotation matrices. Despite this fact, I carried out all of the six permutations of the hydrogen atoms in my code, and just after a permutation performed the Eckart transformation. I found that in the case of the C_{3v} stationary points the six permutations were all equal due to four pseudo-rotation matrices of the Eckart transformation. However, for the stationary points with C_s symmetry 3 different RMS values were calculated. So, the permutational symmetry is not managed perfectly by the Eckart transformation.

It is very important that I did not assign every trajectory points to stationary points because our goal was to study only the reactive region. Thus, I defined a reactant region and different product regions and if the trajectory point belonged to either of these regions the point was not assigned to stationary point. For instance, the reactant and the S_N2 product regions were defined as: if $r_{C\text{-}I} < 3.2$ Å and $r_{Cl\text{-}F} > 5.0$ Å and all $r_{C\text{-}H} < 2.0$ Å, where $r_{Cl\text{-}F}$ is the distance of the middle of the C-I bond to the F atom then this is the reactant region and if $r_{C\text{-}I} > 3.2$ Å and $r_{C\text{-}F} < 2.2$ Å and $r_{CF\text{-}I} > 5.0$ Å and all $r_{C\text{-}H} <$ 2.0 Å, where $r_{CF\text{-}I}$ is the distance of the middle of the C-F bond to the I atom then we are in the S_N2 product region.

Similar assignment techniques were used previously for quasiclassical product analysis.[74,75] My supervisor and his co-workers used trajectory assginments while studying water cluster

dynamics.[76,77] In 2012 an Eckart-transformation method was published,[44] which proved useful for atom + methane[78] and S_N2 reactions[35] and played an important role in the discovery of the double-inversion mechanism by my supervisor and his student István Szabó.[5] Finally a recent work should be mentioned describing an assignment procedure of the trajectory points to IRC points,[79] similarly to our investigation.

I used the trajectories from the study described in chapter 5.2. In brief, with vibrationally unexcited reactants reactions at the following collision energies were investigated: 1.0, 4.0, 7.4, 10.0, 15.9, 35.3, and 50.0 kcal/mol. Our goals were calculating and plotting stationary-point probability distributions, root-mean-square distance distributions, stationary-point-specific trajectory orthogonal projections, transition probability matrices, and time evolutions of the stationary points.[80]

Similar probabilities as the reaction probabilities described by equations (65) and (66) can be obtained for the trajectory points in this investigation. In the probability expression

$$P(k,b) = \frac{N(k,b)}{N_{\mathrm{total}}(b)} \tag{89}$$

the numerator is the number of configurations assigned the k^{th} stationary point at impact parameter b and the denominator is the total number of configurations in the interaction region recorded for all the trajectories (nonreactive and reactive independently from the reaction channels) at a given impact parameter. I calculated the b-weighted stationary-point probability as:

$$\langle P(k) \rangle = \int_0^{b_{\max}} 2\pi b P(k,b) \mathrm{d}b / \pi b_{\max}^2 \,. \tag{90}$$

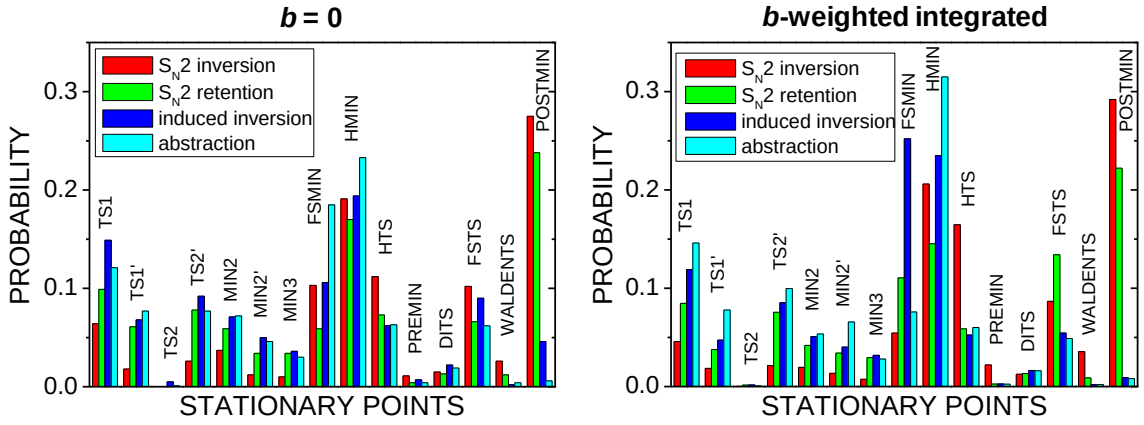

Figure 5.26.: Normalized stationary-point probabilities at collision energy of 35.3 kcal/mol

Figure 5.26 shows stationary-point probabilities at 35.3 kcal/mol. On the left panel the reaction probabilities according to Eq. (89) are plotted at zero impact parameter. On the right panel the *b*-weighted stationary-point probabilities are shown. I calculated and plotted all of the probabilities separetely for the four reaction pathways which are of our interest in this study. Significant amount of the abstraction stationary points (the left side of the panels until MIN3) can be observed in the case of all pathways indicating the indirect nature of the S_N2 reactions and the induced inversion even at higher collision energies. The important role of the front-side minimum discussed in detail in chapter 5.3 can be observed beside the principal role of the HMIN (the stationary-point geometries are shown in Figure 5.1). The low probabilities belonging to the PREMIN were unexpected. Consequently, I carried out trajectory orthogonal projections (TOPs) in the entrance channel as can be seen in Figure 5.27. The TOP for the FSMIN, HMIN, HTS, and PREMIN stationary points shows that I assigned few trajectory points to the PREMIN which are similar to the PREMIN and also to the HMIN and HTS stationary points.

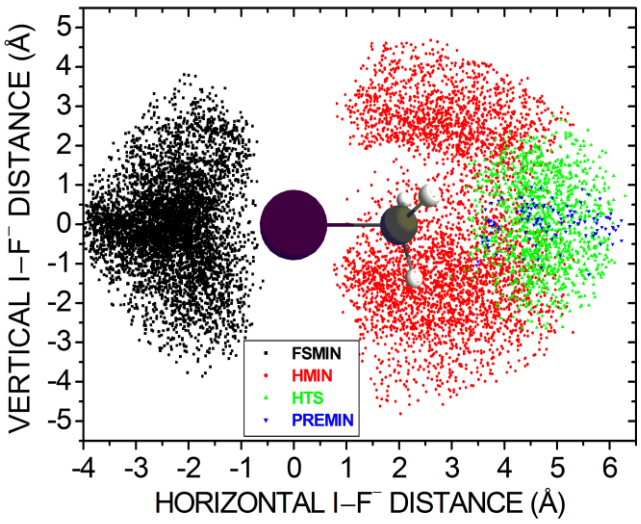

Figure 5.27.: Distributions of four stationary points in the entrance channel after trajectory orthogonal projection onto one of the ICH plane of the CH_3I molecule

The double-inversion transition state appears in all channels. This finding needs to be explained in the case of the abstraction channel and the inversion channel. The trajectories can approach this stationary point without occuring an inversion. Above this, with even number of turnovers of the two hydrogen atoms of the CH_2I^- the configuration remains the original. For example, after two turnovers the HF can give back the proton to the CH_2I^- and nothing happened overall. The DITS and WALDENTS stationary points have low probabilities for all channels, because the trajectory points which are similar to these geometries have high energies. Beside this fact, only

very similar trajectory points can be assigned to these two stationary points, which can be seen in the low RMS values in Figure 5.28. The assignment of the FSTS in the case of non-retention trajectories is caused by the transitions between the backside and frontside regions, because no other stationary point covers this side region. This statement can be supported by the large RMS values belonging to this stationary point and some of transitions in Figure 5.29, which shows the probabilities of the transitions between the differently assigned trajectory points.

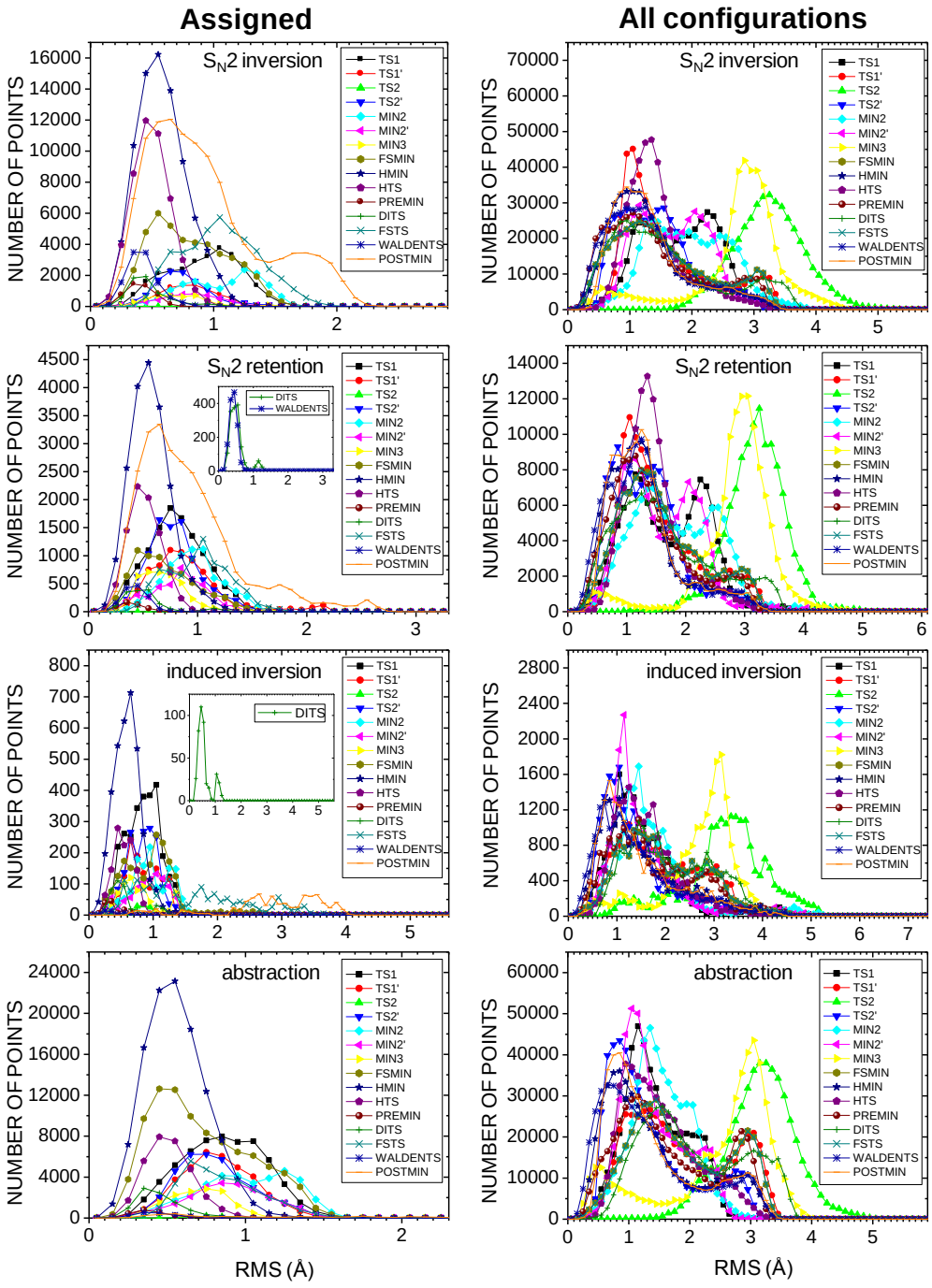

Figure 5.28.: Distribution of the RMS deviations of the trajectory points relative to the assigned and all the stationary points at *b* = 0 and collision energy of 35.3 kcal/mol

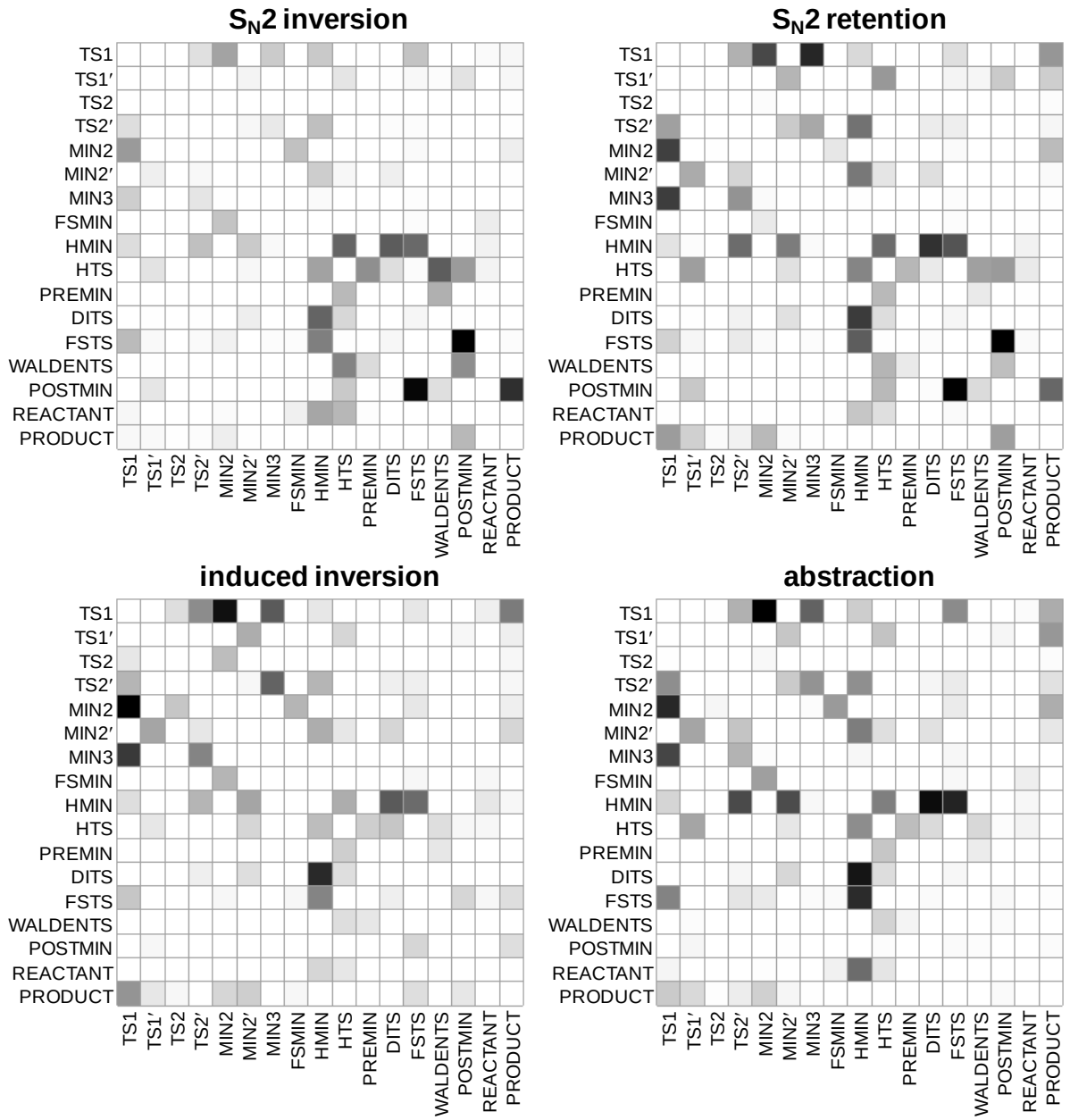

Figure 5.29.: Transition probability matrices for the stationary points at $b = 0$ and collision energy of 35.3 kcal/mol. Darker matrix elements correspond to higher probabilites for row → column transitions between stationary points.

The appearance of the POSTMIN stationary point in induced inversion and abstraction trajectories can only be explained by recrossings, when the trajectory returns from the postsubstitution region. The PRODUCT → POSTMIN and POSTMIN → WALDENTS transitions indicate recrossing trajectories.

Figure 5.28 shows RMS distributions of the trajectory points at $b = 0$ and collision energy of 35.3 kcal/mol relative to the assigned and all the stationary points.[80] The RMS curves often peak around 0.5 Å considering the RMS values of the assigned stationary points. Obviously, the RMS

curves peaks at larger values considering the deviations of every trajectory points from all of the stationary points (these curves can be seen in the right panels). I explained earlier the RMS curves of the front-side, the double inversion and the Walden inversion transition states. Lots of large RMS values belong to the POSTMIN stationary point even if we consider only the deviations from the points assigned to it, similarly to the case of the FSTS. This means that these stationary points cover large configuration space. Considering the RMS curves from the deviations of not just the assigned stationary points, high peaks belong to the TS2 and the MIN3. The largest peaks belong to the TS2 in agreement with Figure 5.26 which shows that this is the rarest-assigned stationary point.

Figure 5.29 shows transition probability matrices at $b = 0$ and collision energy of 35.3 kcal/mol where the darker colours mean higher probabilities of the transitions from the assigned stationary points labelled at the rows of the matrices to the stationary points labelled at the columns of the matrices. The matrix is almost symmetric which supports the indirect nature of this reaction showing that reactions with consecutive stationary points are rare. For example, TS1 $\rightarrow$ MIN2 and MIN2 $\rightarrow$ TS1 transitions have similar probabilities because these stationary points have very similar structures and energies. WALDENTS $\rightarrow$ POSTMIN transitions and POSTMIN $\rightarrow$ WALDENTS transitions also occur, indicating recrossings, as mentioned above. WALDENTS has about 37 kcal/mol higher energy than POSTMIN, thus POSTMIN $\rightarrow$ WALDENTS transitions have signicantly lower probabilities. The energy difference between FSTS and HMIN is similarly high, but the FSTS $\rightarrow$ HMIN and HMIN $\rightarrow$ FSTS transitions have similar probabilities because lots of trajectory points are assigned to the front-side transition state, which have much lower energies than the FSTS. There are also lots of trajectory points assigned to the POSTMIN which stand not close to it in geometry, but this is a low-energy region thus the energies of all these points are similarly low as the energy of the POSTMIN. In the case of the abstraction product region recrossings also occur which can be seen mainly in PRODUCT $\rightarrow$ TS1 transitions.

From the reactant region the trajectories approach the HMIN and HTS with highest probability, but the REACTANT $\rightarrow$ FSMIN transitions also have significant probabilities in some cases, and REACTANT $\rightarrow$ TS1 transitions also occur. The PREMIN can be reached from HTS, WALDENTS can be reached also from HTS and with smaller probability from PREMIN. The trajectories reach the S_N2 PRODUCT region usually from WALDENTS, except in the case of the S_N2 retention trajectories at the collision energy of 50.0 kcal/mol (shown in Figure 5.30), where the probability of the front-side mechanism reactions is high, so the FSTS $\rightarrow$ PRODUCT transitions have similar probabilities as the POSTMIN $\rightarrow$ PRODUCT transitions. In the case of the abstraction channel the product region is reached from abstraction stationary points, mainly from TS1, TS1', and MIN2. MIN3 $\rightarrow$ PRODUCT

transitions are very rare which is a surprising and interesting finding considering Figure 5.1 and previous work.[81]

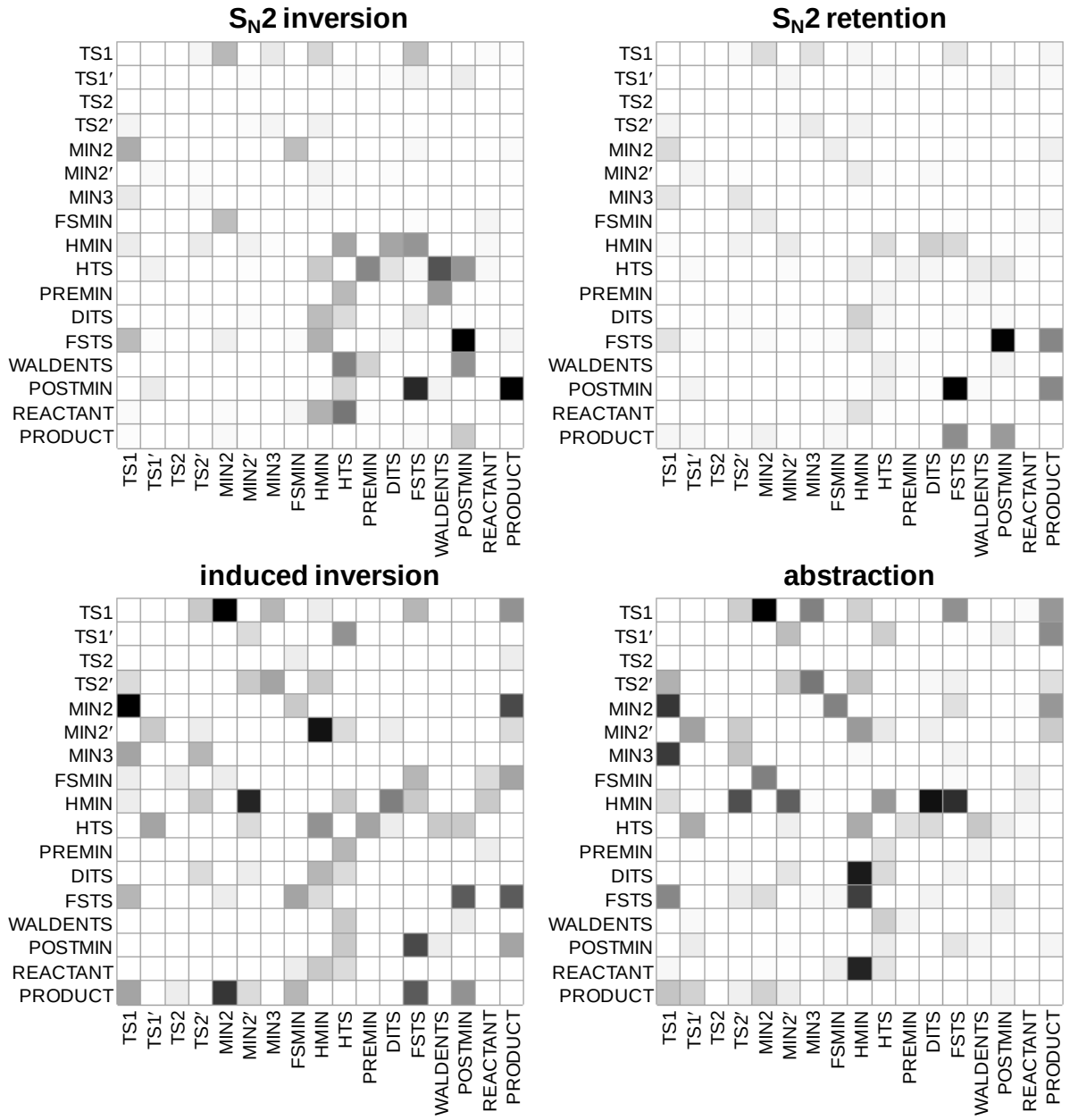

Figure 5.30.: Transition probability matrices for the stationary points at $b = 0$ and collision energy of 50.0 kcal/mol. Darker matrix elements correspond to higher probabilites for row → column transitions between stationary points.

5.7 Electronic structure theory study of the microsolvated $F^-(H_2O) + CH_3I$ S_N2 reaction

The investigations of reactions in solution are of fundamental importance in chemistry. The theoretical studies of solvated systems at high level have difficulties due to the size of the system. Our work presents for the $F^-(H_2O) + CH_3I$ reaction geometries at CCSD(T)-F12b/aug-cc-pVDZ(-PP) level at the first time.[82] Very few geometry optimizations were carried out for the microhydrated $F^- + CH_3I$ system previously. Zhang and co-workers found geometries along the $F^- + CH_3I \rightarrow CH_3F + I^-$ Walden-inversion pathway in microhydrated case at the MP2(ECP)/aug-cc-pVDZ(-PP) and DFT levels with various functionals and carried out single-point energy computations at the CCSD(T)(ECP)/aug-cc-pVTZ(-PP) level for the geometries optimized at MP2(ECP)/aug-cc-pVDZ(-PP) level.[83] I constructed a Walden-inversion energy diagram which is qualitatively the same, but the geometries are optimized at higher level. Similar optimizations at MP2 and DFT levels were carried out by Davico.[84]

Most of the studies are direct dynamics simulations for this reaction.[85,86,87,88,89] One of my goals was to confirm the stationary points found earlier by lower-level optimizations and direct dynamics simulations. Above this, I found novel stationary points, too. I started every optimization at the computationally unexpensive DF[†]-MP2(ECP)/aug-cc-pVDZ(-PP) level of theory, then I optimized this geometry at MP2(ECP)/aug-cc-pVDZ(-PP) level and the geometry found at this level was optimized at MP2(ECP)/aug-cc-pVTZ(-PP) level. Finally, I optimized the MP2(ECP)/aug-cc-pVTZ(-PP) structure at CCSD(T)-F12b(ECP)/aug-cc-pVDZ(-PP) level and made single-point calculations at this geometry at CCSD(T)-F12b(ECP)/aug-cc-pV*n*Z(-PP) [*n* = 3(T) and 4(Q)] levels. Thus, the highest-level classical energies were obtained at the CCSD(T)-F12b(ECP)/aug-cc-pVQZ(-PP) level and the highest-level adiabatic energies were obtained at CCSD(T)-F12b(ECP)/aug-cc-pVQZ(-PP) level with ZPE-correction at CCSD(T)-F12b(ECP)/aug-cc-pVDZ(-PP). It is need to be mentioned that two stationary points are found from IRC computations (DIMIN1 and DIMIN2).

The main goal of my research was to construct reaction energy diagrams using the stationary-point geometries (Figure 5.31) and energies (Table 5.3). A question arises whether one water molecule is enough to describe the real hydrated system. According to a recent study,[89] even if more water molecules are bonded to the fluoride ion, the reaction proceeds probably only with one water presumably due to stereochemical reasons. Davico concluded the same in the above mentioned article.[84] Note that the barriers can be higher if the reactants are solvated by more molecules than the transition states, but the energies of the minima and transition states relative to each other are realistic on the energy diagrams shown in Figures 5.32–5.36. These diagrams are based on chemical intuition and prior work[83,86,87,89] and sometimes are supported by IRC

[†] DF means density fitting

computations. In the following section, I will discuss in detail these reaction pathways and the stationary points involved in them.

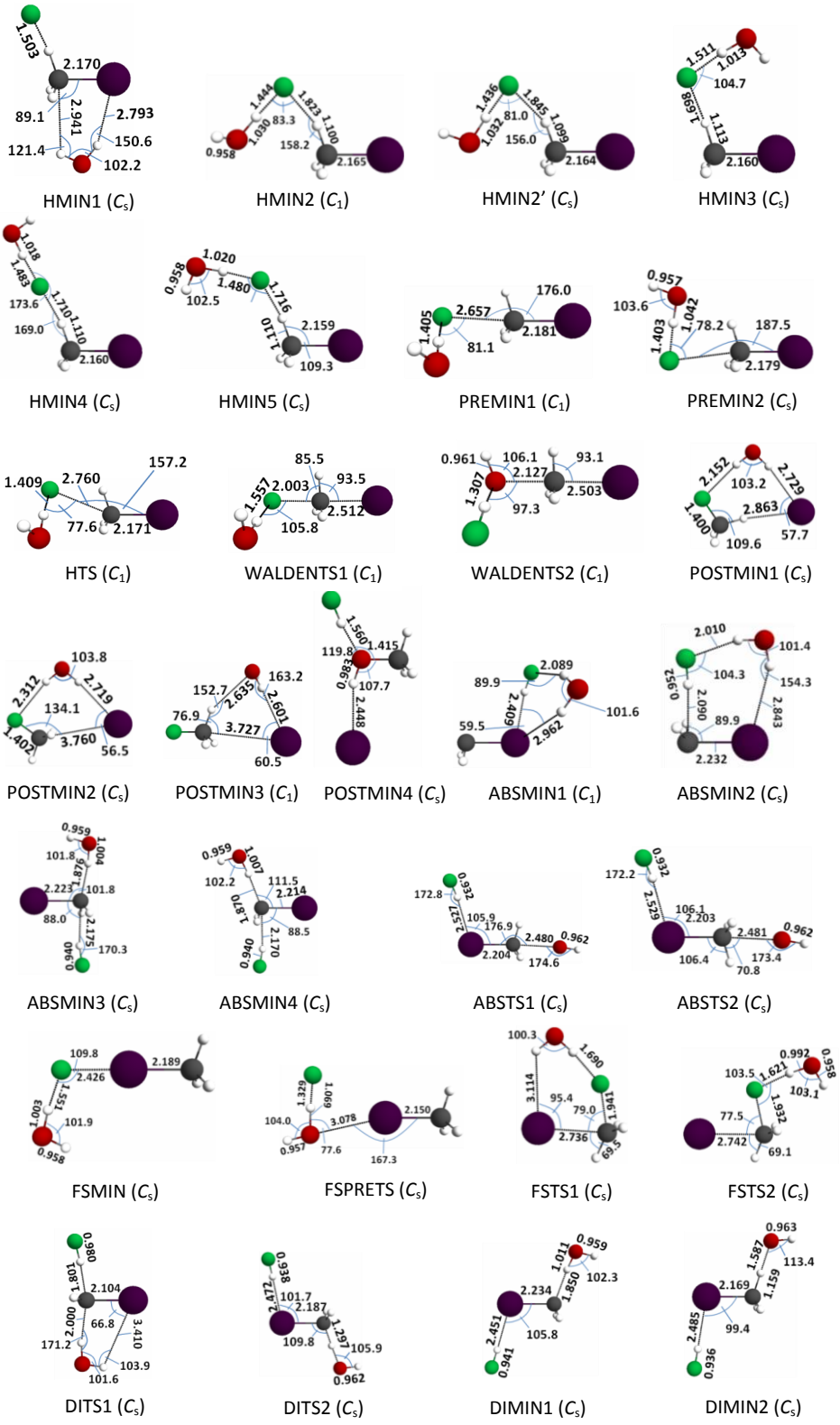

Figure 5.31.: 29 stationary-points structures of the $F^-(H_2O)$ + CH_3I system. The geometric parameters and the point-group symmetries shown in parentheses are CCSD(T)-F12b/aug-cc-pVDZ(-PP) data (bond lengths in Å, the angles in degrees).

Table 5.3.: Relative energies (kcal/mol) of the stationary points of the $F^-(H_2O)$ + CH_3I system at different levels of theory

	MP2		CCSD(T)-F12b			
	AVDZ[a]	AVTZ[b]	AVDZ[c]	AVTZ[d]	AVQZ[e]	AVQZ + ΔZPE[f]
$CH_3I + F^- + H_2O$	26.8	27.6	27.8	27.7	27.5	26.8
$CH_3F + I^- + H_2O$	−16.2	−15.2	−19.6	−19.5	−20.2	−19.2
$CH_3OH + I^- + HF$	−16.0	−14.8	−18.6	−18.6	−19.4	−19.9
$CH_2I^- + HF + H_2O$	50.7	50.2	46.8	46.5	46.3	42.0
$CH_3OH + I^-(HF)$	−32.4	−32.2	−35.4	−35.4	−35.8	−35.1
$CH_3OH(HF) + I^-$	−25.8	−24.7	−28.5	−28.3	−28.3	−25.8
HMIN1	0.8	1.9	1.0	1.3	1.4	1.7
HMIN2	−14.7	−14.0	−15.0	−14.7	−14.4	−13.3
HMIN2’	−14.7	−14.0	−15.0	−14.5	−14.4	−13.5
HMIN3	−14.0	−13.3	−14.4	−14.1	−13.9	−12.5
HMIN4	−13.9	−13.3	−14.4	−14.2	−14.0	−13.0
HMIN5	−13.8	−13.3	−14.3	−14.0	−13.8	−13.0
PREMIN1	−14.0	−13.3	−14.4	−14.1	−13.9	−12.8
PREMIN2	−14.0	−13.3	−14.1	−13.9	−13.7	−13.1
HTS	−13.9	−13.3	−14.2	−13.9	−13.7	−12.9
WALDENTS1	−8.0	−5.6	−8.7	−8.8	−8.8	−7.6
WALDENTS2	−3.3	−2.1	−3.9	−3.9	−3.8	−3.7
POSTMIN1	−34.3	−33.3	−37.5	−37.0	−37.2	−34.0
POSTMIN2	−34.8	−33.1	−37.3	−36.9	−37.2	−34.2
POSTMIN3	−35.5	−34.4	−38.5	−38.2	−38.5	−35.7
POSTMIN4	−46.3	−45.9	−49.0	−48.6	−48.8	−45.1
ABSMIN1	27.8	26.7	23.4	23.4	23.6	22.8
ABSMIN2	24.6	23.8	20.8	21.1	21.3	21.1
ABSMIN3	17.8	17.2	14.8	15.2	15.4	15.1
ABSMIN4	19.0	18.2	16.1	16.5	16.7	16.2
ABSTS1	23.3	22.9	23.2	23.3	23.5	22.0
ABSTS2	23.3	22.8	23.2	23.2	23.4	22.0
FSMIN	−13.6	−13.7	−14.6	−14.6	−14.5	−13.4
FSPRETS	−4.7	−4.9	−4.8	−4.7	−4.6	−4.8
FSTS1	32.2	34.1	30.0	29.7	29.7	30.7
FSTS2	33.4	35.7	31.6	31.4	31.4	32.1
DITS1	23.2	21.2	20.5	20.8	21.0	20.0
DITS2	21.2	20.5	20.5	20.8	21.1	17.5
DIMIN1	19.0	17.9	15.8	16.0	16.3	15.1
DIMIN2	20.2	19.7	19.8	20.2	20.5	18.9

[a] MP2/aug-cc-pVDZ energies at MP2/aug-cc-pVDZ geometries

[b] MP2/aug-cc-pVTZ energies at MP2/aug-cc-pVTZ geometries

[c] CCSD(T)-F12b/aug-cc-pVDZ energies at CCSD(T)-F12b/aug-cc-pVDZ geometries

[d] CCSD(T)-F12b/aug-cc-pVTZ energies at CCSD(T)-F12b/aug-cc-pVDZ geometries

[e] CCSD(T)-F12b/aug-cc-pVQZ energies at CCSD(T)-F12b/aug-cc-pVDZ geometries

[f] CCSD(T)-F12b/aug-cc-pVQZ energies at CCSD(T)-F12b/aug-cc-pVDZ geometries with CCSD(T)-F12b/aug-cc-pVDZ zero-point energy corrections (ΔZPE)

The energies of the stationary points are relative to the reactants consist of $F^-(H_2O)$ complex and CH_3I molecule, because experimentally these reactants are studied.[90,91,92] The formation of the $F^-(H_2O)$ complex from F^- and H_2O is an exothermic process. The D_e[‡] and D_0[§] dissociation energies of the complex are 27.5 and 26.8 kcal/mol, respectively, as Figure 5.36 shows.

The point-group symmetries of the stationary-point structures are either C_1 or C_s, as indicated in Figure 5.31. Based on Table 5.3, the good basis set convergence of the F12b method is observable. The MP2 relative energies with the aug-cc-pVDZ (AVDZ) and aug-cc-pVTZ (AVTZ) basis sets usually agree within 1 kcal/mol, but for FSTS1, FSTS2, and DITS1 the AVDZ and AVTZ energies differ by 1.9, 2.3, and 2.0 kcal/mol, respectively. However, in the case of the explicitly correlated CCSD(T)-F12b method the AVDZ and AVTZ results agree within 0.5 kcal/mol, and the above-mentioned substantial FSTS1, FSTS2, and DITS1 deviations reduce to only 0.3, 0.2, and, 0.3 kcal/mol, respectively. The agreement between the CCSD(T)-F12b AVTZ and AVQZ energies is usually even better, the differences between them are within 0.3 kcal/mol in most cases. Comparison of the MP2 and CCSD(T)-F12b relative energies reveals in some cases large deviations of around 4 kcal/mol, such as for the product channels, POSTMINs, FSTS1, and FSTS2. Considering the ZPE corrections, they can be significant, especially for some of the product-like structures. The ZPE effects are around 3 kcal/mol for the hydrated postreaction ion−dipole complexes (POSTMIN1, POSTMIN2, POSTMIN3, and POSTMIN4), and the correction decreases the endothermicity of the CH_2I^- + HF + H_2O abstraction product channel by 4.3 kcal/mol and the endothermicity of the $CH_3OH(HF)$ + I^- product channel by 2.5 kcal/mol. For the other cases, including various minima, transition states, and product channels, the ZPE effects are usually around 1 kcal/mol.

Figure 5.32 shows the Walden inversion reaction route which is similar but more complicated than in the nonhydrated case. The procession starts with a H-bonding minimum and H-bonding transition state, continues with an ion-dipole complex and the Walden transition state. The postsubstitution region consists of five stationary points according to direct dynamics simulations.[86] The first two postsubstitution complexes were difficult to find because the PES is very flat in this region and the optimization always found another stationary point when I tried to find them. In addition to this, these three complexes describe well this region and other studies also deal just with these three stationary points.[87,83]

It is important to compare the relative energies of the stationary points of the monohydrated system with the nonhydrated system. Due to the fact that the reactants are stronger hydrated than the minima and transition states, the relative energies of the hydrated analogues are always higher. Considering the prereaction stationary points of the Walden reaction route, the energies of the

[‡] best classical energies
[§] best adiabatic energies

hydrated stationary points relative to the reactants are –13–14 kcal/mol, while the energies of the nonhydrated analogues are 3-5 kcal/mol deeper. The relative energy of the hydrated Walden transition state is about 8 kcal/mol higher than the nonhydrated one. In the exit channel the three complexes are about 18 kcal/mol higher in energies than the nonhydrated analogues. This fact is in accord with the significantly higher hydration energy of the F^- ion in comparison with the hydration energy of the I^- ion.

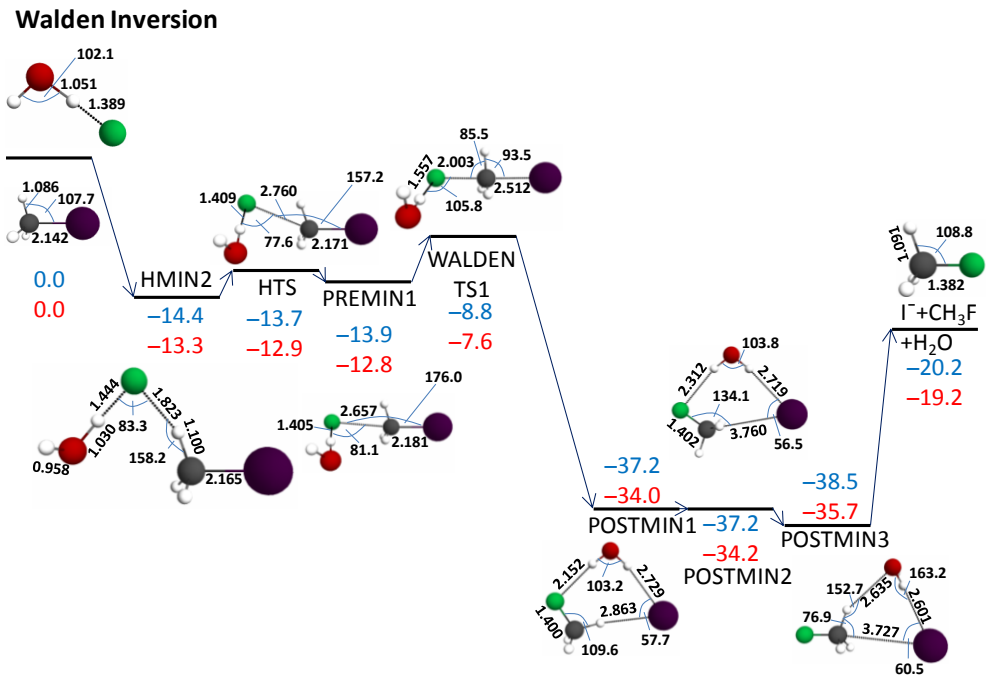

Figure 5.32.: Stationary-point structures along the Walden inversion pathway of the $F^-(H_2O)$ + CH_3I reaction (bond lengths in Å, angles in degrees obtained at CCSD(T)-F12b/aug-cc-pVDZ level). Energies relative to the reactants labelled with blue are the best classical energies calculated at CCSD(T)-F12b/aug-cc-pVQZ level at CCSD(T)-F12b/aug-cc-pVDZ geometries. Energies relative to the reactants labelled with red are the best adiabatic energies calculated at CCSD(T)-F12b/aug-cc-pVQZ level at CCSD(T)-F12b/aug-cc-pVDZ geometries with CCSD(T)-F12b/aug-cc-pVDZ ZPE-correction.

Considering the geometries of the stationary points, the HMIN2 has no symmetry because I find that the analogue with C_s symmetry has somewhat higher energy. Considering the most important geometric parameters of this complex, the H-bonded CH bond length is slightly stretched by 0.014 Å in comparison with the CH bond length in the CH_3I molecule, but this bond is somewhat shorter than in the case of the hydrogen-bonded complex without water. This can be explained by the F-H interaction which weakens the C-H interaction and the fact that the weaker interaction means longer bond lengths. In the nine-atom system the F^--H_2O interaction weakens the other F^--H interaction this is why the CH bond length is the longest in the case of the F^--CH_3I system. In

agreement with this, the CH···F distance is longer in the monohydrated case than in the nonhydrated analogue. Zhang and co-workers found a similar structure at the MP2(ECP)/aug-cc-pVDZ(-PP) level (called im1 in Ref. 83) which has similar geometric parameters except the HFC angle which I found 75.1° in contrast with the 109.9° found by them.

It is interesting to compare the FCI angles in the case of HTS, PREMIN1, and WALDENTS1 and I found them 157.2°, 176.0°, and 178.7°, respectively. These values are close to the degrees of 158.2°, 175.5°, and 178.9° what Zhang and co-workers found with DFT.[83] In the WALDENTS1, this angle is very close to the 180° but due to the water molecule it does not reach it, while in the case of the nonhydrated analogue the FCI angle is 180° and the structure has C_{3v} symmetry, similarly to the ion-dipole complex in the entrance channel as can be seen in Figure 5.1.

Considering the carbon-halogen distances of the HTS, PREMIN1, and WALDENTS1 stationary points, the C-F bond lengths decrease as 2.760(2.744), 2.657(2.604), and 2.003(2.125) Å, while the C-I bond lengths increase as 2.171(2.211), 2.181(2.235), and 2.512(2.495) Å, respectively (the values in parentheses are the DFT results of Zhang and co-workers). In the case of the nonhydrated analogues the C-F distances are shorter and the C-I distances are longer for the HTS1 and the PREMIN1, while the reverse can be seen for the WALDENTS1.

Taking into account the most important geometric parameters of the POSTMIN structures, the OH-I distances are 2.729(2.774), 2.719(2.701) and 2.601(2.632) Å for POSTMIN1, POSTMIN2, and POSTMIN3, respectively. The C-I distances are 3.946(4.035), 3.760(4.058) and 3.727(3.906) Å for the POSTMIN1, POSTMIN2, and POSTMIN3, respectively, while this value is 3.618 Å for the unhydrated analogue, which shows the weakening effect of the I-H_2O interaction on the I-C interaction (DFT values of Zhang and co-workers are shown again in parentheses).

Figure 5.33 shows an other reaction route where the OH^- serves as a reactant after evolved from the H_2O molecule and the F^- ion by proton abstraction. The OH^- ion then inverts the CH_3I molecule by Walden inversion. The process starts with HMIN2 then the proton abstraction takes place before Walden transition state develops which has almost collinear O-C-I arrangement. After the substitution the POSTMIN4 stationary point takes place which can dissociate into three different product channels. The $CH_3OH + HF + I^-$, $CH_3OH(HF) + I^-$, and the $CH_3OH + I(HF)^-$ product channels have exothermicities of −19.9, −25.8, and −35.1 kcal/mol, respectively.

The geometry of POSTMIN4 stationary point is worth comparing with the $CH_3OH(HF)$ complex. The O-C bond is stronger in the POSTMIN4, because the I-H interaction weakens the O-H bond and due to the weaker O-H interaction the O-C interaction becomes stronger. As a result, the O-H bond is longer and the O-C bond is shorter in the case of the POSTMIN4. The interaction of the O atom with the HF unit is also stronger in the POSTMIN4 due to the same reason, and the H-F bond is consequently weaker in the POSTMIN4. POSTMIN4 is also comparable with the postreaction complex

of the $OH^- + CH_3I$ reaction,[93] even if that was found with larger basis set at the CCSD(T)-F12b(ECP)/aug-cc-pVTZ(-PP) level. This complex looks similar to the POSTMIN4 without the HF unit. The most significant difference occurs in the I-H bond length, because the O-HF interaction weakens the OH bond, and, in consequence, strengthens the I-H interaction. As a result, the I-H bond length is 2.448 Å in the nine-atom system and 2.584 Å in the seven-atom system. The I-H-O angle is 162.1° in the POSTMIN4 and 163.4° in the other case. The O-C distances are 1.415 and 1.410 Å in the nine-atom system and in the seven-atom system, respectively.

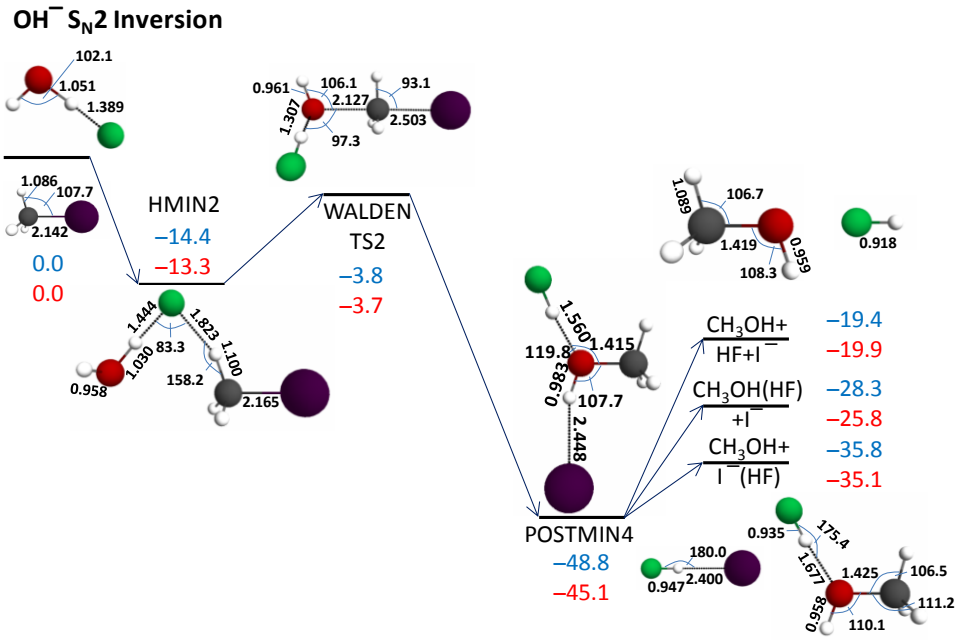

Figure 5.33.: Stationary-point structures along the OH^- S_N2 inversion pathway of the $F^-(H_2O)$ + CH_3I reaction (bond lengths in Å, angles in degrees obtained at CCSD(T)-F12b/aug-cc-pVDZ level). Energies relative to the reactants labelled with blue are the best classical energies calculated at CCSD(T)-F12b/aug-cc-pVQZ level at CCSD(T)-F12b/aug-cc-pVDZ geometries. Energies relative to the reactants labelled with red are the best adiabatic energies calculated at CCSD(T)-F12b/aug-cc-pVQZ level at CCSD(T)-F12b/aug-cc-pVDZ geometries with CCSD(T)-F12b/aug-cc-pVDZ ZPE-correction.

Figure 5.34 shows front-side attack pathways for the monohydrated F^- + CH_3I reaction which were unknown before this study. The reaction can start with FSMIN which is a minimum according to my calculations at CCSD(T)-F12b(ECP)/aug-cc-pVDZ(-PP) level or with FSPRETS which is a second-order saddle-point according to my calculations at the same level. Both starting stationary point can continue in either FSTS1 or FSTS2, which are second-order and third-order saddle-points, respectively. It is need to be mentioned that the frequency values below 100 or 100*i* cm^{-1} are uncertain. As a result, FSMIN is maybe a first-order saddle point, FSPRETS might be a first-order

saddle point, FSTS1 may be a first-order or third-order saddle point, FSTS2 is maybe a second-order saddle point as Table 5.4 shows.

The significantly higher energy of the FSPRETS relative to the FSMIN is in accord with the longer F-I distance (3.398 Å) of the FSPRETS than the FSMIN (2.426 Å). The barrier height of the reaction can be either 29.7 (30.7) kcal/mol (FSTS1) or 31.4 (32.1) kcal/mol (FSTS2). The energy values in parentheses are the best adiabatic energies and without parentheses are the best classical energies. The lower energy of the FSTS1 is probably due to the I-H interaction which misses from the FSTS2. The FSTS1 forms a ring-like structure with this plus interaction. The I-H interaction in the FSTS1 also causes longer F-H distance (1.690 Å) than the FSTS2 has (1.621 Å). In the case of both monohydrated FSTS the FCH_3I unit is semiquantitatively the same as in the nonhydrated case,[48] which can be seen in Figure 5.1.

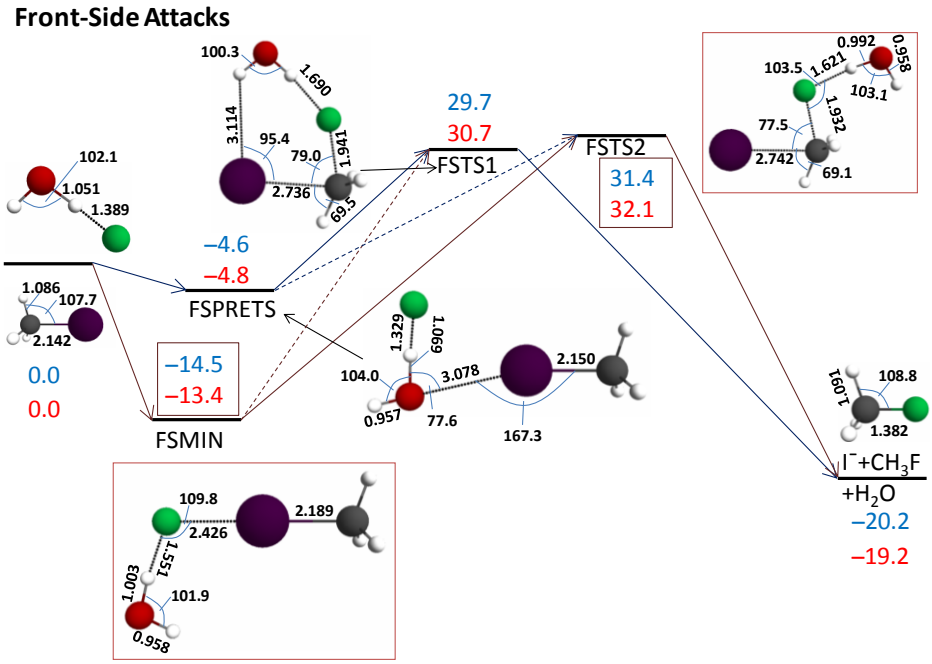

Figure 5.34.: Stationary-point structures along the front-side attack pathways of the $F^-(H_2O)$ + CH_3I reaction (bond lengths in Å, angles in degrees obtained at CCSD(T)-F12b/aug-cc-pVDZ level). Energies relative to the reactants labelled with blue are the best classical energies calculated at CCSD(T)-F12b/aug-cc-pVQZ level at CCSD(T)-F12b/aug-cc-pVDZ geometries. Energies relative to the reactants labelled with red are the best adiabatic energies calculated at CCSD(T)-F12b/aug-cc-pVQZ level at CCSD(T)-F12b/aug-cc-pVDZ geometries with CCSD(T)-F12b/aug-cc-pVDZ ZPE-correction.

As in the unhydrated case, a double-inversion reaction mechanism supposedly exists for this monohydrated system, too. In addition, the barrier of the double-inversion pathway is significantly lower (about 10 kcal/mol as Figures 5.34 and 5.35 show) than the barrier of the front-side reaction

route, again similarly to the nonhydrated case. The hydrated double-inversion pathway has already been investigated by Zhang and co-workers for the F^- + CH_3Cl system[85] and for the F^- + CH_3I system[94] with QM/MM simulations.

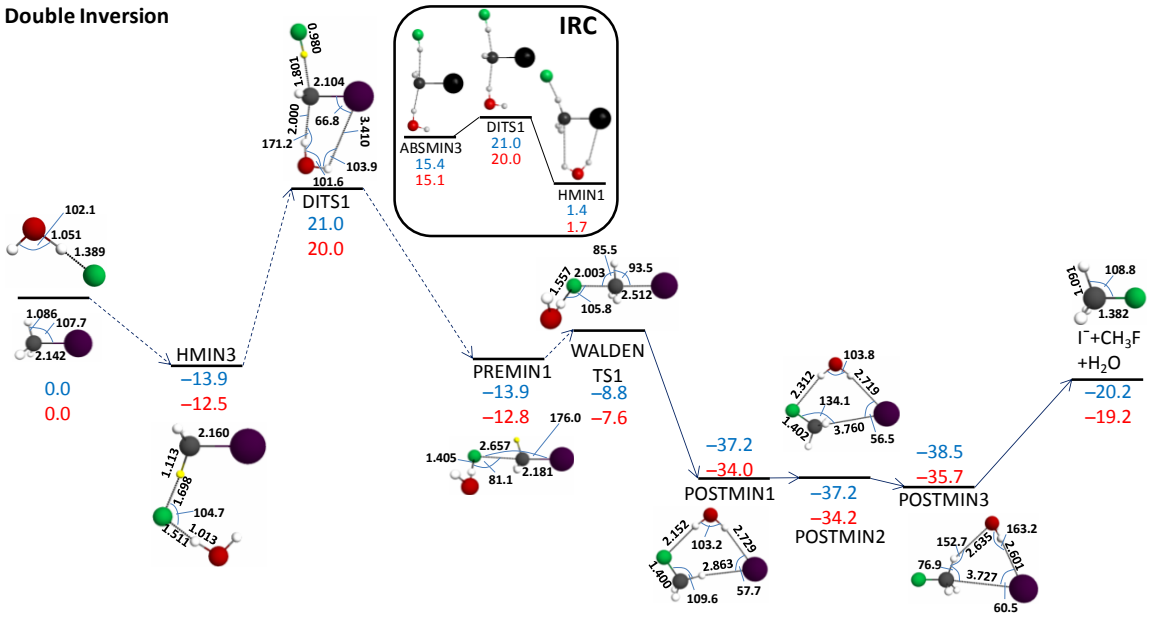

Figure 5.35.: Stationary-point structures along the double-inversion pathway of the $F^-(H_2O)$ + CH_3I reaction (bond lengths in Å, angles in degrees obtained at CCSD(T)-F12b/aug-cc-pVDZ level). Energies relative to the reactants labelled with blue are the best classical energies calculated at CCSD(T)-F12b/aug-cc-pVQZ level at CCSD(T)-F12b/aug-cc-pVDZ geometries. Energies relative to the reactants labelled with red are the best adiabatic energies calculated at CCSD(T)-F12b/aug-cc-pVQZ level at CCSD(T)-F12b/aug-cc-pVDZ geometries with CCSD(T)-F12b/aug-cc-pVDZ ZPE-correction. The yellow hydrogen helps to follow the first inversion.

According to Figure 5.35, the process starts with a hydrogen-bonding complex called HMIN3. Then the fluoride ion abstracts a proton from the methyl-iodide molecule and after the moving of the HF unit to the opposite side of the CH_2I^- unit, the double inversion-state develops. According to our IRC computations, the DITS1 connects the ABSMIN3 stationary point with the HMIN1. After the first inversion, the second inversion takes place starting with the ion-dipole complex PREMIN1 in the same way as in the case of the Walden-inversion process in Figure 5.32. The DITS1 is the most important stationary point in this process considering the geometric parameters. The geometry of the FH-CH_2I^- unit in the DITS1 is very similar to the nonhydrated analogue.[48] The C-HF distances are 1.801 and 1.835 Å in the nine-atom system and in the six-atom system, respectively. The fully hydrated FH-CH_2I^- unit is however very different according to the above mentioned QM/MM simulations by Zhang and co-workers, who found this structure close to the planar geometry in the case of the F^- + CH_3Cl system,[85] and also closer to the planar in the case of the F^- + CH_3I system.[94]

The later fact can be supported by the H-C-I angles which are 125.6° using the QM/MM method and 98.6° according to my computations[82] (the H atom is which bonds to the fluorine).

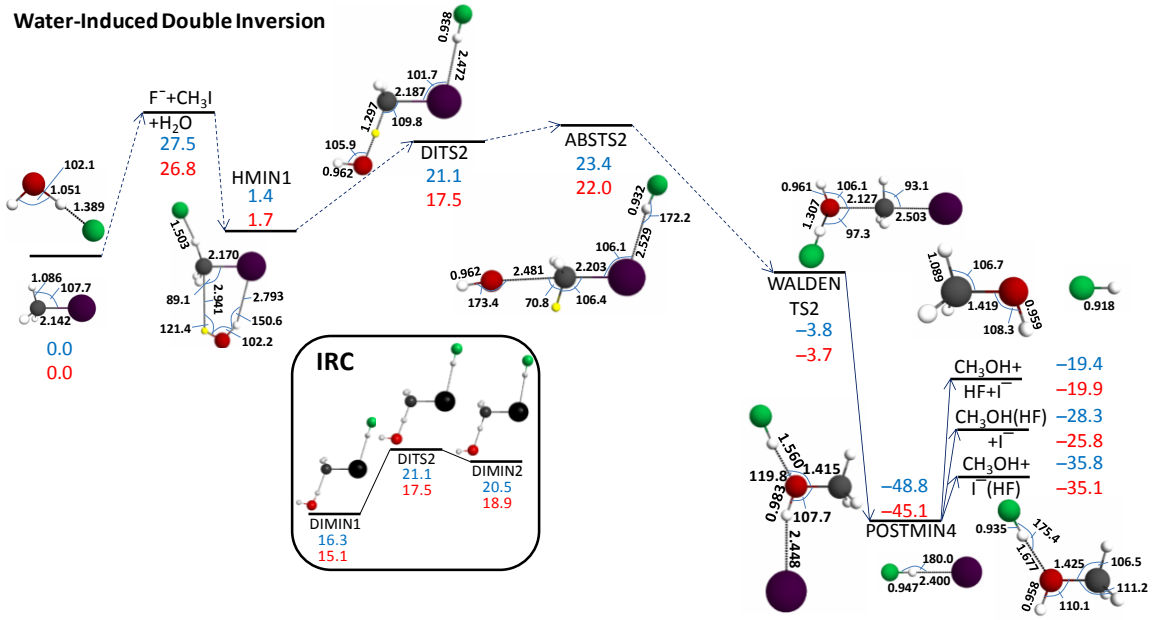

Figure 5.36.: Stationary-point structures along the water-induced double-inversion pathway of the $F^-(H_2O)$ + CH_3I reaction (bond lengths in Å, angles in degrees obtained at CCSD(T)-F12b/aug-cc-pVDZ level). Energies relative to the reactants labelled with blue are the best classical energies calculated at CCSD(T)-F12b/aug-cc-pVQZ level at CCSD(T)-F12b/aug-cc-pVDZ geometries. Energies relative to the reactants labelled with red are the best adiabatic energies calculated at CCSD(T)-F12b/aug-cc-pVQZ level at CCSD(T)-F12b/aug-cc-pVDZ geometries with CCSD(T)-F12b/aug-cc-pVDZ ZPE-correction. The yellow hydrogen helps to follow the first inversion. The first step is the dissociation of $F^-(H_2O)$ which may demand less energy than this diagram shows because the dissocation takes place in the vicinity of CH_3I.

Figure 5.36 shows the water-induced double-inversion mechanism proposed by us. The process start with the dissociation of the $F^-(H_2O)$ complex which is an exothermic process. The dissocation takes place in the neighbourhood of the CH_3I molecule. Thus, the dissociation energy is supposedly smaller than Figure 5.36 shows and the activation energy of the process is maybe the relative energy of the ABSTS2 with 23.4(22.0) kcal/mol (the best adiabatic energy shown again in parentheses). After that, hydrogen-bonding complex called HMIN1 develops. Then, the fluoride abstracts a proton from the methyl-iodide molecule. The HF unit moves to the iodine side of the CH_2I^- unit and connects to the iodine atom with a hydrogen bond. The water molecule gives a proton back to the CH_2I^- unit to the opposite side wherefrom the fluoride removed one, so causing the first inversion. This process is described by the DIMIN1, DITS2, and DIMIN2 stationary points in Figure 5.36. The DIMIN1 and DIMIN2 were found by IRC computations starting from DITS2. Then, the ABSTS2 saddle point takes place, where the OH^- unit connects to the CH_3I-HF unit with ion-dipole

interaction. The next stationary point is the WALDENTS2. It can be seen that the OH^- unit carries out the second inversion with the methyl-iodide unit. This is the Walden-inversion process as in the case of the OH^- S_N2 inversion. The HF unit connects to the O atom in the WALDENTS2 which means that stationary points may miss between the ABSTS2 and WALDENTS2. A question is arising here whether the second inversion goes through without the HF unit. It is possible, but I found that the dissociation of the HF unit from the ABSTS2 is an exothermic process by about 8.5 kcal/mol. The final stationary point before the product channels is the POSTMIN4 as in the case of the OH^- S_N2 inversion described in Figure 5.33. The product channels are also the same which were described for the OH^- S_N2 inversion process. Nevertheless, it is important to emphasize that here methanol is formed with retention of configuration. The most important structure to consider in this case is the DITS2. The C-H bond length for the abstraction H atom (labelled with yellow in Figure 5.36) is 1.297 Å which is longer by 0.211 Å than in the CH_3I molecule. The breaking O-H bond length is 1.322 Å, stretched by 0.363 Å relative to the bond length in the H_2O molecule.

Table 5.4.: CCSD(T)-F12b(ECP)/aug-cc-pVDZ(-PP) frequency values (cm^{-1}) of the stationary points along the pathways starting with front-side attack

FSMIN	FSPRETS	FSTS1	FSTS2
31	226*i*	657*i*	641*i*
69	86*i*	49*i*	119*i*
126	29	53	22*i*
127	66	73	52
141	68	147	93
218	98	235	122
312	430	281	279
508	551	386	400
514	583	406	495
831	874	774	818
833	874	827	848
945	1155	845	867
1238	1271	1134	1136
1474	1476	1423	1431
1475	1478	1477	1488
1730	1727	1714	1722
3039	1949	3117	3110
3061	3061	3238	3234
3132	3158	3273	3247
3133	3158	3449	3257
3889	3893	3859	3894

I have not constructed energy diagram for the abstraction reaction, because it would have been very difficult considering the fact that even in the case of the nonhydrated reaction different channels exist as Figure 5.1 shows. It is need to be mentioned that a recent DFT study showed a possible abstraction pathway for this channel.[95]

Summary

During my doctoral work my main goal was to study the dynamics and mechanisms of chemical reactions using first-principles theoretical techniques. Since a chemical system consists of electrons and nuclei one has to describe the motion of these particles. The electronic motion is treated quantum mechanically, whereas the much heavier nuclei can be well described using classical mechanics. The numerical solution of the electronic Schrödinger equation provides the potential energy surface, whose negative gradients give the forces, which govern the motion of the nuclei in a chemical reaction. The key of my research is the mathematical representation of the potential energy surface using a multidimensional analytical function obtained by fitting high-level *ab initio* energy points. Using this analytical surface the dynamics of chemical reactions can be efficiently studied with the quasiclassical trajectory method.

Motivated by the previous work of our research group on the dynamics of S_N2 reactions, my main project was the investigation of the $F^- + CH_3I$ S_N2 and proton-transfer reactions from several aspects. The $F^- + CH_3I$ system has become a benchmark prototype S_N2 reaction in the past 5 years, which has been under several experimental and theoretical investigations. However, analytical potential energy surface was not available for this important reaction, which hindered the efficient dynamical theoretical studies. Therefore, the first goal of my doctoral work was the development of an accurate potential energy surface for the $F^- + CH_3I$ reaction. In 2017 we reported such a surface, which describes the back-side attack Walden inversion, the front-side attack retention, and the double-inversion retention substitution pathways as well as the proton-abstraction (proton transfer from CH_3I to F^-) channel.

Using the newly developed analytical potential energy surface I performed quasiclassical trajectory computations with vibrationally unexcited reactants.[48] We found good agreement with experimental results, except for the highest collision energies where the quality of the PES may require further improvement. We achieved another purpose of our dynamical investigations namely that we found trajectories for this system belonging to the double-inversion mechanism, which is a recently discovered retention S_N2 reaction mechanism.[5]

The analytical potential developed during my PhD work made possible a long overdue investigation of the role of the front-side complex formation in the $F^- + CH_3I$ S_N2 reaction.[50] Since the iodine atom has the lowest electronegativity among the halogens, the role of this minimum is the most important in this case. Our simulations showed quantitatively for the first time that the halogen-bonded front-side complex plays a significant role in the dynamics of the $F^- + CH_3I$ reaction, whereas the formation of this complex is negligible for the $F^- + CH_3Cl$ reaction. This theoretical

finding provides the explanation of a previous experiment revealing that the $F^- + CH_3I$ reaction is much more indirect than the seemingly similar $F^- + CH_3Cl$ S_N2 reaction.

Beside the trajectories started with reactants which have only their zero-point energies, the effects of the vibrational excitations were also worth investigating. Such a mode-specific vibrational simulation requires extremely large number of trajectories. The analytical potential energy surface allows performing such an investigation. First, I ran trajectories at two collision energies investigating only the effect of the excitation of the CH symmetric stretch. These results were comparable with the experimental results of Roland Wester and co-workers and we found excellent agreement with the measuered results. The main consequence of our joint theoretical–experimental work[20] was that the CH stretching mode is spectator in the case of the S_N2 inversion but promotes the proton abstraction reaction pathway. Although this finding may seem expected, the previous theoretical studies provided contradictional results and our joint work reported the first evidence of the spectator character of the CH stretching mode in S_N2 reactions.

Since the above-mentioned theoretical–experimental study only involved two collision energies and the exciation of one vibrational mode, the investigation of other collision energies and other modes seemed to be necessary. I carried out these detailed mode-specific simulations for the $F^- + CH_3I$ S_N2 and proton-transfer reactions using our analytical potential energy surface.[69] The computed results showed that the CH stretching modes efficiently promote the S_N2 retention reaction pathway beside the abstraction channel. This can be explained by the fact that the double-inversion process starts with a proton abstraction. The results also showed that the excitation of the CI stretching mode is the most efficient way promoting the S_N2 inversion. Our detailed theoretical data may motivate future experimental investigations of the mode-specific dynamics of the $F^- + CH_3I$ reaction. In fact, experimental work studying the effect of the asymmetric CH stretching mode is underway in the Wester laboratory at the University of Innsbruck.

The role of the stationary points in the reaction dynamics has traditionally been observed mainly manually by watching trajectory animations. Thus, I carried out an investigation[80] in that I assigned the structures along the quasiclassical trajectories to stationary points based on the best overlap between the actual geometry and the stationary-point structure. I implemented this numerical technique into a fortran program. This new analysis tool provides stationary-point probability distributions, transition probability matrices, time-dependence of the assigned stationary points, etc. The stationary point probability results confirmed the important role of the front-side minimum in the case of the $F^- + CH_3I$ reaction and showed that the title reaction is a complex indirect process, where most of the stationary points are involved in every reaction pathways. In the future the application of this numerical assignment method would be interesting for a direct reaction as well.

Beside the investigation of the six-atomic F^- + CH_3I reaction the monohydrated case, where a H_2O molecule is attached to the system, seemed also important because of the widespread practical applications of the solution-phase reactions. For the nine-atomic $F^-(H_2O)$ + CH_3I system previous experiments and direct dynamics simulations were reported but a detailed high-level *ab initio* characterization of the stationary points was lacking. Therefore, I carried out such an *ab initio* study using the explicitly correlated CCSD(T)-F12b method for the first time in the case of a monohydrated S_N2 reaction. I found 29 stationary points based on our own chemical intuition, prior work, and intrinsic reaction coordinate computations.[82] Using these stationary points several new reaction pathways are proposed besides the previously known Walden-inversion mechanism. It is important that in this case the water molecule can play a role as a reactant, too. One way of this is an inversion pathway producing methanol, which was known in the literature. However, our newly proposed reaction route, called water-induced double inversion, is a kind of double-inversion mechanism which results in methanol which has the same configuration as the reactant methyl-iodide molecule. This system needs further investigation including the finding of more stationary points, reaction dynamics simulations, and experiments. Development of an analytical potential energy surface for a monohydrated S_N2 reaction is challenging but possible with the techniques used during my doctoral work.

My theoretical research demonstrates that the analytical *ab initio* potential energy surface-based approach is a powerfull tool to reveal the dynamics of chemical reactions with unprecedented details. The analytical potential allows using high-level of electronic structure theory and running millions of trajectories, thereby providing better accuracy, both electronic structure and statistical points of view, than the traditional direct dynamics simulations. The large number of trajectories makes the identification of low-probability reaction pathways, such as front-side attack and double inversion possible. The statistically accurate differential cross sections and internal energy distributions allow direct comparision with crossed-beam experiments. As a result my PhD research revealed several new findings about a prototypical S_N2 reaction such as the possibility of front-side attack and double-inversion retention mechanisms, significant front-side complex formation, spectator character of the CH symmetric stretching mode, mode-specific dynamics, and a novel water-induced double-inversion mechanism in the case of the monohydrated system. Furthermore, the numerical stationary-point assignment technique developed during my doctoral work certainly will become a useful tool to uncover novel reaction mechanisms for complex polyatomic chemical reactions.

Acknowledgements

I express thanks to the Richter Scholarship, the National Research, Development and Innovation Office–NKFIH, K-125317, and the Ministry of Human Capacities, Hungary grant 20391-3/2018/FEKUSTRAT for the financial support.

I thank principally to my supervisor Dr. Gábor Czakó for his supporting. I give thanks to other co-workers, Dr. István Szabó, Dr. Gábor Paragi, Prof. Roland Wester and his research team, and Tibor Győri.

I acknowledge the KIFÜ Institute (former name NIIFI) for awarding me access to computational resources at Szeged and Debrecen.

References

[1] Xie, J.; Hase, W.L. Rethinking the S_N2 reaction, Science, 2016, 352, 32-33

[2] Walden, P. Über die gegenseitige Umwandlung optischer Antipoden. Berichte der deutschen chemischen Gesellschaft, 1896, 29, 133-138

[3] Laerdahl, J.K.; Uggerud, E. Gas phase nucleophilic substitution, Int. J. Mass Spectr., 2002, 214, 277-314

[4] Cayzergues, P.; Georgoulis, C.; Ville, G.J. Evidence for a bimolecular aliphatic substitution with partial retention of configuration, at a saturated carbon-atom, Chem. Res. (S), 1978, 325

[5] Szabó, I.; Czakó, G. Revealing a double-inversion mechanism for the $F^- + CH_3Cl$ S_N2 reaction, Nat. Commun., 2015, 6, 5972

[6] Mikosch, J.; Trippel, S.; Otto, R.; Eichhorn, C.; Hlavenka, P.; Weidemüller, M.; Wester, R. Kinematically complete reaction dynamics of slow ions, J. Phys.: Conf. Ser., 2007, 88, 012025

[7] Mikosch, J.; Trippel, S.; Eichhorn, C.; Otto, R.; Lourderaj, U.; Zhang, J.X.; Hase, W.L.; Weidemüller, M.; Wester, R. Imaging nucleophilic substitution dynamics, Science, 2008, 319, 183-186

[8] Wang, H.; Hase, W.L. Kinetics of $F^- + CH_3Cl$ S_N2 nucleophilic substitution, J. Am. Chem. Soc., 1997, 119, 3093-3102

[9] Su, T.; Wang, H.; Hase, W.L. Trajectory studies of S_N2 nucleophilic substitution. 7. $F^- + CH_3Cl \rightarrow FCH_3 + Cl^-$, J. Phys. Chem. A, 1998, 102, 9819-9828

[10] Espinosa-Garcia, J.; Bravo, J.L.; Rangel, C. New analytical potential energy surface for the $F(^2P) + CH_4$ hydrogen abstraction reaction: kinetics and dynamics, J. Phys. Chem. A, 2007, 111, 2761-2771

[11] Czakó, G.; Shepler, B.C.; Braams, B.J.; Bowman, J.M. Accurate *ab initio* potential energy surface, dynamics, and thermochemistry of the $F + CH_4 \rightarrow HF + CH_3$ reaction, J. Chem. Phys., 2009, 130, 084301

[12] Czakó, G.; Bowman, J.M. Dynamics of the reaction of methane with chlorine atom on an accurate potential energy surface, Science, 2011, 334, 343-346

[13] Li, J.; Jiang, B.; Guo, H. Permutation invariant polynomial neural network approach to fitting potential energy surfaces. II. Four-atom systems, J. Chem. Phys., 2013, 139, 204103

[14] Chen, J.; Xu, X.; Xu, X.; Zhang, D.H. A global potential energy surface for the $H_2 + OH \leftrightarrow H_2O + H$ reaction using neural networks, J. Chem. Phys., 2013, 138, 154301

[15] Szabó, I.; Császár, A.G.; Czakó, G. Dynamics of the $F^- + CH_3Cl \rightarrow Cl^- + CH_3F$ S_N2 reaction on a chemically accurate potential energy surface, Chem. Sci., 2013, 4, 4362-4370

[16] Sun, R.; Xie, J.; Zhang, J.; Hase, W.L. The $F^- + CH_3I \rightarrow FCH_3 + I^-$ entrance channel potential energy surface Comparison of electronic structure methods, Int. Journal Mass Spectr. 2015, 377, 222-227

[17] Zhang, J.; Hase, W.L. Electronic structure theory study of the $F^- + CH_3I \rightarrow FCH_3 + I^-$ potential energy surface, J. Phys. Chem. A, 2010, 114, 9635-9643

[18] Ma, Y-T., Ma, X.; Li, A.; Guo, H.; Yang, L.; Zhang, J.; Hase, W.L. Potential energy surface stationary points and dynamics of the $F^- + CH_3I$ double inversion mechanism, Phys. Chem. Chem. Phys., 2017, 19, 20127-20136

[19] Carrascosa, E.; Michaelsen, T.; Stei, M.; Bastian, B.; Meyer, J.; Mikosch, J.; Wester, R. Imaging proton transfer and dihalide formation pathways in reactions of $F^- + CH_3I$, J. Phys. Chem. A, 2016, 120, 4711-4719

[20] Stei, M.; Carrascosa, E.; Dörfler, A.; Meyer, J.; Olasz, B.; Czakó, G.; Li, A.; Guo, H.; Wester, R. Stretching vibration is a spectator in nucleophilic substitution, Sci. Adv., 2018, 4, eaas9544

[21] Born, M.; Oppenheimer, R. Zur Quantentheorie der Molekeln. Ann. Phys., 1927, 389, 457-484

[22] Hehre, W. J.; Radom, L.; Schleyer, P. v. R.; Pople, J. A. Molecular orbital theory; Wiley: New York, 1986, 7, 379

[23] Møller, C.; Plesset, M. S. Note on an approximation treatment for many-electron systems, Phys. Rev., 1934, 46, 618-622

[24] Čížek, J. On the correlation problem in atomic and molecular systems. Calculation of wavefunction components in Ursell-type expansion using quantum-field theoretical methods, J. Chem. Phys., 1966, 45, 4256-4266

[25] Adler, T.B.; Knizia, G.; Werner, H.-J. A simple and efficient CCSD(T)-F12 approximation, J. Chem. Phys., 2007, 127, 221106

[26] Kohn, W.; Sham, L. J. Self-consistent equations including exchange and correlation effects, Phys. Rev., 1965, 140, A1133-A1138

[27] Becke, A.D. A new mixing of Hartree-Fock and local density-functional theories, J. Chem. Phys., 1993, 98, 1372-1377

[28] Zhao, Y.; Truhlar, D. G. A new local density functional for main-group thermochemistry, transition metal bonding, thermochemical kinetics, and noncovalent interactions, J. Chem. Phys., 2006, 125, 194101

[29] Binkley, J.S.; Pople, J.A.; Hehre, W.J. Self-consistent molecular orbital methods. 21. Small split-valence basis sets for first-row elements, J. Am. Chem. Soc., 1980, 102, 939-947

[30] Dunning Jr., D.H. Gaussian basis sets for use in correlated molecular calculations. I. The atoms boron through neon and hydrogen, J. Chem. Phys., 1989, 90, 1007-1023

[31] Ypma, T.J. Historical development of the Newton–Raphson method, SIAM Rev., 1995, 37, 531-551

[32] Case, A. Normal mode analysis of protein dynamics, Curr. Op. Struct. Biol., 1994, 4, 285-290

[33] Sun, L.; Song, K.; Hase, W.L. A S_N2 reaction that avoids its deep potential energy minimum, 2002, 296, 875-878

[34] Braams, J.B.; Bowman, J.M. Permutationally invariant potential energy surfaces in high dimensionality, Int. Rev. Phys. Chem., 2009, 28, 577-606

[35] Szabó, I.; Czakó, G. Dynamics and novel mechanisms of S_N2 reactions on *ab initio* analytical potential energy surfaces, J. Phys. Chem. A, 2017, 121, 9005-9019

[36] Conte, R.; Qu, C.; Bowman, J.M. Permutationally invariant fitting of many-body, non-covalent interactions with application to three-body methane–water–water, J. Chem. Theory. Comput., 2015, 11, 1631-1638

[37] Bowman, J.M.; Czakó, G.; Fu, B. High-dimensional *ab initio* potential energy surfaces for reaction dynamics calculations, Phys. Chem. Chem. Phys., 2011, 13, 8094-8111

[38] Conte, R.; Houston, P.L.; Bowman, J.M. A benchmark-quality, full-dimensional *ab initio* potential energy surface for Ar-HOCO, J. Chem. Phys, 2014, 140, 151101

[39] Wang, Y.; Bowman, J.M. Calculations of the IR spectra of bend fundamentals of $(H_2O)_{n=3;4;5}$ using the WHBB 2 potential and dipole moment surfaces, Phys. Chem. Chem. Phys., 2016, 18, 24057-24062

[40] Levesque, D.; Verlet, L. Molecular dynamics and time reversibility, J. Stat. Phys., 1993, 72, 519–537

[41] Hase, W.L. Encyclopedia of Computational Chemistry, 1998, Wiley, New York, 399-407

[42] Bonnet, L.; Rayez, J.C. Quasiclassical trajectory method for molecular scattering processes: Necessity of a weighted binning approach, Chem. Phys. Lett., 1997, 277, 183-190

[43] Czakó, G.; Bowman, J.M. Quasiclassical trajectory calculations of correlated product distributions for the F + CHD_3(v_1 = 0, 1) reactions using an *ab initio* potential energy surface, J. Chem. Phys., 2009, 131, 244302

[44] Czakó, G.; Gaussian binning of the vibrational distributions for the Cl + CH_4($v_{4/2}$=0,1) $\rightarrow$ H + CH_3Cl($n_1n_2n_3n_4n_5n_6$) reactions, J. Phys. Chem. A, 2012, 116, 7467-7473

[45] Knowles, P.J.; Werner, H.-J. An efficient method for the evaluation of coupling coefficients in configuration interaction calculations, Chem. Phys. Lett., 1988, 145, 514-522

[46] Robinson, J.B.; Knowles, P.J. Breaking multiple covalent bonds with Hartree–Fock-based quantum chemistry: quasi-variational coupled cluster theory with perturbative treatment of triple excitations, Phys. Chem. Chem. Phys., 2012, 14, 6729-6732

[47] Győri, T.; Olasz, B.; Paragi, G.; Czakó, G. Effects of the level of electronic structure theory on the dynamics of the F^- + CH_3I reaction, J. Phys. Chem. A., 2018, 122, 3353-3364

[48] Olasz, B.; Szabó, I.; Czakó, G. High-level *ab initio* potential energy surface and dynamics of the F^- + CH_3I S_N2 and proton-transfer reactions, Chem. Sci., 2017, 8, 3164-3170

[49] Werner, H.-J.; Knowles, P.J.; Knizia, G.; Manby, F.R.; Schütz, M.; and others, Molpro, version 2015.1; a package of *ab initio* programs, see http://www.molpro.net.

[50] Szabó, I.; Olasz, B.; Czakó, G. Deciphering front-side complex formation in S_N2 Reactions via dynamics mapping, J. Phys. Chem. Lett., 2017, 8, 2917-2923

[51] Polanyi, J.C. Some concepts in reaction dynamics, Acc. Chem. Res., 1972, 236, 680-690

[52] Zare, R.N. Laser control of chemical reactions, Science, 1998, 279, 1875-1879

[53] Crim, F.F. Chemical dynamics of vibrationally excited molecules: Controlling controlling reactions in gases and on surfaces, Proc. Natl. Acad. Sci. U.S.A. 2008, 105, 12654-12661

[54] Zhang, W.; Kawamata, H.; Liu, K. CH stretching excitation in the early barrier $F + CHD_3$ reaction inhibits CH bond cleavage, Science, 2009, 325, 303-306

[55] Wang, F.; Kiu, L. Enlarging the reactive cone of acceptance by exciting the C-H bond in $O(^3P) + CHD_3$ reaction, Chem. Sci., 2010, 1, 126-133

[56] Wang, Y.; Song, H.; Szabó, I.; Czakó, G.; Guo, H.; Yang, M. Mode-specific S_N2 reaction dynamics, J. Phys. Chem. Lett., 2016, 7, 3322-3327

[57] Kowalewski, M.; Mikosch, J.; Wester, R.; Vivie-Riedle, de R. Nucleophilic substitution dynamics: Comparing quantum wave packet calculations with experiment, J. Phys. Chem. A., 2014, 118, 4661-4669

[58] Zhang, J.; Xie, J.; Hase, W.L. Dynamics of the $F^- + CH_3I \rightarrow HF + CH_2I^-$ proton transfer reaction, J. Phys. Chem. A, 2015, 119, 12517-12525

[59] Viggiano, A.A.; Morris, R.A.; Paschkewitz, J.S.; Paulson, J.F. Kinetics of the gas-phase reactions of Cl^- with CH_3Br and CD_3Br: experimental evidence for nonstatistical behavior?, J. Am. Chem. Soc., 1992, 114, 10477-10482

[60] Ayotte, P.; Kim, J.; Kelley, J. A.; Nielsen, S. B.; Johnson, M. A. Photoactivation of the $Cl^- + CH_3Br$ S_N2 reaction via rotationally resolved C-H stretch excitation of the $Cl^- \cdot CH_3Br$ entrance channel complex, J. Am. Chem. Soc. 1999, 121, 6950-6951

[61] Tonner, D. S.; McMahon, T. B. Non-statistical effects in the gas phase S_N2 Reaction, J. Am. Chem. Soc. 2000, 122, 8783-8784

[62] Hennig, C.; Schmatz, S. Spectator modes in reaction dynamics revisited: Reaction cross sections and rate constant for $Cl^- + CH_3Br \rightarrow ClCH_3 + Br^-$ from quantum scattering, Chem. Phys. Lett., 2007, 446, 250-255

[63] Hennig, C.; Schmatz, S. State-selected dynamics of the complex-forming bimolecular reaction $Cl^- + CH_3Cl' \rightarrow ClCH_3 + Cl'^-$: A four-dimensional quantum scattering study, J. Chem. Phys. 2004, 121, 220-236

[64] Schmatz, S. Quantum dynamics of gas-phase S_N2 reactions, ChemPhysChem 2004, 5, 600-617

[65] Hennig, C.; Schmatz, S. Four-dimensional quantum study on exothermic complex-forming reactions: $Cl^- + CH_3Br \rightarrow ClCH_3 + Br^-$, J. Chem. Phys. 2005, 122, 234307

[66] Kowalewski, M.; Mikosch, J.; Wester, R.; de Vivie-Riedle, R. Nucleophilic substitution dynamics: comparing wave packet calculations with experiment, J. Phys. Chem. A 2014, 118, 4661-4669

[67] Wang, Y.; Song, H.; Szabó, I.; Czakó, G.; Guo, H.; Yang, M. Mode-specific S_N2 reaction dynamics, J. Phys. Chem. Lett., 2016, *7*, 3322-3327

[68] Szabó, I.; Czakó, G. Mode-specific multi-channel dynamics of the $F^- + CHD_2Cl$ reaction on a global *ab initio* potential energy surface, J. Chem. Phys., 2016, 145, 134303

[69] Olasz, B.; Czakó, G. Mode-specific quasiclassical dynamics of the $F^- + CH_3I$ S_N2 and proton-transfer reactions, J. Phys. Chem. A, 2018, 122, 8143-8151

[70] Szabó, I.; Czakó, G. Double-inversion mechanisms of the $X^- + CH_3Y$ [X,Y = F, Cl, Br, I] S_N2 reactions, J. Phys. Chem. A, 2015, 119, 3134-3140

[71] Ma, Y.-T.; Ma, X.; Li, A.; Guo, H.; Yang, L.; Zhang, J.; Hase, W. L. Potential energy surface stationary points and dynamics of the $F^- + CH_3I$ double inversion mechanism, Phys. Chem. Chem. Phys., 2017, 19, 20127-20136

[72] Mikosch, J.; Zhang, J.; Trippel, S.; Eichhorn, C.; Otto, R.; Sun, R.; de Jong, W.A.; Weidemüller, M.; Hase, W.L.; Wester, R. Indirect dynamics in a highly exoergic substitution reaction, J. Am. Chem. Soc., 2013, 135, 4250-4259

[73] Szabó, I.; Telekes, H.; Czakó, G. Accurate *ab initio* potential energy surface, thermochemistry, and dynamics of the $F^- + CH_3F$ S_N2 and proton-abstraction reactions, J. Chem. Phys., 2015, 142, 244301

[74] Corchado, J.C.; Espinosa-Garcia, J. Product vibrational distributions in polyatomic species based on quasiclassical trajectory calculations, Phys. Chem. Chem. Phys., 2009, 11, 10157-10164

[75] Ping, L.; Tian, L.; H. Song, H.; Yang, M. New method to extract final-state information of polyatomic reactions based on normal mode analysis, J. Phys. Chem. A, 2018, 122, 6997-7005

[76] Czakó, G.; Kaledin, A.L.; Bowman, J.M. Zero-point energy constrained quasiclassical, classical, and exact quantum simulations of isomerizations and radial distribution functions of the water trimer using an *ab initio* potential energy surface, Chem. Phys. Lett., 2010, 500, 217-222

[77] Czakó, G.; Kaledin, A.L.; Bowman, J.M. A practical method to avoid zero-point leak in molecular dynamics calculations: Application to the water dimer, J. Chem. Phys., 2010, 132, 164103

[78] Czakó, G.; Bowman, J.M. Reaction dynamics of methane with F, O, Cl, and Br on *ab initio* potential energy surfaces, J. Phys. Chem. A, 2014, 118, 2839-2864

[79] Tsutsumi, T.; Harabuchi, Y.; Ono, Y.; Maeda, S.; Taketsugu, T. Analyses of trajectory on-the-fly based on the global reaction route map, Phys. Chem. Chem. Phys., 2018, 20, 1364-1372

[80] Olasz, B.; Czakó, G.; Uncovering the role of the stationary points in the dynamics of the F^- + CH_3I reaction, Phys. Chem. Chem. Phys., 2019, 21, 1578-1586

[81] Viggiano, A. A.; Morris, R. A.; Paschkewitz, J. S.; Paulson, J. F. Kinetics of the gas-phase reactions of Cl^- with CH_3Br and CD_3Br: experimental evidence for nonstatistical behavior?, J. Am. Chem. Soc., 1992, 114, 10477-10482

[82] Olasz, B.; Czakó, G.; High-level-optimized stationary points for the $F^-(H_2O)$ + CH_3I system: Proposing a new water-induced double-inversion pathway, J. Phys. Chem. A, 2019, 123, 454-462

[83] Zhang, J.; Yang, L.; Sheng, L. Electronic structure theory study of the microsolvated $F^-(H_2O)$ + CH_3I S_N2 reaction, J. Phys. Chem. A, 2016, 120, 3613-3622

[84] Davico, G.E. Interpretation of the gas-phase solvent deuterium kinetic isotope effects in the S_N2 reaction mechanism: comparison of theoretical and experimental results in the reaction of microsolvated fluoride ions with methyl halides, J. Phys. Chem. A, 2006, 110, 13112-13121

[85] Liu, P.; Wang, D.; Xu, Y. A new, double-inversion mechanism of the F^- + CH_3Cl S_N2 reaction in aqueous solution, Phys. Chem. Chem. Phys., 2016, 18, 31895-31903

[86] Yang, L.; Liu, X.; Zhang, J.; Xie, J. Effect of microsolvation on a S_N2 reaction. Indirect atomistic dynamics and weakened suppression of reactivity, Phys. Chem. Chem. Phys., 2017, 19, 9992-9999

[87] Zhang, J.; Yang, L.; Xie, J.; Hase, W.L. Microsolvated $F^-(H_2O)$ + CH_3I S_N2 reaction dynamics. Insight into the suppressed formation of solvated products, J. Phys. Chem. Lett., 2016, 7, 660-665

[88] Liu, X.; Yang, L.; Zhang, J. Competition of F/OH-induced S_N2 and proton-transfer reactions with increased solvation, J. Phys. Chem. A, 2018, 122, 9446-9453

[89] Liu, X; Xie, J.; Zhang, J.; Yang, L.; Hase, W.L. Steric effects of solvent molecules on S_N2 substitution dynamics, J. Phys. Chem. Lett., 2017, 8, 1885-1892

[90] Otto, R.; Brox, J.; Trippel, S.; Stei, M.; Best, T.; Wester, R. Exit channel dynamics in a micro-hydrated S_N2 reaction of the hydroxyl anion, J. Phys. Chem. A, 2013, 117, 8139-8144

[91] Otto, R.; Brox, J.; Trippel, S.; Stei, M.; Best, T.; Wester, R. Single solvent molecules can affect the dynamics of substitution reactions, Nat. Chem., 2012, 4, 534-538

[92] O'Hair, R. A. J.; Davico, G. E.; Hacaloglu, J.; Dang, T. T.; DePuy, C. H.; Bierbaum, V. M. Effects for the gas-phase S_N2 reactions of fluoride with methyl halides, J. Am. Chem. Soc., 1994, 116, 3609-3610

[93] Tasi, D.A.; Fábián, Z.; Czakó, G. Benchmark *ab initio* characterization of the inversion and retention pathways of the OH^- + CH_3Y [Y = F, Cl, Br, I] S_N2 reactions, J. Phys. Chem. A, 2018, 122, 5773-5780

[94] Liu, P.; Zhang, J.; Wang, D. Y. Multi-level quantum mechanics theories and molecular mechanics study of the double-inversion mechanism of the F^- + CH_3I reaction in aqueous solution, Phys. Chem. Chem. Phys., 2017, 19, 14358-14365

[95] Liu, X.; Yang, L.; Zhang, J.; Sun, J. Competition of F/OH induced S_N2 and proton-transfer reactions with increased solvation, J. Phys. Chem. A, 2018, 122, 9446-9453